

**THE EFFECTS OF MANGANESE  
CONCENTRATION ON THE MECHANICAL  
PROPERTIES OF A356 ALUMINUM ALLOY  
WHEELS PRODUCED BY LOW PRESSURE DIE  
CASTING**

**A Thesis Submitted to  
the Graduate School of Engineering and Sciences of  
İzmir Institute of Technology  
in Partial Fulfillment of the Requirements for the Degree of  
MASTER OF SCIENCE  
in Materials Science and Engineering**

**by  
Ahmet Yiğit KAYA**

**June 2024  
İZMİR**

We approve the thesis of **Ahmet Yiğit KAYA**

**Examining Committee Members:**

**Assoc. Prof. Mertol GÖKELMA**

Department of Materials Science and Engineering, Izmir Institute of Technology

**Assoc. Prof. Özge BALCI ÇAĞIRAN**

Department of Materials Science and Engineering, Izmir Institute of Technology

**Assoc. Prof. Esra DOKUMACI ALKAN**

Department of Metallurgical and Materials Engineering, Dokuz Eylül University

**10 June 2024**

**Assoc. Prof. Mertol GÖKELMA**

Supervisor, Department of  
Materials Science and Engineering,  
Izmir Institute of Technology

**Asst. Prof. Dr. Kemal DAVUT**

Co-Supervisor, Department of  
Materials Science and Engineering,  
Izmir Institute of Technology

**Prof. Dr. Yaşar AKDOĞAN**

Head of the Department of  
Materials Science and Engineering,  
Izmir Institute of Technology

**Prof. Dr. Mehtap EANES**

Dean of the Graduate School of  
Engineering and Sciences

## ACKNOWLEDGEMENTS

I would like to express my sincere gratitude to my advisors, Asst. Prof. Dr. Mertol GÖKELMA and Asst. Prof. Dr. Kemal DAVUT for their invaluable guidance, support, motivation, and encouragement during my thesis. I extend my deepest thanks to my committee members Assoc. Prof. Özge BALCI ÇAĞIRAN and Assoc. Prof. ESRA DOKUMACI ALKAN for their interest and constructive review of the final manuscript.

My heartfelt appreciation also goes to Onur ÖZAYDIN, who has been a guiding force since the very beginning of my career. He has always provided technical expertise and served as an inspirational role model, influencing my path by consistently behaving as a supportive mentor rather than just a team leader.

I would like to extend my heartfelt gratitude to my former colleagues Tunahan ÖZAY, Süleyman BAKIR, Gizem AMMAS, and my former manager Şansal TEKELİ for their moral courage, technical and mental support during both good times and, especially, during challenging times.

I am profoundly grateful to my dear friends Ceren TÜRKDOĞAN DAMAR, Senagül TUNCA TAŞKIRAN, Nazife ÇERCİ, and Ayberk GÜRBÜZ. Their unwavering support in helping me conduct my Charpy impact tests, along with their constant assistance and encouragement, made my transition to the academy smoother and more gratifying. Their friendship and kindness have been invaluable throughout this journey.

I would also like to thank the IZTECH Center for Materials Research and Cevher Alloy Wheels Co. for their provision of the labor and materials essential for the manufacturing and analysis undertaken in this thesis.

I would like to express my greatest thanks to my childhood friend Emir Ulaş UÇAKURT, along with Elif ULU UÇAKURT, Sıla ÖZ GÖRKEM, and Enes GÖRKEM who have grown together with me, evolving from old friends into a bond like a family. I am deeply thankful for the enduring memories we've shared together.

Finally, I would like to express my deepest gratitude to my dear grandparents, Sedat Huzeyfe ŞENSES, Ayser ŞENSES, my dear uncle Sinan ŞENSES, as well as my dear mother, İlknur KAYA, my dear father Ramazan KAYA, my dear brother Arda KAYA. Their lifelong inspiration, support, and encouragement have been the guiding lights of my life. I am profoundly thankful to have them by my side

## ABSTRACT

### THE EFFECTS OF MN CONCENTRATION ON THE MECHANICAL PROPERTIES OF A356 ALUMINUM ALLOY WHEELS PRODUCED BY LOW PRESSURE DIE CASTING

Aluminum has become increasingly crucial in the automotive industry and automobile wheels, often made from aluminum alloy, because of their recycling efficiency, high specific strength, thermal conductivity, machinability, and corrosion resistance, contribute to vehicles' enhanced performance and improved fuel efficiency due to their reduced weight. Aluminum alloy wheels must meet specific mechanical standards. A major concern is whether recycled aluminum alloys can fulfill these mechanical requirements. As the proportion of recycled scrap increases in aluminum alloy components, the mixing and accumulation of impurities become significant issues.

In this study, Mn was used to counteract the detrimental effects of iron content. The presence of Mn neutralizes these adverse effects, thereby enabling the use of secondary aluminum in safety-critical applications. For this purpose, A356 alloy automobile wheels containing 0.040 wt% (batch 1), 0.069 wt% (batch 2) and 0.14 wt% (batch 3) Mn were cast by low pressure die casting method. In order to see the effects of Mn by examining intermetallics, optical microscope examination was performed and these images were converted into numerical data with the help of ImageJ software. In addition. The mechanical properties of the produced wheels were examined by performing hardness measurement, tensile test, and Charpy impact test. Fracture surfaces formed as a result of Charpy impact test were examined with the help of SEM and EDX.

As expected, the hardness and yield strength values exhibited similar behavior across all samples. With regional increases and decreases mirroring each other. After statistical analysis a non-strong negative linear correlation between Mn concentration and mechanical properties was observed. Therefore, Mn addition is not the only and the strongest parameter for the decrease in mechanical properties. Impact energy is strongly influenced on aspect ratio and grains/mm<sup>2</sup> as like elongation and yield strength. But oppositely, it is more sensitive aspect ratio than grains/mm<sup>2</sup>.



# ÖZET

## MANGAN KONSANTRASYONUNUN ALÇAK BASINÇLI DÖKÜM YÖNTEMİYLE ÜRETİLMİŞ A356 ALUMİNYUM ALAŞIMLI JANTLARDA MEKANİK ÖZELLİKLERE ETKİSİ

Alüminyum, otomotiv endüstrisinde her geçen gün daha önemli hale gelmektedir. Genellikle alüminyum alaşımından yapılan otomobil jantları, geri dönüşüm verimliliği, yüksek özgül mukavemeti, termal iletkenliği, işlenebilirliği ve korozyon direnci nedeniyle tercih edilmekte ve hafiflikleriyle araçların artan performansına ve yakıt verimliliğine katkıda bulunmaktadır. Alüminyum alaşımli jantlar belirli mekanik standartları karşılamak zorundadır. Bu konudaki büyük bir endişe, geri dönüştürülmüş alüminyum alaşımlarının bu mekanik gereksinimleri karşılayıp karşılayamayacağıdır. Alüminyum alaşımlarında geri dönüştürülmüş hurda oranı arttıkça, empüritelerin karışması ve birikmesi önemli sorunları beraberinde getirmektedir.

Bu çalışmada demir içeriğinin zararlı etkilerini ortadan kaldırmak için Mn kullanılmıştır. Mangan varlığı demir intermetaliklerinin olumsuz etkilerini nötralize eder, böylece ikincil alüminyumun güvenlik açısından kritik uygulamalarda kullanılmasına olanak tanır. Bu amaçla ağırlıkça %0,040 (şarj 1), ağırlıkça %0,069 (şarj 2) ve ağırlıkça %0,14 (şarj 3) Mn içeren A356 alaşımli otomobil jantları alçak basınçlı döküm yöntemiyle döküldü. İntermetalikler incelenerek Mangan etkilerinin görülebilmesi amacıyla optik mikroskop incelemesi yapılmış ve bu görüntüler ImageJ yazılımı yardımıyla sayısal verilere dönüştürülmüştür. Üretilen jantların mekanik özellikleri sertlik ölçümü, çekme testi ve Charpy darbe testi yapılarak incelenmiştir. Charpy darbe testi sonucunda oluşan kırılma yüzeyleri SEM ve EDX yardımıyla incelenmiştir.

Beklendiği gibi, sertlik ve akma dayanımı değerleri tüm numunelerde benzer davranış sergilemiştir. Bölgesel artış ve azalışlar vardır. İstatistiksel analizler sonrasında, Mn konsantrasyonu ile mekanik özellikler arasında güçlü olmayan negatif doğrusal bir korelasyon gözlenmiştir. Dolayısıyla, Mn ilavesi mekanik özelliklerdeki düşüş için tek ve en güçlü parametre değildir. Darbe enerjisi, uzama ve akma dayanımında olduğu gibi en-boy oranı ve tane/mm<sup>2</sup> üzerinde güçlü bir etkiye sahiptir. Ancak akma dayanımı ve uzamanın aksine, en-boy oranı tane/mm<sup>2</sup>'ye göre daha hassastır.

# TABLE OF CONTENTS

LIST OF FIGURES .....	viii
LIST OF TABLES .....	xii
CHAPTER 1. INTRODUCTION .....	1
CHAPTER 2. STATE OF THE ART .....	4
2.1. Production of Aluminum .....	4
2.2. Aluminum Alloys.....	9
2.2.1. Aluminum Silicon Alloys .....	11
2.2.2. Trace Elements in Aluminum-Silicon Alloys.....	16
2.2.3. Effect of Manganese in Aluminum-Silicon Alloys .....	20
2.3. Methods of Wheel Production .....	22
2.3.1. Composite Wheels .....	24
2.3.2. Forged Wheels .....	26
2.3.3. Steel Wheels .....	27
2.3.4. Cast Wheels (Low Pressure Die Casting).....	28
2.4. Heat Treatments .....	33
2.4.1. T6 Heat Treatment.....	35
CHAPTER 3. EXPERIMENTAL.....	37
3.1. Materials.....	37
3.2. Wheel Production.....	40
3.3. Mechanical Characterization.....	46
3.3.1. Tensile Testing.....	47
3.3.2. Hardness Test.....	47
3.3.3. Charpy-Impact Test .....	49
3.4. Microscopic Characterization .....	50
3.4.1. Optical Microscopy .....	52
3.4.2. Scanning Electron Microscopy .....	57
3.5. Casting Simulation .....	58

CHAPTER 4. RESULTS AND DISCUSSION.....	63
4.1. Mechanical Characterization Results.....	63
4.2. Simulation Results .....	84
4.3. Statistical Approach .....	87
CHAPTER 5. CONCLUSIONS .....	93
REFERENCES .....	95

# LIST OF FIGURES

<u>Figure</u>	<u>Page</u>
Figure 2.1. Inputs and outputs of electrolytic production of 1 t aluminum (Source: Tabereaux and Peterson, 2014).....	7
Figure 2.2. Al-Si phase diagram (Source: Sigworth, 2013).....	13
Figure 2.3. (A) Microstructure of hypoeutectic alloy 150x magnification. (B) Microstructure of eutectic alloy 400x magnification (C) Microstructure of hypereutectic alloy 150x magnification (Source: Warmuzek 2004) .....	15
Figure 2.4. Primary and secondary dendrites (Source: Nikolic, Štajduhar, and Čanađija, 2021) .....	16
Figure 2.5. Optical microscopic observation of AlSi7Mg0.3 alloy, precipitates at A) 200x B) 500x (Source: Fasching, 2015) .....	21
Figure 2.6. Preparation steps of polymer matrix composite wheel (Source: Edwin Raja Dhas et al., 2023) .....	25
Figure 2.7. Die parts of automobile wheel. (Source: Zhang et al., 2015).....	27
Figure 2.8. View of a steel wheel (Source: Borecki et al., 2024).....	28
Figure 2.9. Schematic representation of low pressure die casting machine with electric resistance holding furnace (Source: Woycik and Peters, 2008).....	30
Figure 2.10. Molten metal transferring to the holding furnace.....	31
Figure 2.11. Technical drawing of the location for tensile test bar .....	32
Figure 2.12. Drawing of Charpy impact testing.....	33
Figure 2.13. Microstructures of A356 alloy light microscope micrographs; etched with 1% HF. (a) As-cast modified, 150x. (b) As-cast modified, 750x. (c) After heat treatment (T6), 150x . (d) After heat treatment (T6), 750x (Source:Warmuzek 2004).....	34
Figure 2.14. T6 heat treatment (Source:A. Y. Kaya et al., 2021).....	35
Figure 3.1. Optical emission spectrometer.....	38
Figure 3.2. 75 wt.% Mn tablet .....	38
Figure 3.3. Gas fired crucible .....	39
Figure 3.4. Molten metal transfer from melting furnace (“Cevher,” n.d.).....	40

Figure 3.5. Rotary degassing operation .....	42
Figure 3.6. After mold coating operation .....	43
Figure 3.7. Cooling pipes of a die (Kırmızıgöl et al., 2020).....	44
Figure 3.8. LPDC machine .....	45
Figure 3.9. Xray inspection A) hub B) spoke part of wheel.....	46
Figure 3.10. Tensile test bar in DIN 50125 .....	47
Figure 3.11. Points on a cross section of a wheel for hardness test (Kutsal et al., 2023) .....	48
Figure 3.12. Red coloured Charpy specimen region on a wheel .....	49
Figure 3.13. Ceast Charpy impact test machine .....	50
Figure 3.14. Wheel sections for microstructural analyse.....	51
Figure 3.15. A sample of the optical microscopy .....	53
Figure 3.16. Menu of ImageJ.....	54
Figure 3.17. Created images at 100x magnification A) after threshold B) after particle analyse .....	55
Figure 3.18. Results window of a processed image.....	56
Figure 3.19. Ultrasonic cleaning of SEM samples .....	58
Figure 3.20. Startup menu.....	60
Figure 3.21. .CAD data of the mold, wheel, and casting system.....	60
Figure 3.22. Mesh quality .....	61
Figure 3.23. Material definitions .....	62
Figure 4.1. Average hardness test results .....	65
Figure 4.2. Tensile strength results .....	66
Figure 4.3. Yield strength results.....	67
Figure 4.4. Elongation results .....	67
Figure 4.5. Average values of Charpy impact test.....	69
Figure 4.6. Optical microscopy images of hub section a) reference sample at 100x b) batch 1 at 100x c) batch 2 at 100x d) batch 3 at 100x e) reference sample at 200x f) batch 1 at 200x g) batch 2 at 200x h) batch 3 at 200x .....	70
Figure 4.7. Optical microscopy images of spoke section a) reference sample at 100x b) batch 1 at 100x c) batch 2 at 100x d) batch 3 at 100x e) reference sample at 200x f) batch 1 at 200x g) batch 2 at 200x h) batch 3 at 200x .....	71

Figure 4.8. Optical microscopy images of rim section a) reference sample at 100x b) batch 1 at 100x c) batch 2 at 100x d) batch 3 at 100x e) reference sample at 200x f) batch 1 at 200x g) batch 2 at 200x h) batch 3 at 200x.....	72
Figure 4.9. SDAS measurement at 25x magnification .....	73
Figure 4.10. Averages of SDAS per arm .....	75
Figure 4.11. Major axis plotted histograms via ImageJ a) number fraction of hub b) area fraction of hub c) number fraction of spoke d) area fraction of spoke e) number fraction of rim f) area fraction of rim.....	76
Figure 4.12. Circularity plotted histograms via ImageJ a) number fraction of hub b) area fraction of hub c) number fraction of spoke d) area fraction of spoke e) number fraction of rim f) area fraction of rim .....	77
Figure 4.13. Aspect ratio plotted histograms via ImageJ a) number fraction of hub, b) area fraction of hub, c) number fraction of spoke, d) area fraction of spoke, e) number fraction of rim, f) area fraction of rim .....	78
Figure 4.14. SEM images at 45x a) batch 1 4th, b) batch 3 1st, c) batch 2 5th, d) batch 2 6th, e) batch 3 4th.....	79
Figure 4.15. SEM images of the fracture surface a) batch 1 4th 500x, b) batch 1 4th 1000x, c) batch 1 4th 5000x, d) batch 3 1st 500x, e) batch 3 1st 1000x, f) batch 3 1st 5000x, g) batch 2 5th 500x, h) batch 2 5th 1000x, i) batch 2 5th 5000x, j) batch 2 6th 500x, k) batch 2 6th 1000x, l) batch 2 6th 2500x, m) batch 3 4th 500x, n) batch 3 4th 1000x, o) batch 3 4th 5000x.....	80
Figure 4.16. EDX results a) batch 1 4th, b) batch 3 1st, c) batch 2 5th, d) batch 2 6th, e) batch 3 4th .....	83
Figure 4.17. Die filling absolute velocity (m/s) results back and cross-sectional view .....	85
Figure 4.18. Die filling temperature results .....	85
Figure 4.19. Termocouple inserted locations.....	86
Figure 4.20. Termocouple data during solidification and cooling.....	86
Figure 4.21. Significance, predicted values, and sensitivity analysis of elongation .....	91

Figure 4.22. Significance, predicted values, and sensitivity analysis of yield strength .....	91
Figure 4.23. Significance, predicted values, and sensitivity analysis of impact energy .....	92

# LIST OF TABLES

<b><u>Table</u></b>	<b><u>Page</u></b>
Table 2.1. Composition and process differences in bauxite ores (Source: Seetharaman et al., 2014).....	5
Table 2.2. Aluminum production by countries in 2021 (Source: Bhutada, 2022).....	8
Table 2.3. Classification of aluminum alloys (F. C. Campbell, 2012).....	11
Table 3.1. Composition of main elements of batches.....	37
Table 4.1. Hardness test results .....	64
Table 4.2. Arranged data of impact energy .....	68
Table 4.3. Arranged data of SDAS measurements .....	74
Table 4.4. Pearson correlation values between microstructural and mechanical parameters for rim region.....	89
Table 4.5. Pearson correlation values between microstructural and mechanical parameters for spoke region.....	90



# CHAPTER 1

## INTRODUCTION

It has not been more than 150 years since aluminum metal has been produced or used on an industrial scale, even though aluminum is the most abundant metal to be found as well as that after the oxygen and silicon, it is the third most abundant element in the earth's crust. The solid surface of the earth contains 8.1% of its weight. However, it has grown to become the second most important metal producer behind iron and steel in the last century (Schlesinger, 2014; Lide, 2003). Recycling efficiency, high specific strength, thermal and electrical conductivity, machinability, and corrosion resistance led to aluminum has become more and more vital in the automotive industry. As a lightweight material, aluminum provides vehicles with a significant advantage in terms of fuel consumption. Because it's approximately 3 times lighter than steel components.

There are also other lightweight alloys that can be an alternative to aluminum alloys in the automotive industry. The most common examples are titanium and magnesium alloys. Not only aluminum alloys are heavier than magnesium alloys, but also titanium alloys can outperform aluminum alloys when used at high temperatures. R&D studies have being carried out to determine which of these alloys are more suitable for certain components. Aluminum alloys, however, have been used more widely in automobile applications than other lightweight alloys due to their ease of casting, machining and competitive cost at the moment.

Automobile wheels are one of the parts that can be produced as an aluminum alloy in vehicles. The reduced weight of lighter wheels not only enhances the vehicle's performance, but also improves fuel efficiency; lighter wheels decrease the overall weight, therefore requiring less energy to accelerate and brake. On the other hand, In comparison to producing aluminum from raw materials, remelting aluminum requires only 5% of the energy it consumes. With this circumstance, aluminum can provide a clear advantage over environmental regulations that are likely to become more strict in the near future (Başer, 2013; Raabe et al., 2022).

In order to combat climate change and advance environmental sustainability, the European Union (EU) has established the 'Green Deal' as a policy initiative. As part of

this initiative, ambitious targets and strategies are outlined that will help achieve climate neutrality within the EU by 2050 (“Delivering the European Green Deal - European Commission,”). As a result of this, there are some automotive main industry companies have started to use automobile wheels made of 100% recycled aluminum. However, foundries by and large use a mix of primary ingot and secondary sources in a proportionate amount. Thus it can be said that the demand for the cast product in which secondary aluminum is used more can be expected to gradually increase.

In addition to these environmental requirements, automobile wheel is a cosmetic product as well as a safety equipment. For this reason, it has to meet certain mechanical and visual conditions (“Wheel Testing Services,”) and one of the main problems is whether recycled aluminum alloys can meet these mechanical requirements. When recycling aluminum alloy components with increasing amounts of recycled scrap, mixing and thickening of impurities is a serious problem, as cast components must exhibit higher performance. That's why some highly secure automotive components require primary ingots with low iron content as an impurity element (Závodská, Tillová, Švecová, Kuchariková, et al., 2018). Studies have shown that increased iron content and contamination sources cause recycled materials to have lower mechanical properties (Závodská et al., 2018; Kuchariková et al., 2017). Not only increased iron content negatively affect mechanical properties due to the needle-like intermetallics it creates, but also other contaminations during recycling give a question mark over minds in terms of molten metal quality. For this reason, the production of security parts entirely from recycled ingots seems risky and requires a lot of R&D work to prove that the risk has been reduced (Nunes et al., 2023).

It can be possible to minimize harmful effects. Both microstructure modification is commonly carried out in aluminum alloy wheels with elements such as Sr, Sc, Na, and also the needle-like structure is replaced by a more rounded structure after heat treatment (Barrirero, 2019). In addition to that, Mn was used in this study to eliminate the harmful effects of iron content. The presence of Mn will neutralize its damaging effects and annihilate the obstacle to using secondary aluminum for safety equipment like automobile wheels in automotive and other industries. The presence of Mn will neutralize its damaging effects and annihilate the obstacle to using secondary aluminum for safety equipment like automobile wheels in automotive and other industries. As a result of removing the mechanical property constraint, foundries and industrial facility ecosystems

that consume less energy, have less carbon emission, and able to manufacture a safety equipment with the same quality at a lower cost.

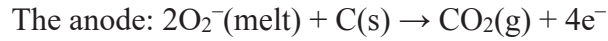
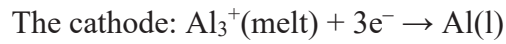
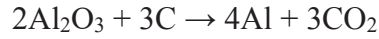
## CHAPTER 2

### STATE OF THE ART

#### 2.1. Production of Aluminum

It's well known that making aluminum has played a pivotal and important role in the history and growth of industries. It's approximately one-third as dense as iron and steel. At room temperature, aluminum has a density of  $2.7\text{g/cm}^3$ , classifying among the light metals. Besides, alloying aluminum gives it special properties, which has allowed it to be used for the design of operational equipment (Kvande, 2015). Although aluminum metal is a recent discovery, its compounds have been widely used throughout the history in various civilizations such as the Egyptians, Persians, and Greeks. The absence and abundance of aluminum depended on the ability of scientists to extract aluminum in the mid-19th century even though it is the third most common element in the crust of the earth by weight. The most familiar story of the first extraction of aluminum is that Charles Martin Hall, from Ohio, developed aluminum's electrolytic extraction process in the late 1800s. On the other hand, it has been revealed that a similar but different process was developed by Paul Héroult in France during the same period. By rapidly heating aluminum chloride ( $\text{AlCl}_3$ ) with potassium amalgam and distilling off the mercury, Hans Christian Ørsted manufactured the first metallic aluminum in the early 1800s. But it was a process hard to be repeatable. Continuing his series of experiments, Hall made a significant discovery: the dissolution of alumina in cryolite (sodium hexafluoroaluminate,  $\text{Na}_3\text{AlF}_6$ ) occurred upon heating it beyond its melting point of  $1000^\circ\text{C}$  within his furnace. It's worth noting that in nature, there are very few minerals of aluminum that are free of oxygen. However, there is one notable exception, namely cryolite. The experiments were not just conducted by Hall, but Héroult also used cryolite as a solvent and succeeded in making his first extraction. The two innovators came to a friendly understanding as a result and the Hall-Héroult process is now commonly known (Geller, 2007).

The overall reaction of his experiment was:



Two separate processes are required to transform the ore into aluminum in the production of primary aluminum. These are the Bayer process, which is the wet chemical caustic leach operation to transform bauxite to alumina and the Hall–Héroult process, whose molten aluminum is produced by electrolysis of alumina dissolved in a molten fluoride electrolyte consisting primarily of cryolite (Schwarz, 2004). The main ore of aluminum today, despite the use of cryolite previously, is bauxite, the source of over 99% of global metallic aluminum (Kvande, 2015).

Table 2.1. Composition and process differences in bauxite ores (Source: Seetharaman et al., 2014)

	Unit	Gibbsite	Böhmite	Diaspore
Process		Bayer	Bayer	Soda-Lime Sinter
Composition		$\alpha\text{-Al}_2\text{O}_3 \cdot 3\text{H}_2\text{O}$	$\alpha\text{-Al}_2\text{O}_3 \cdot \text{H}_2\text{O}$	$\beta\text{-Al}_2\text{O}_3 \cdot \text{H}_2\text{O}$
Alumina Content	%	45-65	47-85	47-85
Silica	%	1-5	2-5	4-16
Alumina/Silica Ratio		19	12	4
Crystal System		Monoclinic	Orthorhombic	Orthorhombic
Density	$\text{g/cm}^3$	2.42	3.01	3.44
Temperature, Rapid Dehydration	$^\circ\text{C}$	150	200-250	450
Energy	Gj/t	7.5-12	11-16	34-45

It was discovered by Bayer that alumina in bauxite can be dissolved by heating it under pressure with a mixture of sodium hydroxide in an autoclave. This creates a solution called sodium aluminate. Later, aluminum hydroxide can be made to fall out of this solution by adding alumina hydrate. The resulting hydrate can be easily filtered, washed, and calcined to make a high-quality crystalline alumina. To make aluminum using the Hall–Héroult process, a significant quantity of alumina must be generated. It takes

approximately 4 tons of bauxite to produce 2 tons of alumina, and nearly 2 tons of alumina are needed to produce 1 ton of aluminum metal. In Bayer plants, the two most substantial expenses per ton of alumina are bauxite and fuel. The process has five key steps. First, crushed ore is mixed with a caustic soda solution in order to make a slurry. This slurry, containing aluminum-bearing minerals from bauxite, is then pumped into a digester, where the aluminum compound is dissolved and extracted. The hot slurry, now with sodium aluminate solution, goes through flash tanks that lower the pressure. Bauxite is added during digestion to reach a certain alumina level, ensuring stability as it moves through the flashing and clarification stages. During clarification, the solution is pumped into a tank where the caustic will not dissolve the oxide impurities, and the liquor containing sodium aluminate is separated from the insoluble impurities. After cooling the filtered liquid, it goes through big tanks where solid seed crystals are added. By using evaporation, a cake-like substance called aluminum hydroxide is obtained. Finally in calcination step, a quarter of the required energy is consumed. Aluminum hydroxide is washed, filtered, and calcined to remove the chemically bonded water from hydrate and form anhydrous alumina crystals in the process (Seetharaman et al., 2014; Grjotheim et al., 1982). After all, in the electrolysis of aluminum oxide, molten cryolite is dissolved in aluminum oxide, and a direct electric current is passed through the mixture to produce pure aluminum metal.

Four units of bauxite must be given to the system as input to produce one unit of aluminum is shown in Figure 2.1. Also as an anode, carbon has a special role in the production process, being responsible for the reduction of alumina. Its moderate electrical conductivity and the fact that it does not produce chemically undesirable reactions make it suitable for use as an anode material.

Anodes by and large are made of baked the mixture of petroleum coke aggregate and a binder. Diminishing the coke quality also raises questions about carbon sources. This reduction in quality also means an increase in sulphur content, which makes the process gases emitted during electrolysis more environmentally harmful, forcing the industry to look for other alternatives.

Aluminum production faces three major challenges worldwide: the economy, exceptional energy consumption, and environmental protection. One of the reasons for the majority of the problem is that in the early years of aluminum production, these issues were not very popular and therefore mitigation measures were not given much thought.

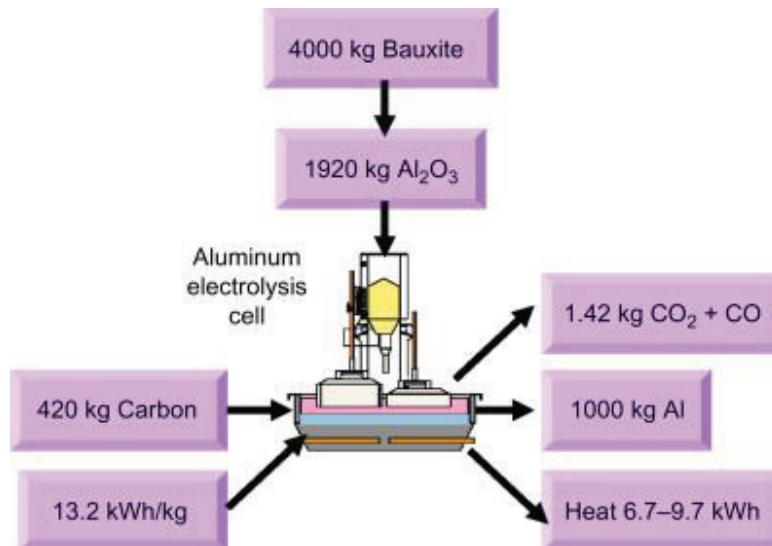


Figure 2.1. Inputs and outputs of electrolytic production of 1 t aluminum (Source: Tabereaux and Peterson, 2014)

Metal prices, energy costs, environmental regulations and emission restrictions, which were much lower in the past, were also considered to be at levels that did not cause concern on these issues. From a business standpoint, most aluminum companies are currently working on programs that will decrease production costs and increase margins, which will improve operations and increase productivity. Additionally, reducing output and shutting down inefficient units are part of a plan to reduce capacity. From an energy perspective, aluminum production is quite electrical energy intensive. For instance, the aluminum smelters of world now consume about 3.5% of the global electric power consumption. In the other words, primary aluminum industry has always relied on cheap electric power to drive production. Power is the main driver of costs, which differ greatly throughout producers. Usually, energy makes up around 30% of the total cost of primary aluminum production (Kvande, 2015). Such inefficient energy consumption is mainly attributed to two reasons: To prevent the back reaction of aluminum with  $\text{CO}_2$  gas thereby decreasing the amount of metal produced, the anode-cathode distance ought to be adjusted above a specific minimum value. Ohmic resistances in the anodes and cathode contribute to the high cell resistance. The other reason is keeping the temperature low enough in order to shield the sidewall material from chemical assault by the electrolyte, high heat losses through the cell sidewalls are required. After all considering the process environmentally, eventhough non-reactive material cannot be found to not form carbon

dioxide as an off-gas, collecting the CO<sub>2</sub> that releases during the process may be the alternative solution. Besides, energy recovery is another challenge. Outgoing heat that comes from sidewalls of cells should be made usable for further operations.

Aluminum is produced by alumina through electrolytic reduction as mentioned formerly. Briefly, after the electrolysis molten aluminum is ready for refining before being molded into its different dimensions.

Table 2.2. Aluminum production by countries in 2021 (Source: Bhutada, 2022)

Country	2021 Aluminum Production (tonnes)	% of total
China	39 000 000	59%
India	3 900 000	6%
Russia	3 700 000	6%
Canada	3 100 000	5%
United Arab Emirates	2 600 000	4%
Australia	1 600 000	2%
Rest of the World	12 660 000	18%
<b>Total</b>	<b>66 560 000</b>	<b>100%</b>

China is both the greatest producer and consumer of aluminum worldwide. India is the second-largest producer, but its output is barely one-tenth that of China. The requirement for aluminum has grown along with the material's expanding application areas. In 2021 alone, about 66 million tonnes of aluminum were produced, as shown in Table 2.2, which is a proof of the growing production and demand for aluminum. It is anticipated that this production will rise even more due to the need for aluminum. Considering the energy consumed in primary aluminum production, harmful gases emitted to nature and process efficiency, there is a necessity to find less harmful, cheaper, new sources and efficient processes every day as discussed earlier. One of the concepts that can solve these problems is undoubtedly the widespread use of recycling and secondary aluminum production. The secondary aluminum production process uses either new, old scrap and drosses. Various types of furnaces are used for melting aluminum scrap based upon the type of scrap that is collected and the required final grade. Scrap is often melted in rotary furnaces beneath a layer of liquid melting salt in order to produce casting alloys. It consists of scrap preparation and remelting basically. In scrap



preparation, sorting is the most important step such as removing the iron included scrap by using magnetic separator. Afterwards, relying on the alloy type, the variety of furnace to be used is determined. Because, by and large different furnace types are used for wrought alloys and cast alloys. In a remelter, wrought aluminum is made mostly from clean, sorted wrought alloy scrap. Refining comes after the rotary furnace-based alloy manufacturing process.

Considering the volumes of energy in primary and secondary production, the energy consumption to produce recycled aluminum can be reduced up to 95% of that required to produce primary aluminum, also which means that CO<sub>2</sub> emissions are significantly reduced. Aluminum has one of the highest recycling rates of any material. In Europe, the building and automotive sectors recycle at above 90%, yet only 75% of aluminum cans are recycled (“Circular Aluminium Action Plan” 2020). The process of converting alumina to aluminum metal needs about 13 kWh/kg (46,800 MJ/t) of electricity. However, in the recycling context, the industry norm of 2000 Btu/lb (2110 MJ/t) that is frequently cited usually only covers the melting and casting of recovered aluminum. On the low end of the energy usage range, inefficient reverb furnaces may use as much as 4220 MJ/t, while rotary furnaces with oxy-fuel burners are capable of using as low as 580 MJ/t. The gathering and delivery of the feed materials to a recycling plant also require energy. Furthermore, several preprocessing methods may be used, requiring as an input. The goal of maximizing aluminum metal recovery tempers this urge to use less energy. The heat letting out due to the oxidation of aluminum, and theoretically melting the entire load might be achieved by oxidizing just 4-5 percent of the aluminum. Since aluminum has a far higher value than the heat produced during oxidation, every attempt is taken to guarantee that lower energy consumption for melting the metal results from appropriate thermal practices rather than recovery being sacrificed (Seetharaman et al., 2014).

Consequently, we ought to promote sustainability and recover and recycle all aluminum scraps and by-products, just like we should with any other resource. Recycling aluminum benefits the environment and the economy.

## **2.2. Aluminum Alloys**

Fundamental alloy design is a continuous process since industrial applications always require greater outcomes. The aluminum industry has recognized its primary

sectors as building and construction, transportation, consumer goods, electrical engineering, machinery and equipment, packaging. For a very long period, the only material groups utilized in structural materials were steels and cast irons. Thanks to its lower density, lower melting point, specific strength, corrosion resistance, and malleability compared to steel, aluminum has largely displaced ferrous alloys in various applications, particularly in the automotive industry. Due to weight constraints and a push to enhance payload capacity, manufacturers have extensively incorporated aluminum into the design of cabs, trailers, and trucks. Sheet alloys play a vital role in constructing truck cab bodies, while extruded stringers, frame rails, and cross members further reduce dead weight. Typically, extruded or formed sheet bumpers and forged wheels are employed. Aluminum fuel tanks offer benefits such as weight reduction, corrosion resistance, and an appealing appearance. Additionally, castings and forgings are widely utilized in engine and suspension systems (ASM Handbook, 1990). Since aluminum is insufficient to meet basic properties such as hardness and strength when used in its pure form because pure aluminum is quite ductile and soft, alloying is performed to improve the targeted properties by alloying with elements such as silicon, magnesium, copper, and zinc.

From the recycling point of view, unfortunately the removal of most alloying elements from molten aluminum makes them hard to recycle into anything other than cast alloy. Therefore, they shouldn't be collected and melt wrought and cast alloy scraps into the same batch. Wrought alloys has a lower amount of alloying elements. As wrought and cast alloy scraps are collected and mixed together, chemical composition of recycled mixture metal would have less alloying elements proportional to the quantity. This causes a diminishment in mechanical properties such as hardness, and yield strength and as a result, rendering all the anticipated benefits of recycling meaningless (Schlesinger, 2014).

Aluminum alloys are classified under two different categories: wrought and cast alloys. These alloys are numbered according to the most abundant element after aluminum as shown in Table 2.3. These alloys can also be analysed in two different groups: heat treatable and non-heat treatable. Wrought alloys are usually intended for the production of wrought products by hot or cold working such as rolling, extruding, forging and drawing. According to the European designation system 4 digit system is used and the first digit describes the alloy group. Last two digits identify the alloy or indicate the aluminum purity. The second digit indicates modifications or impurity limits. On the other hand, for cast alloys composition is described by 5 digit separated by a decimal point at the end of the fourth digit ("The Aluminum Automotive Manual", 2002).

Considering hardenability by heat treatment, 1xxx, 3xxx, 5xxx, and the majority of the 4xxx wrought alloys are not able to be strengthened by heat treatment. The 1xxx, 3xxx, and 5xxx alloys can be strengthened by strain hardening, solid solution strengthening, and grain size controlling. The 2xxx, 6xxx, and 7xxx alloys are strengthened by precipitation hardening.

Table 2.3. Classification of aluminum alloys (F. C. Campbell, 2012)

Series	Aluminum content or main alloying element
<b>Wrought alloys</b>	
1xxx	99% min
2xxx	Copper
3xxx	Manganese
4xxx	Silicon
5xxx	Magnesium
6xxx	Magnesium and silicon
7xxx	Zinc
8xxx	Others
<b>Cast alloys</b>	
1xx.0	99% min
2xx.0	Copper
3xx.0	Silicon with copper and/or magnesium
4xx.0	Silicon
5xx.0	Magnesium
7xx.0	Zinc
8xx.0	Tin
9xx.0	Other

### 2.2.1. Aluminum Silicon Alloys

As well as wrought aluminum alloys, there are over 200 cast aluminum alloys available. Compared to wrought alloys, cast alloys usually have higher alloy contents. The industrial use of the 3xx.x and 4xx.x series, whose main alloying element is silicon, is quite widespread and is increasing day by day. These alloys containing from 4% to

22% Si comprise more than 90% of all castings and the maximum dissolution limit of silicon in aluminum is 1.65% (Zolotarevsky, Belov, and Glazoff, 2007). The most critical properties of hypoeutectic aluminum alloys are the decrease in melting temperature and increase in fluidity with the increasing silicon content. Due to the Al-Si alloys with high fluidity values are more preferred for thin-section parts or for casting into a permanent mold where solidification in the part may be faster than in other parts, since feeding and filling the mold may be problematic. Increased fluidity allows thin sections and complex parts to be cast. High silicon alloys have low thermal expansion coefficient, high corrosion resistance, good weldability, and high wear resistance. In additive manufacturing field, Al-Si alloys are increasingly gaining attention for their potential in producing complex geometries with high precision. However, their adoption in additive manufacturing processes such as selective laser melting or powder bed fusion has been limited compared to other alloys like titanium or stainless steel. Despite the current challenges, Al-Si alloys are promising for additive manufacturing applications particularly in industries where lightweighting, thermal management, and complex part geometries are critical factors (Kan et al., 2019; Shakil et al., 2021). In addition to that, silicon plays a substantial role in minimizing the solidification shrinkage of aluminum because it needs longer time to solidify, with negligible influence from other alloying elements on the shrinkage phenomenon during solidification after the casting operation. Therefore, they find their place in automotive applications requiring high temperature, and complex shaped products such as cover plates, motor shells, brackets. (Kaufman and Rooy, 2004).

The Al-Si binary equilibrium phase diagram has a eutectic point at the 12.6 wt.% Si content at 577°C according to Figure 2.2. If the composition of Si is lower than 12.6 wt.% named hypoeutectic, if it is between 15 and 20 wt.% called hypereutectic. Besides, these alloys have between 10 and 13 wt.% silicon they described as an eutectic alloy. These alloys, often eutectic in nature and typically composed of copper, magnesium, and occasionally nickel, possess several desirable characteristics. They exhibit a narrow freezing range, ensuring consistent casting, and boast excellent fluidity, facilitating ease of manufacturing. Moreover, they offer commendable wear resistance and maintain good ductility, particularly when not subjected to alloying and high-temperature treatments for enhancing strength. These alloys are extensively utilized in piston production, playing a vital role in achieving the reliability and performance standards demanded by internal combustion engines (Sigworth, 2013).

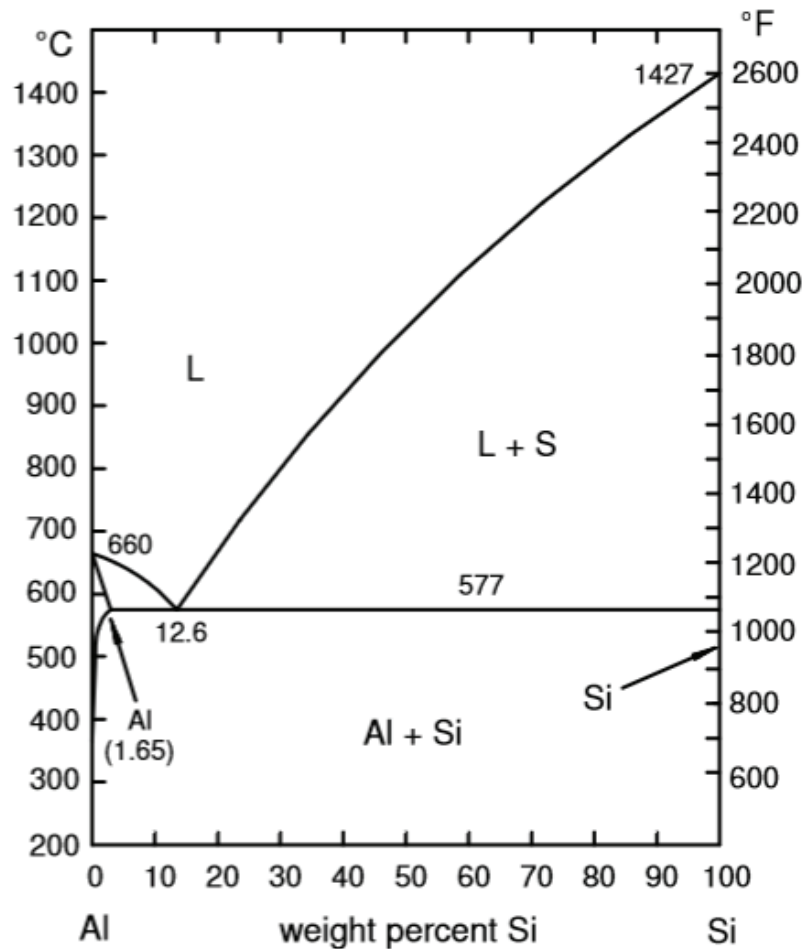


Figure 2.2. Al-Si phase diagram (Source: Sigworth, 2013)

In the region where silicon is less than 1.65 wt.%, an  $\alpha$  aluminum phase is observed and less silicon gives ductility to the structure. The microstructure of hypoeutectic Al-Si alloys consists of a dendritic  $\alpha$  primary phase and a eutectic phase distributed between these phases. The  $\alpha$  aluminum solid solution is the matrix of cast aluminum silicon. It solidifies as non-faceted dendrites, aligning with the crystallographic lattice structure of aluminum. This lattice system adopts a face-centered cubic (fcc) arrangement, accommodating four atoms within each elementary cell. The atoms are bound together by metallic bonds, which exhibit isotropy and relatively modest bonding energy (Askeland et al., 2013). The silicon precipitates within commercially used aluminum-silicon alloys are predominantly pure, exhibiting faceted crystalline structures. These formations vary in appearance, appearing either as primary, dense precipitates in hypereutectic alloys or as branching plates within the aluminum-silicon eutectic phase. In essence, these alloys consist of a ductile, continuous matrix of  $\alpha$ -aluminum solid solution, interspersed with silicon precipitates of differing morphologies, contributing to

the material's overall hardness (Warmuzek, 2004). Al-Si alloys generally used as casting alloys in the range of 5-11 wt.% in the industry all this given the advantages of the properties and chemical composition. There are various additions and processes involved in modifying alloy properties to meet the desired specifications for the end product. Among these, ensuring that the liquid metal is sufficiently clean is paramount. Hydrogen is a problem for Al-Si cast alloys. Because hydrogen is able to soluble in the matrix. It's solubility changes drastically at approximately 750°C. The solubility of this gas is notably higher in the molten metal than in its solid form. It can be regulated through alterations in processing. This is achieved through treatments such as degassing, to minimize aluminum loss by using fluxes, and isolating the liquid metal from exposure to air, which are commonly employed (C. Li et al., 2023). Importantly, it is crucial to transfer the liquid metal very slowly before casting operation, and measures should be taken to prevent turbulent flow within the mold and the overlapping of liquid metal layers (J. Campbell, 2004; Tigli and Dispinar, 2023). Once metal cleanliness and turbulence-free flow are ensured, the effects of alloying elements on mechanical properties become more apparent, leading to observable enhancements.

In figure 2.3, the darker regions within the microstructures correspond to eutectic silicon, which contributes to the hardness of the matrix but tends to be more brittle. Conversely, the lighter regions represent  $\alpha$  aluminum. In hypoeutectic alloys, Figure 2.3 (A), the solidification process results in the formation of dendrites, clearly visible in the microstructure. The black areas observed at the boundaries of dendrites and above the grey regions in the hypereutectic alloy are indicative of defects, such as microporosity, shrinkage, or gas porosity, which can arise during production.

Silicon serves as the primary alloying element in the majority of aluminum casting alloys, imparting excellent castability, hot tear resistance, and wear resistance to the aluminum. Addition of silicon also leads to a decrease in specific gravity and coefficient of thermal expansion. The most important feature observed in hypoeutectic cast alloys is the liquid metal fluidity, which increases with increasing silicon content. Thanks to this increase, the liquid metal can fill through the complex and thin sections in the molds without any difficulty, and thus, if the mold and molten metal temperature are kept under favourable conditions, defects such as misrun due to lack of fluidity can be avoided.



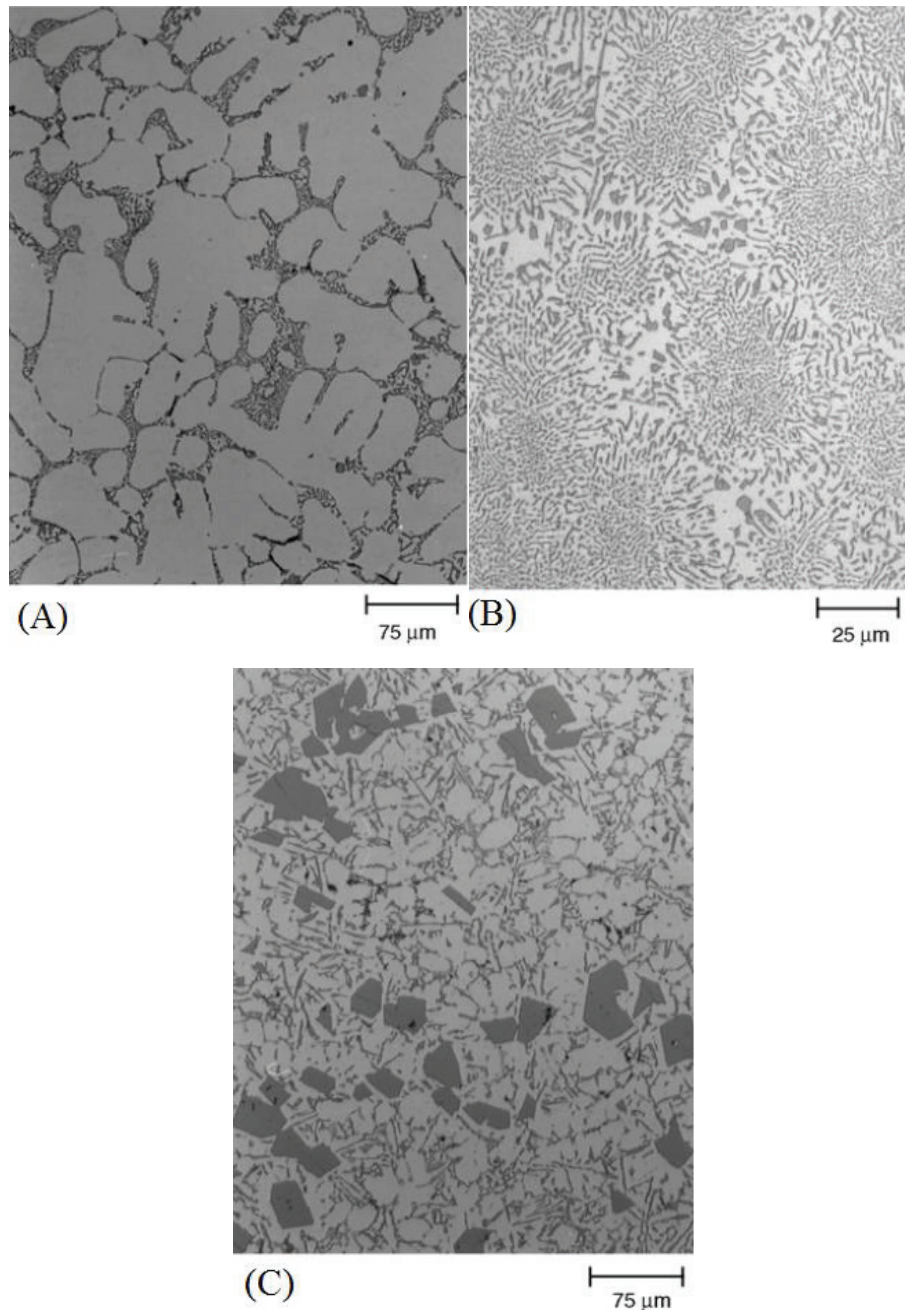


Figure 2.3. (A) Microstructure of hypoeutectic alloy 150x magnification. (B) Microstructure of eutectic alloy 400x magnification (C) Microstructure of hypereutectic alloy 150x magnification (Source: Warmuzek, 2004)

Changes in the microstructure and their impact on mechanical properties are typically associated with the size and shape of eutectic silicon grains. Consequently, factors like challenging machinability and increased hardness can often be attributed to silicon, although it may not be the only contributing factor (Robles Hernandez, Herrera Ramírez, and Mackay, 2017; Y. Kaya et al., 2019).

Another concept that should be mentioned is Secondary dendrite arm spacing.

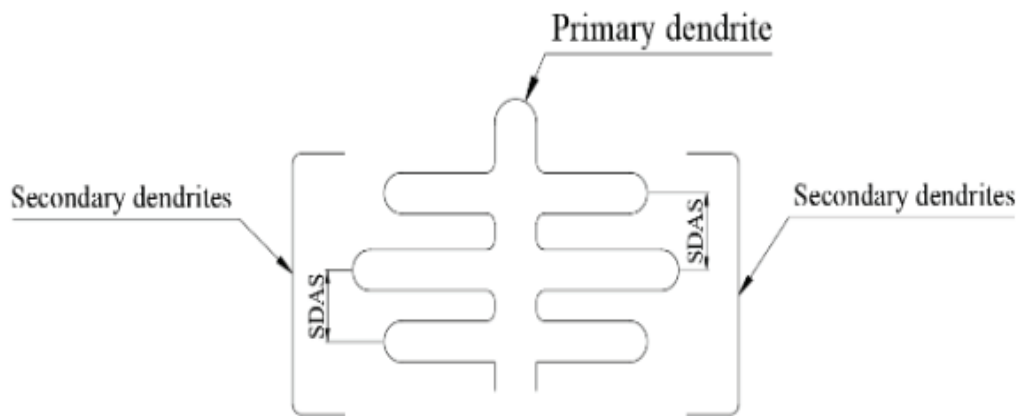


Figure 2.4. Primary and secondary dendrites (Source: Nikolic, Štajduhar, and Čanađija, 2021)

SDAS is an abbreviation of secondary dendrite arm spacing. SDAS is related to the solidification rate and the composition of an alloy, also there is a relationship between mechanical properties and SDAS. Not only the mechanical properties are strongly dependent on casting defects like porosity or oxide films, but also Si particle distribution and size, and the amount of Fe-rich brittle intermetallics. The optical microscope is capable of measuring SDAS.

## 2.2.2. Trace Elements in Aluminum-Silicon Alloys

Aluminum-silicon (Al-Si) alloys employ various alloy additions to manage and enhance properties such as hardness, strength, fracture energy, ductility, and corrosion resistance. However, it's crucial to enhance these properties without compromising other important factors like fluidity, machinability, and wear resistance.

### 2.2.2.1. Magnesium

Magnesium plays a critical role for hardness and strength in some alloys with heat treatment. Because it is a precipitation hardener. These alloys may also contain Cu and Ni. The hardening phase,  $Mg_2Si$ , demonstrates an advantageous limit of solubility after which further reinforcement ceases or the matrix undergoes softening. After a certain heat



treatment whose are usually T5 and T6 heat treatments, the precipitates undergo an aging to convert into  $Mg_2Si$  and helps to reduce the residual stress of the structure that can stealthily cause catastrophic failures. Aging can occur naturally (T5) or artificially (T6) (Pezda, 2015; Özyaydın et al., 2019; Kutsal et al., 2023).  $Mg_2Si$  is evenly dispersed, enhancing the uniformity of the alloy and consequently elevating its mechanical characteristics. Even though the addition of Mg should be adjusted the right amount for the required features, it should not be forgotten that impacts the ductility negatively It is advised to maintain magnesium content within the range of 0.6 to 3 wt.% (Riahi and Alpas, 2006). In addition to that, it has been noted that the hardness of A356 alloy rises with magnesium levels reaching around 0.9 wt% (Şimşek and Özyürek, 2019). However, in the manufacturing of safety components, it's important to recognize that although high magnesium content boosts hardness during processes like machining and flow forming, it also poses the risk of reducing tool tip longevity and potentially causing hard-to-detect cracks as the parts near completion.

#### **2.2.2.2. Copper**

Copper plays a significant role as an alloying element in aluminum-silicon alloys, typically enhancing their strength in as-cast or heat-treated situations substantially like magnesium. It aids in precipitation hardening, thereby boosting the strength and hardness of the alloys. However, presence of copper may diminish ductility. The maximum solid solubility of Cu in aluminum is around 6 wt.% at 546 °C. For optimal precipitation hardening outcomes, it is suggested to adding copper ranging between 2 and 4 wt%. In general, copper tends to diminish resistance to corrosion. Additionally, the inclusion of copper decreases resistance to hot tearing and prevents castability (ASM Handbook, 1990; Haque and Maleque, 1998).

#### **2.2.2.3. Boron**

Boron is often used to improve mechanical properties by enabling the formation of finer grains. However, since it is a small element and additions are made at ppm levels, its determination in the chemical composition may not always be accurate. When combined with other metals, boron forms borides. Titanium boride acts as stable

nucleation points, facilitating interaction with grain-refining phases. Boron is usually added to aluminum alloys in the form of master alloy. It also has been studied a powder form of the master alloy (Pozan, 2022). Master alloys added in triplinary in the form of Al-Ti-B are suspected to cause Si poisoning effect. For this reason, a binary Al-B master alloy was investigated. For optimum grain refinement in aluminum foundry alloys with boron additions, it's preferable for them to be devoid not only of titanium but also other trace elements like Zr. Most importantly, this article given the current findings, the deliberate addition of titanium in foundry alloys should be reassessed. Also, in other article it was observed that boron and strontium added separately at 300 ppm provided the best grain refinement (Birol, 2014a; 2014b; Nogita, McDonald, and Dahle, 2003).

#### **2.2.2.4. Titanium**

Titanium is commonly utilized to enhance the grain structure of aluminum casting alloys, typically alongside smaller quantities of boron. It's important to have an excess of titanium beyond the stoichiometry of  $TiB_2$  to achieve optimal grain refinement. In some cases, titanium is used in concentrations higher than necessary for grain refinement to mitigate cracking. In molten metal, there should be a sufficient amount of titanium to initiate the nucleation of  $TiAl_3$  before the transformation of  $\alpha$ -Al occurs to reduce the size of grains (Mohanty and Gruzleski, 1995; C. Li et al., 2024).

#### **2.2.2.5. Strontium**

Strontium is employed to alter the morphology and microstructure of eutectic silicon, particularly in hypoeutectic Al-Si alloys. Increased addition levels, like more than 400 ppm, are linked to the occurrence of casting porosity, particularly in processes or thick-section parts where solidification takes place at a slower rate. Moreover, higher levels of strontium may negatively impact degassing efficiency. (ASM Handbook, 1990). Altering a coarse and elongated grain (needle like) to a finer morphology (chinese script) which leads to improved mechanical features. Additionally, improved feeding effectiveness may be observed with modification. However, it is important to monitor the holding time of strontium, as its effectiveness may diminish over time. (Özaydin, Armakan, and Kaya, 2018). On the other hand, it was observed that there was no greater

effect on hot tearing than bifilms that deteriorate metal quality (Uludağ, Çetin, and Dispınar, 2017).

#### **2.2.2.6. Iron**

Especially for secondary Al alloys, it is considered the impurity element. It is considered undesirable because intermetallic phases formed by iron during solidification have a negative impact on the mechanical properties of alloys, particularly their ductility. The influence of iron on aluminum varies depending on the quantity of iron present in the alloy and the structure of the iron-formed phases.  $Al_5FeSi$  ( $\beta$ -phase) has a harmful morphology like needle-shaped or plate-shaped. Its shape is a stress concentrator and may be responsible for cracks because it's also brittle, therefore it decreases the impact energy (Karabulut et al., 2023). In recycled alloys, the iron concentration can reach up to 1 wt% (Davis, 1993). However, in future, this concentration should be increased due to the growing necessity of utilizing secondary sources. By gradually increasing the use of ferrous sources, we can avoid sudden production bottlenecks caused by the adverse effects of the  $\beta$ -phase, enabling us to confidently embrace ferrous sources in production processes. This phase can be controlled with alloying or cooling rates (Robles Hernandez, Herrera Ramírez, and Mackay, 2017; Wu et al., 2020; Sanchez et al., 2023; Závodská, Tillová, Švecová, Chalupová, et al., 2018).

#### **2.2.2.7. Rare Earth Elements**

Various elements are recognized for their ability to induce chemical modification; for instance, strontium and sodium are notable examples. Conversely, for the purpose of reducing grain size through alloying, elements such as boron and titanium are widely employed in today's industrial practices. In order to create an alternative in terms of a possible supply crisis, elemental effect and cost, rare earth elements have been widely tested in recent years due to their modification and grain size reduction effect. It is observed that the efficacy of modifying the mechanical properties of A356 alloy with 1.0 wt.% lanthanum is comparable to that achieved with the commercially available modifier, Sr (Tsai et al., 2009). Apart from that, Erbium (Er), Scandium (Sc), and Yttrium (Y) are also considered rare earth elements (REEs) that are commonly researched. When 0.1 wt.% of Sc is added along with Vanadium (V), it enhances fluidity (Can Dizdar et al., 2022).

Additionally, the inclusion of Erbium may lead to a relative increase in Ultimate Tensile Strength (UTS) and elongation. Researchers have experimented with different amounts of Lanthanum, Cerium, and their combination. Increasing the intermetallic content, was found to reduce feedability, consequently raising shrinkage and promoting porosity formation (Mahmoud et al., 2018). Sc is not only has advantageous for fluidity but also the microstructure refined by Sc eradicated the formation of Fe-intermetallics and enhanced tensile strength features like the Mn do. It is observed that the harmful Fe intermetallics turned into Chinese script morphology (Xu et al., 2015). Other REEs have also special effect on cast aluminum alloys especially generally studied A356 alloy. The grain size decreases from 443 to 196  $\mu\text{m}$  with the increasing of Hf content with the help of AlHf master alloy (H. Li et al., 2016). La and Yb are studied. The effect of modification declined when the pouring temperature increased above 730°C. almost no modification was observed until 0.3 wt.% addition (Song et al., 2019). Gadolinium (Gd) belongs to a distinct group of rare earth elements, and researchers have explored its impact on modification and strength properties. They observed a grain refinement effect, though its influence on tensile properties was minimal when added to the alloy without undergoing heat treatment (Shi et al., 2015).

### **2.2.3. Effect of Manganese in Aluminum-Silicon Alloys**

In Cu-free alloys, the amount of Mn can reduce the negative effects of Fe. In Al-Si alloys with medium or high Fe content, it can induce the formation of  $\alpha$ -phase instead of the damaging  $\beta$ -phase. With three elements (Si, Fe, Al) it creates a  $\text{Al}_{15}(\text{Mn}, \text{Fe})_3\text{Si}_2$  intermetallic which is known as Chinese script phase. Iron tends to combine with other elements to form various types of intermetallic phase particles. Also a critical concept of Fe level for Al-Si alloys was defined and empirically formulated by Taylor. The calculation is based on the relationship between silicon and iron content (Taylor, 2004). It indicates the threshold at which the presence of iron above a certain level of silicon content becomes detrimental, expressed as a percentage. Mn is a common alloying addition used to neutralize the effect of iron and change the morphology, type of intermetallic phases. It has been reported that if the iron content exceeds 0.45% by weight, the Mn content should not be less than half of the iron. Studies have indicated that when the iron content surpasses 0.45% by weight, the manganese content should be maintained

at no less than half of the iron content (Ak, 2012; Muşdal, 2018). Besides, cooling rates alters the form of the intermetallic. Higher than 20 °C/s can provide less defective alpha phase of iron (Becker et al., 2019). Not only the effect of cooling rates alters the morphology of intermetallic of iron, but also alloying has been studied a lot. The effect of Mn, Fe, Y was investigated, sample alloys were prepared using Al–20%Si–2.5%Fe–2%Mn master alloy and Y. Since Y and Mn are used together, they increased the tensile strength and elongation values on the safety equipment of automobile (Q. Li et al., 2020). Also, the triple effect of the use of Mn, Cr, Be was examined. No positive results were obtained from the corrosion test (Zabalegui et al., 2014). The advantages of this process are not consistently evident. An excess of manganese might decrease the presence of  $\beta$ -phase and encourage the formation of  $\alpha$ -phase, potentially enhancing ductility. However, it can also result in the development of hard spots and machining challenges. Additionally, manganese additions do not consistently enhance the ability to cast or reduce porosity in alloys with high iron content.

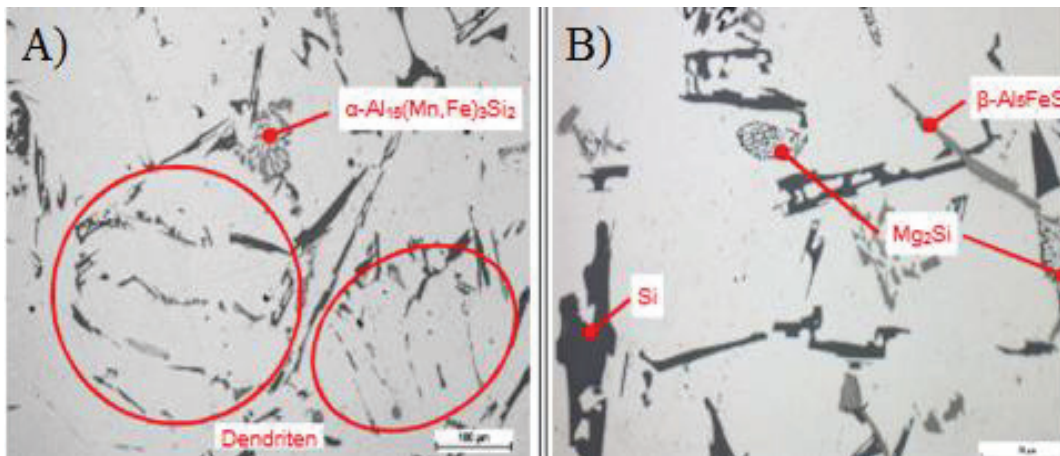


Figure 2.5. Optical microscopic observation of AlSi7Mg0.3 alloy, precipitates at A) 200x B) 500x (Source: Fasching, 2015)

The impact of manganese is influenced by the overall composition of the alloy. Given the absence of a practical means to separate iron from aluminum, adjusting the chemical composition and managing local cooling rates offer a solution to convert the coarse and needle-like iron  $\beta$ -phase into the  $\alpha$ -phase, known as Chinese script. This approach effectively mitigates any detrimental effects on the alloy's mechanical properties (Muşdal, 2018).

### **2.3. Methods of Wheel Production**

Wheels, an ancient invention, are circular frames designed to rotate on an axis. According to the IATF 16949 Quality Management System, automobile wheels are considered safety equipment and must undergo various tests to ensure their suitability for use in cars. The wheel serves as the main suspension component of the vehicle, bearing both static and dynamic loads throughout its operation. Therefore, the selection of materials must be made with careful consideration. In recent times, the automotive industry has seen a rise in the significance of lightweight materials, driven by stringent fuel economy and emissions regulations. Aluminum alloy materials are extensively employed in the automobile wheel sector owing to their notable specific strength, resistance to corrosion, and lightweight properties. Additionally, alternative alloy choices such as magnesium alloy exist. Despite magnesium alloy being lighter than aluminum, challenges are encountered during the manufacturing process of magnesium alloy wheels. Magnesium die casting is a specialized manufacturing technique utilized for creating metal parts and components from magnesium alloy. Among the primary issues associated with magnesium casting is its heightened reactivity during melting and its tendency to be more costly than other commonly used casting alloys (Fleming, 2012). Enhancing the range of electric vehicles, reducing weight is a key strategy. This is because lighter vehicles require less energy to move, thus increasing efficiency and extending the driving range on a single charge. However, it's not just about making parts lighter; they also need to maintain or even improve performance and durability. One approach to reducing weight is through the use of advanced materials with high strength-to-weight ratios, such as magnesium alloys and carbon fiber composites. These materials offer significant weight savings while still providing the necessary structural integrity and durability required for automotive applications. Additionally, the design of components plays a crucial role in weight reduction. Topological optimization is a computational design approach that allows engineers to create highly efficient structures by removing excess material while maintaining structural integrity. This can result in complex, lightweight designs that maximize strength and minimize weight. However, there are limitations to how much weight can be reduced through design optimization alone. At a certain point, further reductions may compromise the performance or safety of the component. In such



cases, alternative materials or manufacturing processes may need to be considered (Korkut et al., 2019; 2020).

The lightweighting of automobiles is a notable trend also in application. An alternative approach involves producing lighter structural components by altering the production technique while retaining the same primary material group. Both cast and forged automotive parts can be crafted using aluminum alloys. While the composition of the alloy differs between wrought and cast variants, the base material remains aluminum. Prior to forging, the material is heated below solidification temperatures, and the forging process occurs without the presence of liquid at relatively lower temperatures compared to casting. However, this doesn't necessarily mean of lower costs compared to casting. Generally, the energy consumption associated with forging is considerably higher than that of casting. Despite this, forging remains a widely adopted method for lightweighting, enabling the creation of thinner sections with excellent mechanical properties (Öztürk, 2008). About 20 years ago, aluminum alloy wheels were widely produced by gravity die casting, but they were also produced by cutting the runners, which requires a lot of material and is an additional process. Despite all this, the most profitable production method for the manufacturer of an average automobile wheel that meets the general expectations of OEM brands, except for special applications and premium customer expectations, is the production of wheels with low pressure die casting. Nonetheless, polymeric composites, comprising a polymeric matrix and fibers, exhibit exceptionally high specific strengths, making them valuable for vehicle construction. Consequently, these composites find widespread use in automotive applications. Unfortunately, polymer composite applications in the automotive industry come with their own set of drawbacks. Unlike aluminum alloy, they are not conducive to mass production and come with higher associated costs. Steel wheels, being the traditional choice for automobiles, play a vital role in propelling vehicles and offer a simpler, more cost-effective alternative to alloy wheels. Nevertheless, their production involves multiple manufacturing steps to shape a basic steel plate into a wheel suitable for various automotive applications. Similar to other commercial options, ensuring the safety and quality of these wheels before reaching consumers necessitates employing a variety of tools and measures during production to meet rigorous standards. However, challenges such as corrosion susceptibility and significantly greater weight compared to aluminum are pressing issues that the automotive industry faces.

### 2.3.1. Composite Wheels

While the primary focus remains on polymer composites due to the fiber matrix of composites are lighter and have higher tensile strength than metallic materials, there are ongoing experiments involving metal matrix composites. The increasing appeal of materials exhibiting high tribological performance at a low cost globally is driving interest in metal matrix composites. Adjusting parameters such as molten metal temperature, holding time, and pressurization presents significant challenges. Stir casting stands out as a widely utilized production technique in metal matrix composites. Through continuous stirring at elevated temperatures over an extended period, particles aggregate in the molten state. This method, typically employing ceramic powders (SiC, Al<sub>2</sub>O<sub>3</sub>, B<sub>4</sub>C, fly ash etc.) has shown potential for enhancing hardness, impact energy, and excellent fatigue life (Rao et al., 2019). Other frequently employed production methods for preparing composites include centrifugal casting, powder metallurgy, and squeeze casting. The primary obstacle in manufacturing metal matrix composites lies in achieving a homogeneous mixture. Special modifications to traditional techniques are necessary to achieve this goal. Metal matrix composites find application in various components such as brake drums, and gears (Singh et al., 2021). However, their suitability for automobile wheels remains a research and development project. The feasibility of mass production is still under scrutiny, considering alternative production methods and ongoing advancements in the field.

Fiber-reinforced polymer composite materials are rapidly becoming popular in both fundamental research and practical use. They offer cost-effectiveness, and full or partial recyclability. By utilizing carbon-epoxy composite materials, the weight reduction is approximately 10% compared to aluminum alloy wheels (Wilczynski et al., 2018).

Natural fiber-reinforced polymer composite materials are rapidly gaining popularity in both fundamental research and practical usage. Composite materials, particularly those reinforced with carbon fiber, exhibit superior strength-to-weight ratios, which make them highly suitable for high-performance automotive applications. Three distinct polymer material combinations were subjected to testing: E-glass/Polyester, Carbon/Polyester, and E-glass/Carbon/Polyester. Mechanical properties were evaluated through hardness and Charpy impact tests.





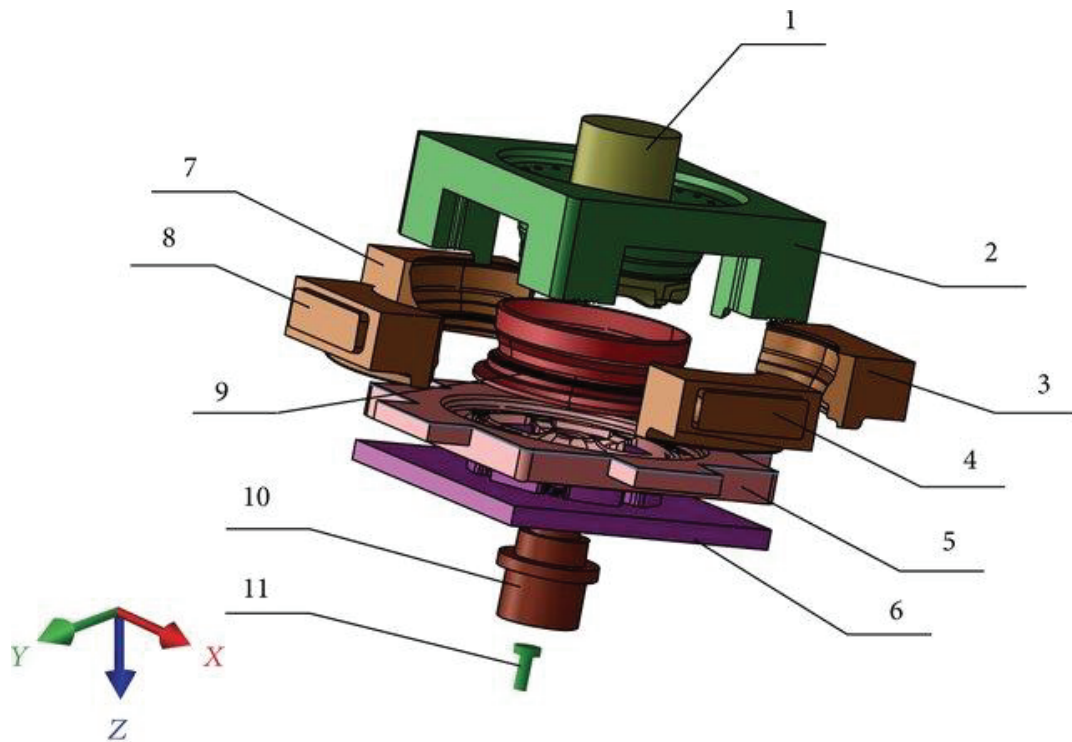
Figure 2.6. Preparation steps of polymer matrix composite wheel (Source: Edwin Raja Dhas et al., 2023)

. Based solely on these results, they could serve as alternatives to metal alloy wheels. In figure 2.5 preparation and coating of outside of the wheel can be observed (Edwin Raja Dhas et al., 2023). Composite wheels are generally designed with an aerodynamic advantage because of the closed surfaces. It's the same effect with aluminum alloy wheels with the plastic cover (Korkut et al., 2019). Through numerical analysis, the authors determined that utilizing a laminated carbon/epoxy composite material wheel instead of steel resulted in a 31.5% reduction in equivalent (Von-Mises) stress and a 15.5% decrease in total deformation. Furthermore, compared to a structural steel wheel, the use of a reinforced carbon epoxy automotive wheel led to an approximate 80% reduction in weight. This reduction in unsprung weight of the vehicle contributes to improved performance (Gardie et al., 2021). Additionally, the significant weight reduction in composite wheels not only enhances vehicle performance but also contributes to fuel efficiency and reduces emissions. The lower unsprung weight allows for better handling and improved ride comfort due to the decreased inertia forces acting on the suspension system.

### 2.3.2. Forged Wheels

This method is widely used and suitable for mass production. Higher investment costs are required, and lower production rates are achieved, with less flexibility regarding geometry. Hybrid processes are additionally employed to reduce costs for example rheocasting, thixocasting, or squeeze casting, all aimed at boosting production rates while simultaneously ensuring a substantial reduction in porosity in castings. In forging, an aluminum bar heated under liquidus temperature is forged into shape. Since this is a semi-solid forging process, the mechanical properties are much better than casting. The wheels, which can also be flow-formed to adjust the shape of the rim surface, then go to machining and take their final shape. Wheels produced in this way are usually heat treated before being subjected to machining processes to further increase their mechanical properties. The most important advantage of the forging process is that it is possible to produce parts with very thin sections and thicknesses without any casting defects related to fluidity and filling in thin sections, which are difficult in cast wheels today. In cast wheels, porosity and shrinkage problems are seen in this case, since a thick section that is fed through a thin section has to be formed. These problems can be overcome with a design change, but you don't always have the flexibility to update the design to be castable (Çetin and Kalkanli, 2009; GURSOY et al., 2021). Forging also produces lightweight wheels that provide optimal strength across all wheel regions, along with the ability to accommodate larger wheel diameters which is another problem today's world among wheel manufacturers.

Despite the favorable forgeability of aluminum alloys in terms of ductility, the energy and force demands vary significantly depending on the chemical composition of the alloy and the forging temperature. The primary reason for the limited use of less forgeable materials in forging operations is the high pressure requirement (Öztürk, 2008). The integrated casting and forging process, an alternative technique, combines the advantages of both casting and forging. This approach enables the achievement of specific properties in different sections of the wheel. In traditional casting, the hub section of the wheel typically displays coarser grain size and inferior mechanical properties due to its thickness and position as the initial solidification region where molten metal enters the mold cavity (Tocci et al., 2015).



- |                  |                              |
|------------------|------------------------------|
| (1) Punch        | (7) Side die                 |
| (2) Top die      | (8) Side die                 |
| (3) Side die     | (9) Wheel hub                |
| (4) Side die     | (10) Discharge and feed gate |
| (5) Bottom die   | (11) Injection piston        |
| (6) Floating die |                              |

Figure 2.7. Die parts of automobile wheel. (Source: Zhang et al., 2015).

However, hybrid methods allow for independent control of the processing region. Illustrated in Figure 2.6 are die components associated with the integrated casting and forging process, identified by numbers. The molten metal enters the mold through the injection piston, after which the punch forges the hub section of the wheel.

### 2.3.3. Steel Wheels

Wheels can be made from either lightweight metal alloy materials or steel. They offer a simpler and more economical alternative to alloy wheels. Forming and welding methods are commonly used in their production, with steel wheels finding greater use in construction machinery and commercially used vehicles. Automotive wheel rims can be classified into single-piece and multi-piece types. However, they are not perfectly axis-

symmetric due to ventilation holes, bolt holes, and valve seats. The rim and disc are produced separately using lamination and stamping processes, respectively, and are then joined through welding. Non-heat-treated low carbon steels typically have low resistance and hardness but high toughness and ductility, making them easily machinable and weldable with low production costs. Sectional welding is preferred over constant welding seams to avoid significant distortion. Overall, the standard steel wheel rim for automobiles is formed by shaping a rectangular sheet metal into a cylindrical sleeve, achieving the desired thickness profile through cylindrical flow spinning, and then forming rims on both sides with an inner cylindrical wall and an outer conical wall. The rim and wheel disc are finally assembled and welded beneath the outer seat of the rim (“Car Steel Wheels,” n.d.).



Figure 2.8. View of a steel wheel (Source: Borecki et al., 2024)

### 2.3.4. Cast Wheels (Low Pressure Die Casting)

The automotive alloy wheel market is expanding as a result of growing demand for lighter and stronger wheels in the automotive sector. Aluminum alloy wheels offer several benefits compared to welded steel wheels, such as greater design flexibility, visual appeal, and weight advantages. Alloy wheels play a role in reducing vehicle weight, improving fuel efficiency, and enhancing performance. Furthermore, they offer superior durability and aesthetics, making them a preferred choice among vehicle owners. The Al alloy wheel manufacturing sector is expected to grow at a compound annual growth rate (CAGR) of 9.63% from 2023 to 2030 (Sejal, 2024). Regarding the low pressure die

casting (LPDC) process, which stands as one of the predominant technologies employed for manufacturing aluminum wheels.

The low pressure die casting machine consists of two main parts: The lower part and the upper part. In the lower section, there's a pressure vessel known as the holding furnace. Here, the liquid metal is maintained at a set temperature using electrical energy. The furnace is lined with refractory bricks and typically features a front cover for transfer purposes. At the rear of the furnace, channels are present through which dried air is supplied via compressors, creating the pressure necessary for the liquid metal to enter the mold. This furnace is mobile and typically moves along a single axis on rails. It contains a riser tube submerged within it and a thermocouple for real-time monitoring of the liquid metal temperature. In the upper part, there is a bottom plate, columns, pistons and cooling channels to which several permanent molds consisting of steel and cast iron parts are connected.

Positioned at the top is the control screen for the machine, allowing for monitoring of all process parameters such as cooling times, flow rates, pressurization parameters, and thermocouple temperature values. The top plate of the bench moves along the z-axis, while the pistons, linked to the side cores, move along a single axis. Furthermore, the outlets of the cooling channels are situated on the upper side for connection to the molds using fasteners and hoses. Even though commercial LPDC machines pressure can be adjusted up to 8 steps and more, typically, the low pressure referred to in this casting method involves a pressure value that comprises three stages, with the pressure slightly exceeding 1 bar in the third stage. The length of the riser tube extends below the metal surface, depending on factors such as style, size, and depth of the casting furnace. This feature provides a notable advantage to the low-pressure process by ensuring that the surface of the molten bath remains undisturbed throughout casting. Consequently, this helps prevent the inclusion of surface oxides into the melt. Mechanical and fatigue properties of low-pressure cast components generally exhibit an improvement of around 5% compared to gravity cast components of the same alloy. By applying pressure in a controlled manner, a seamless and non-turbulent filling of the cavity from bottom to top is achieved. During the initial step, the metal riser is positioned at the end of the tube, with the pressure at its lowest level. The subsequent step involves filling the mold cavity, where the rate of increase in pressure (measured in mbar/s) from the first to the second step is crucial.



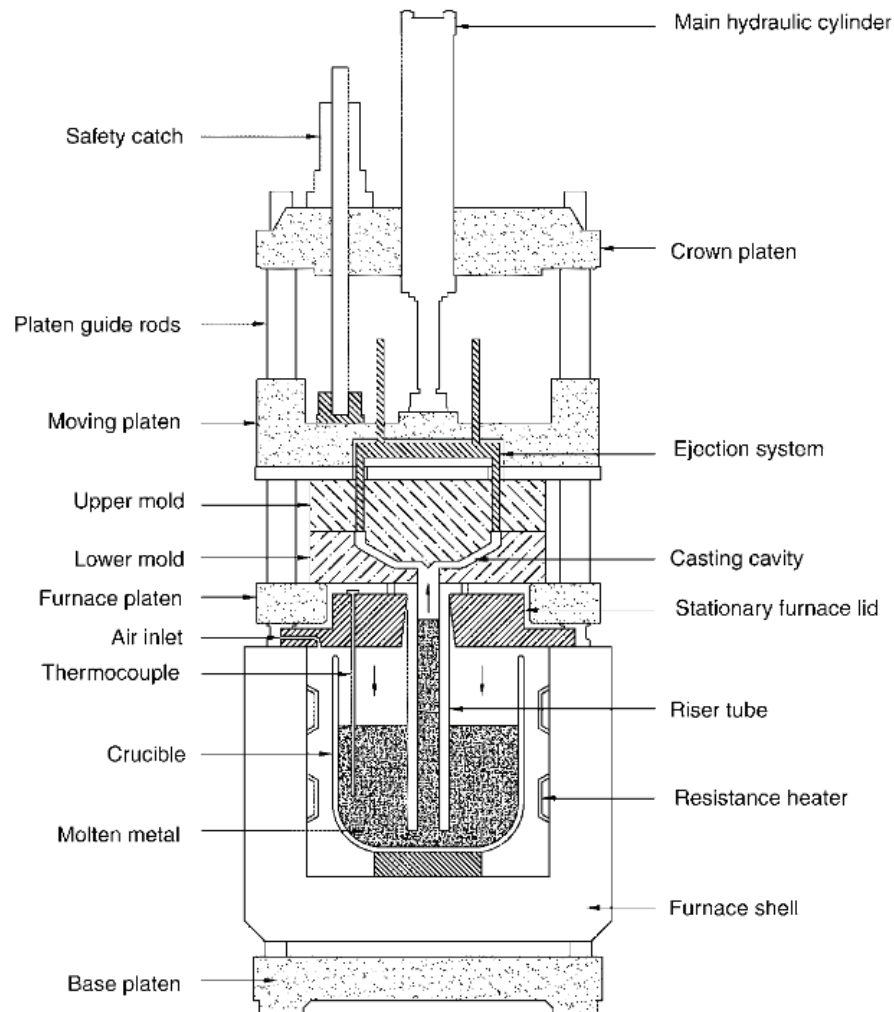


Figure 2.9. Schematic representation of low pressure die casting machine with electric resistance holding furnace (Source: Woycik and Peters, 2008)

It's important to ensure that the metal is filled into the mold without turbulence during this step. The recommended guideline, as stated in the literature, is to fill at speeds below 0.5 m/s (Runyoro and Campbell, 1992). The third stage is where the highest pressure is applied, compressing the metal and maintaining a constant pressure for an extended period. During this time, directional solidification may begin from the inner flange towards the hub as cooling channels come into play. In this casting process, typically consisting of three stages, the pressures and durations in these stages are influenced by factors such as riser tube length, metal density, and mold length along the z-axis.

When setting the parameter, it is also necessary to set the compensation pressure correctly. Compensation pressure is the pressure value entered to compensate for the

decreasing metal level after each part and to pour each part at preset pressure values. Considering that the holding furnaces can carry approximately 1 ton of liquid metal, since the metal level will decrease considerably at the end of 15 pieces, the valves should be commanded to gradually increase the pressure after each piece in order to avoid casting errors such as misrun. Although low pressure die casting is designed to avoid turbulent casting, turbulence must also be avoided in previous operations. As shown in figure 2.9, during the transfer of the metal to the holding furnace, it is important to introduce the liquid metal in the correct time and method (Ou et al., 2020; Kaufman and Rooy, 2004).

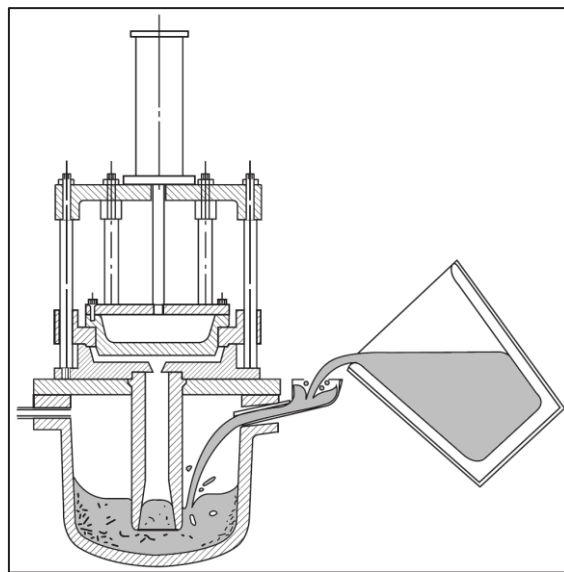


Figure 2.10. Molten metal transferring to the holding furnace

Due to the LPDC method, it is examined with the help of a number of mechanical tests that a wheel is manufactured that is robust and meets customer requirements. Although some of these mechanical tests are wheel-specific and standardized, overall, they are mainly used to measure the basic concepts of fatigue, tensile and yield strength, percent elongation and hardness. The aim of all mechanical tests is to ensure that passenger safety is not compromised. For this reason, the tensile test, which is a destructive testing method, is frequently used in wheel production.

Tensile testing is a widely used type of destructive testing that is one of the easiest ways to understand the mechanical properties of wheels. This test can be repeated even if parameters are changed mid-production to monitor the change in mechanical properties. Depending on the intensity of the labor, results can be obtained after one hour of sample extraction and processing. Customers require specific values to be provided from specific

regions during the commissioning phase and after mass production. The progress of the project and its acceptance for mass production depends on these mechanical properties and other tests.



Figure 2.11. Technical drawing of the location for tensile test bar

The hardness test is another frequently used test. There is a direct correlation between tensile strength value and hardness. After heat treatment, hardness checks are carried out periodically from defined areas of the wheels. Hardness is a critical mechanical property of wheels are checked regularly. In particular, the formation of the  $Mg_2Si$  phase after heat treatment results in significant increases in hardness. Wheels with insufficient hardness are defined as a scrap. Generally, the hardness values expected by customers are above 80 HB.

The Charpy impact test, which is an unusual test in wheel production, is valuable in giving a numerical idea of the impact energy of the samples. The ease of execution makes the test more applicable. Although there are normally impact tests specific to the wheel product, these tests usually give a binary result in the form of an impact load OK-Not OK. This results are given after visual inspection whether any section on the wheel



has crack or not. Due to the primitive nature of this result, the Charpy impact test was used in this study. Under certain conditions, typically ductile metals can fracture suddenly and with minimal plastic deformation. Additionally, standard tensile tests may not provide sufficient depth of analysis regarding the fracture characteristics of a material following an instantaneous impact.

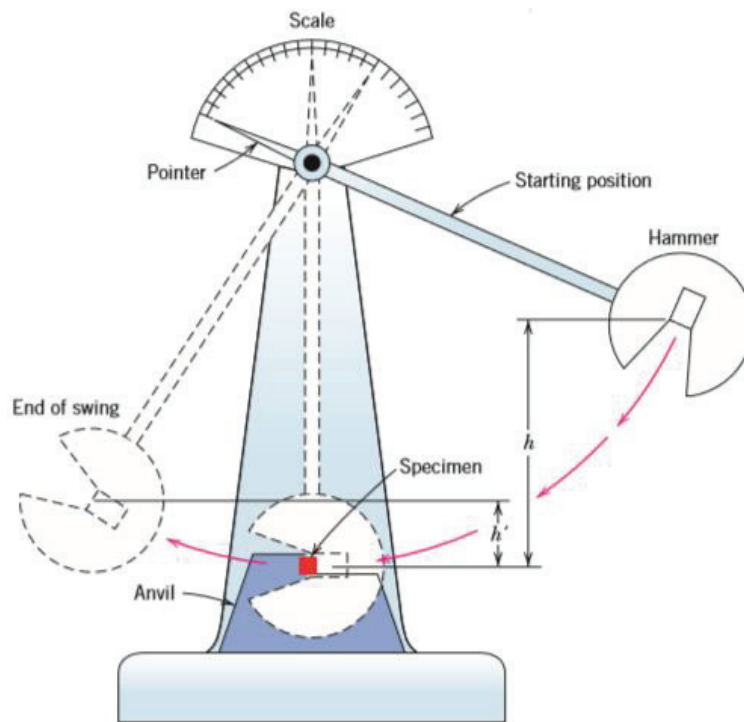


Figure 2.12. Drawing of Charpy impact testing

The Charpy test, originally designed and still widely employed, serves as a common method for measuring impact energy. The specimen typically takes the form of a square cross-section bar, featuring a centrally machined v-notch. The notch in the middle can be U type or in some conditions no notched. Machining procedures adhere to the specifications outlined in ISO 148-1 (“ISO 148-1 2009 Metallic Materials —Charpy Pendulum Impact Test”, 2009).

## 2.4. Heat Treatments

Heat treating refers to the heating and cooling procedures conducted to alter the mechanical properties, metallurgical structure, or residual stress state of a metal product

without aiming to change the physical shape of product. However, when discussing aluminum alloys, the term often specifically refers to operations aimed at enhancing the strength and hardness of precipitation-hardenable wrought and cast alloys heat treated (ASM Handbook, 1991). Aluminum alloys can be divided into non heat treatable and heat treatable. But heat treatment is not only for improving hardness and strength. Annealing is also performed to increase ductility and reduce residual stresses.

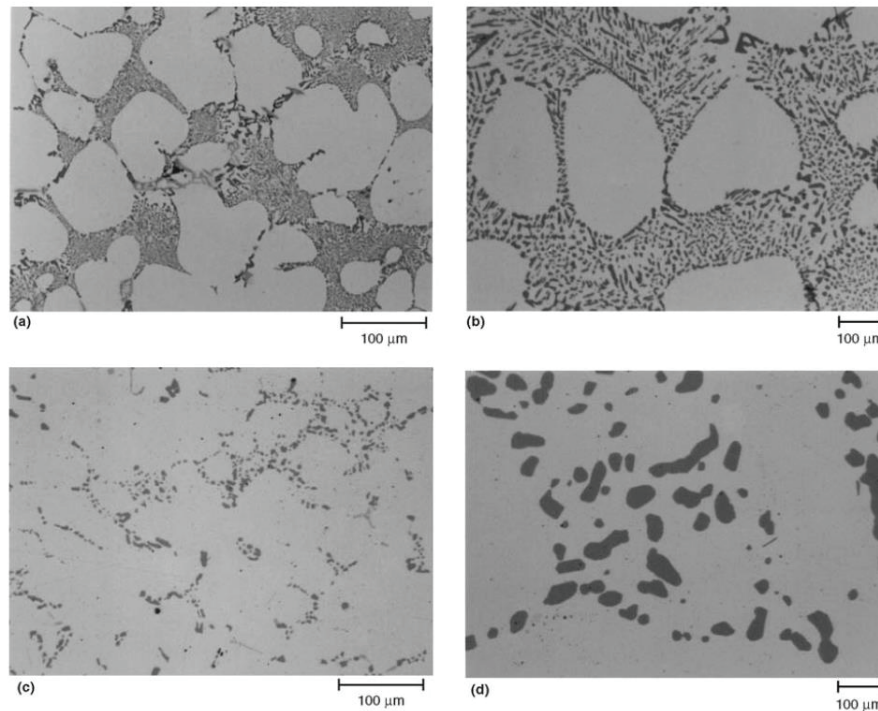


Figure 2.13. Microstructures of A356 alloy light microscope micrographs; etched with 1% HF. (a) As-cast modified, 150x . (b) As-cast modified, 750x. (c) After heat treatment (T6), 150x . (d) After heat treatment (T6), 750x (Source: Warmuzek, 2004)

In the heat treatment, the pace of structural alterations is typically regulated by the speed at which atoms within the lattice shift positions. As a result of heat treatment, the needle-like appearance of eutectic silica structures is replaced by rounded structures. Heat treatments can be described by different letters. T3 (solution heat treated, cold worked, and naturally aged to a substantially stable condition), T4 (solutionized, natural aged), T5 (cooled from an elevated-temperature shaping process and artificially aged), T6 (solution heat treated and artificially aged), T7 (solution heat treated and stabilized), T8 (solutionized, cold worked, artificial aged) and so on. Due to its  $Mg_2Si$  phase content,

A356 is a precipitation hardenable alloy, so a three-step T6 heat treatment is usually applied in wheel production. (Pezda, 2015; Md Yahaya et al., 2020).

### 2.4.1. T6 Heat Treatment

The T6 heat treatment method is widely employed to strengthen age-hardenable aluminum alloys. It involves a series of steps including solution treatment, quenching, and artificial aging as shown in figure 2.11.

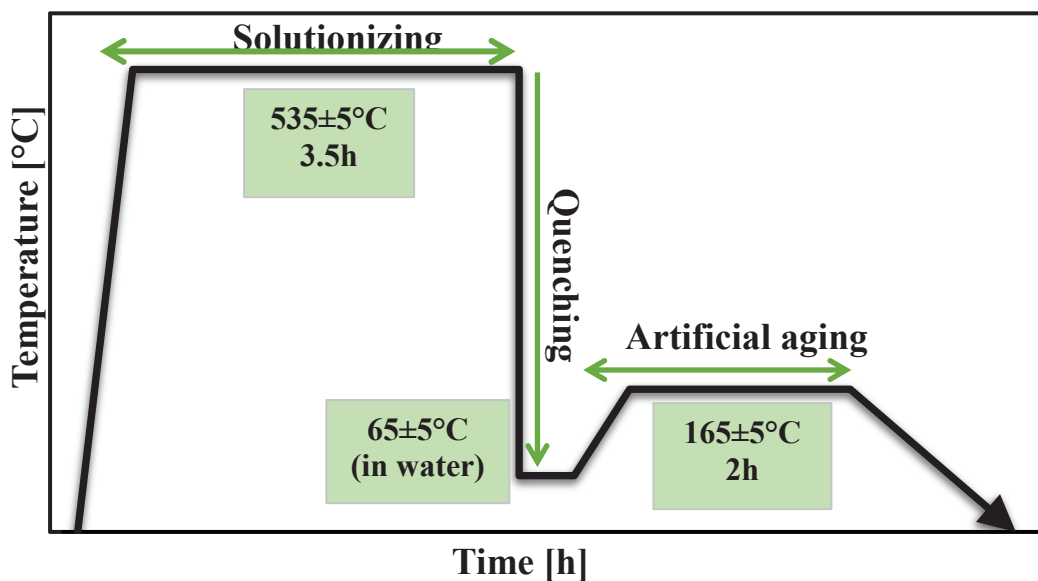


Figure 2.14. T6 heat treatment (Source:A. Y. Kaya et al., 2021)

The initial phase of T6 heat treatment, termed solution heat treatment or solutionizing, holds quite importance in dissolving soluble phases within the A356 alloy. This intricate step involves subjecting the alloy to a meticulously controlled temperature range, allowing the plate-shaped Mg<sub>2</sub>Si particles within the aluminum alloy to dissolve and diffuse uniformly throughout the matrix as a solid solution. The dissolution of magnesium and silicon constituents into the aluminum matrix instigates the formation of GP zones, which serve as precursory sites for the subsequent emergence of Mg<sub>2</sub>Si precipitates. Consequently, the resultant state reveals a supersaturated solid solution, a critical foundation for enhancing the alloy's mechanical properties. Furthermore, alongside its role in modifying the eutectic silicon morphology through alloying with Sr, this treatment facilitates the spheroidization process, further refining the alloy's

microstructure (Güneren, 2019). Solutionizing time and temperature is a subject that has been extensively studied and continues to be optimized according to alloys and conditions. The important issue here is the effect of the time and temperature spent in this phase on the hardness at the end of the aging process. In addition, there are studies that show that secondary dendrite arm spacing also changes with the solution time (do Lee, 2013).

Following the solution heat treatment, the alloy undergoes rapid quenching in a suitable medium, such as water or a polymer solution. This quenching action serves to diminish the solubility of the alloying elements within the aluminum matrix, resulting in the creation of a supersaturated solid solution. During this phase, various observations such as deformations in distinct areas may become apparent. The efficacy of this process is directly influenced by factors such as the type and temperature of the quenching liquid, the duration of immersion, and the entry position of the parts into the liquid. Importantly, quenching plays a pivotal role in averting the formation of large precipitates while promoting the generation of fine, dispersed precipitates essential for the subsequent aging process (Peng et al., 2011).

The quenched alloy undergoes a subsequent stage, called artificial aging, where it is reheated to a moderate temperature and held for a specified duration to enhance its hardness, yield and tensile strength. Both the duration of exposure and the temperature during this aging process are critical. An additional benefit of aging is its capacity to alleviate residual stresses induced during quenching, similar to the stress relief annealing effect. Nonetheless, precise control of time and temperature is crucial to avoid entering a stage known as over aging, which can lead to a decline in hardness. Given that heat treatment is typically employed as a continuous process in industrial settings, optimizing this stage is as crucial as the preceding steps in terms of its impact on material yield, tensile strength, and hardness. It's important to note that prioritizing maximum hardness and strength may necessitate compromising elongation properties (Özaydın et al., 2019; Do Lee, 2018).

## CHAPTER 3

### EXPERIMENTAL

#### 3.1. Materials

Batches containing the specified amounts of Mn were initially prepared in this section. These Mn ratios, given below in table 3.1, were determined based on the customer defined Mn limits. Four batches, each with different amounts of Mn, were created by varying the Mn levels to be both below and above the customer limit.

Table 3.1. Composition of main elements of batches

<b>Batch No.</b>	<b>Mn (wt.%)</b>	<b>Si (wt.%)</b>	<b>Mg (wt.%)</b>	<b>Fe (wt.%)</b>	<b>Ti (wt.%)</b>	<b>Sr (wt.%)</b>	<b>Al (wt.%)</b>
<b>EN AC- AlSi7Mg0.3</b>	Max. 0.050	7.5-6.5	0.20-0.45	Max. 0.15	0.10-0.25	Max. 0.02	Balance
<b>Batch 1</b>	0.040	7.23	0.27	0.11	0.11	0.01	Balance
<b>Batch 2</b>	0.069	7.09	0.27	0.11	0.11	0.01	Balance
<b>Batch 3</b>	0.14	7.23	0.27	0.12	0.11	0.01	Balance

Analyzes are carried out according to EN ISO 10204 3.1. Sampling starts with liquid metal. It is poured into a mold with a diameter of about 35 mm. The solidified sample is removed and grinded on one side. This sample is placed in the spectrometer with the machined surface on top. Spectral analysis is performed on this surface. This is done because cleaned and machined surfaces give the most accurate results. Optical emission spectroscopy can give a percentage distribution of 21 elements. The number of channels can be increased according to the need for additional elemental analysis.

The chemical composition is determined by optical emission spectrometer (OES) can be seen in figure 3.1. ARL ispark 8820.



Figure 3.1. Optical emission spectrometer

For each group, the chemical composition of the sample which was taken from gas fired crucible after adding Mn tablets and grain refiners also being sure to the chemical composition samples were taken after degassing and holding furnace just before casting operation is given in table 3.1. The chemical composition provided indicates the materials derived from the melting furnace and allocated to each group. To minimize measurement errors, the chemical composition is assessed at three distinct points on the surface. To ensure precision in the analysis, three measurements are taken from each prepared sample surface. The values presented in table 3.1 depict the average data derived from three separate analyses conducted on each sample surface.

The manganese tablets (75 wt.%) seen in the figure 3.2 were added into the liquid metal and manually stirred until completely dissolved. Then analysed the chemical composition of liquid metal after stirring.

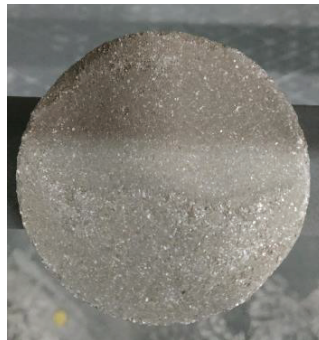


Figure 3.2. 75 wt.% Mn tablet





Figure 3.3. Gas fired crucible

In this study, a gas-fired crucible (figure 3.3) was used for alloying trials. The temperature started to rise by using natural gas. Molten metal temperature was  $730 \pm 10^\circ\text{C}$ . Once melting occurred, an OES sample was taken to analyze the Mn-free chemical composition. After calculations for the aimed Mn composition, Mn tablets were cut, weighed, and then placed into a steel apparatus. Manual mixing was initiated. The process involved waiting until the manganese tablet completely dissolved in the steel apparatus. Once all tablets had dissolved, the liquid metal was transferred to the degassing unit for degassing. Rotary degassing facilitated a more uniform distribution of manganese and other elements within the structure. Following degassing, the crucible underwent another round of sampling for chemical analysis before being transferred to the holding furnace. Chemical analysis was conducted at each stage to precisely determine the alloy's composition and ensure the desired proportions of manganese were achieved, thereby enhancing the trial's accuracy. Subsequently, after closing the holding furnace cover, samples were taken just before the casting process commenced to verify that the cast wheels also met the desired chemical composition.

### 3.2. Wheel Production

In these experiments, production was carried out with the low pressure casting method, which is also widely mentioned in the literature. This method is widely used in the production of aluminum alloy wheels. One of the biggest advantages of the method is that it is possible to produce a wheel in an average of 5 minutes, although it varies greatly depending on the wheel size, alloy type, cooling design and coolant. With this method, directional solidification is performed and the wheel is solidified starting from the inner flange towards the hub. In this way, it is possible to achieve the desired mechanical values in certain areas and reduce the defects that may occur during filling and solidification by managing the correct heat transfers. These heat transfers can be between the mold and the liquid metal, between the liquid metal and the gating system, between the mold and the mold and so on. What needs to be done here is to adjust the correct mold thicknesses and to provide adequate cooling in appropriate places.



Figure 3.4. Molten metal transfer from melting furnace (“Cevher,” n.d.)

Aluminum ingots and scraps are melted in the shaft type melting furnace (StrikoWestofen GmbH), with the proportion of recycled aluminum varying depending on the manufacturing method. For this investigation, a composition of 50% primary



aluminum ingot, 20% aluminum scrap, and 30% machining chips is employed. The first step of this experimental process melting the ingots. Gas fired furnace has a capacity of approximately 700 kg. The metal is transferred from the shaft type melting furnace to the ladle as shown in figure 3.4. The method of carrying the ladle is using forklift. When the metal transferred from the main melting furnace to the crucible the temperature of molten metal is around 720°C. The main melting furnace is set at a high temperature because the cooling of the metal is taken into account, taking into account the waiting times for degassing and transfer, and also to ensure a fast melting under mass production conditions. Thermocouples are installed in different zones of the main melting furnace to control the temperature. One in the bath section, one in the chimney section and one in the section where the metal is taken, which is measured manually with a pyrometer. The temperature in the chimney may give information about the condition of the furnace. It is normal to have a temperature difference between the section where the melting takes place and the section where the metal is taken. In the melting section, the temperature is higher because the burners hit directly. The crucibles are made of alumina based ceramic and are regularly maintained. The maximum service temperature of the refractories used is usually 1200°C. This ladle was then poured into a preheated gas fired crucible. Chemical analysis was then taken before starting alloying. After the first batch of alloying, the metal in the crucible was transferred back to the transfer ladle and taken to the degassing unit for degassing operation. In general, a modifier element such as Sr and grain refiner elements such as Ti and B are added into the liquid metal before degassing. In some production facilities, it is even common to use flux to minimize the loss of aluminum during this degassing stage and to cut the contact of the aluminum surface with the air and to lower the melting point slightly. Neither flux nor grain refiners and modifiers were not used in this study.

In the degassing operation, there is a rotatable graphite impeller as shown in figure 3.5 with holes at the bottom for blowing gas. The crucible must be centered in the degassing unit and the liquid metal level must be constant at all times for accurate degassing performance. After the impeller is immersed in the liquid metal, it starts to blow 99.99% purity nitrogen gas into the metal at the end.

During this operation bubbles should be observed clearly. Because it may be the evidence of better distributed gas bubbles which provides more efficient degassing (Huang et al., 2002).



Figure 3.5. Rotary degassing operation

While blowing continues, the shaft continues to rotate at a certain rpm. Then 50% hydrogen 50% argon mixture is blown for a short time for regassing, after degassing is completed. During these processes, the speed of the rotor was around 300 rpm. It is actually an operation of degassing and re-gassing. It aims to bring hydrogen and inclusions in the molten metal to the surface, hydrogen is released through the surface. Initially, during these trials, 200 seconds of nitrogen was blown at a flow rate of 15 l/min, followed by 3 seconds of mixed hydrogen argon gas, also at a flow rate of 15 l/min which was the regassing stage. It is done for upgassing, that is, to lower the density of the metal in a controlled manner. It is done because it is practical knowledge that castability is increased. The proportions of these values and the combination of gases utilized may vary under mass production conditions. During mass production, the degassing process may involve higher duration of nitrogen blowing, and adjustments in the quantity of mixed gases blown may be made to attain the desired density index values. Additionally, the programs within degassing machine can be modified dynamically to accommodate these variations. This procedure significantly reduces the gas content in the liquid metal. Subsequently, the liquid metal is prepared for casting.



Figure 3.6. After mold coating operation

The low pressure die casting process is done with permanent molds. Therefore, the molds have a preparation process. Before being connected to the machine, the mold parts, whose bottom core is made of Uddeholm dievar, side blocks are made of cast iron, and the upper core is made of H13 steel, are subjected to mold painting after machining. Once the molds reach a temperature of around 250°C through exposure to an open flame, they undergo the application of Dycote 34 and Dycote 39 coatings. Subsequently, after looks like in figure 3.6 the mold is retrieved and closed using a combination of forklifts, cranes, and manual labor. Following the closing process, it is returned to the heating stations for further heating. This time, the mold, heated to a range of 450-550°C, is then transferred to the low-pressure die casting machine and linked up for operation.

It's fair to say that in casting, two crucial steps are filling and solidification. In permanent molds, solidification is achieved using nozzles and cooling channels, as depicted in figure 3.7. Since directional solidification is utilized in wheel production, the nozzle areas and the working time and flow rates during cooling are designed accordingly. The efficiency of cooling is directly impacted by various factors such as the diameter of the air pipes, the area they cover, the number of nozzles utilized, the flow rate passing through them, and the integrity of the pipes with no cracks.

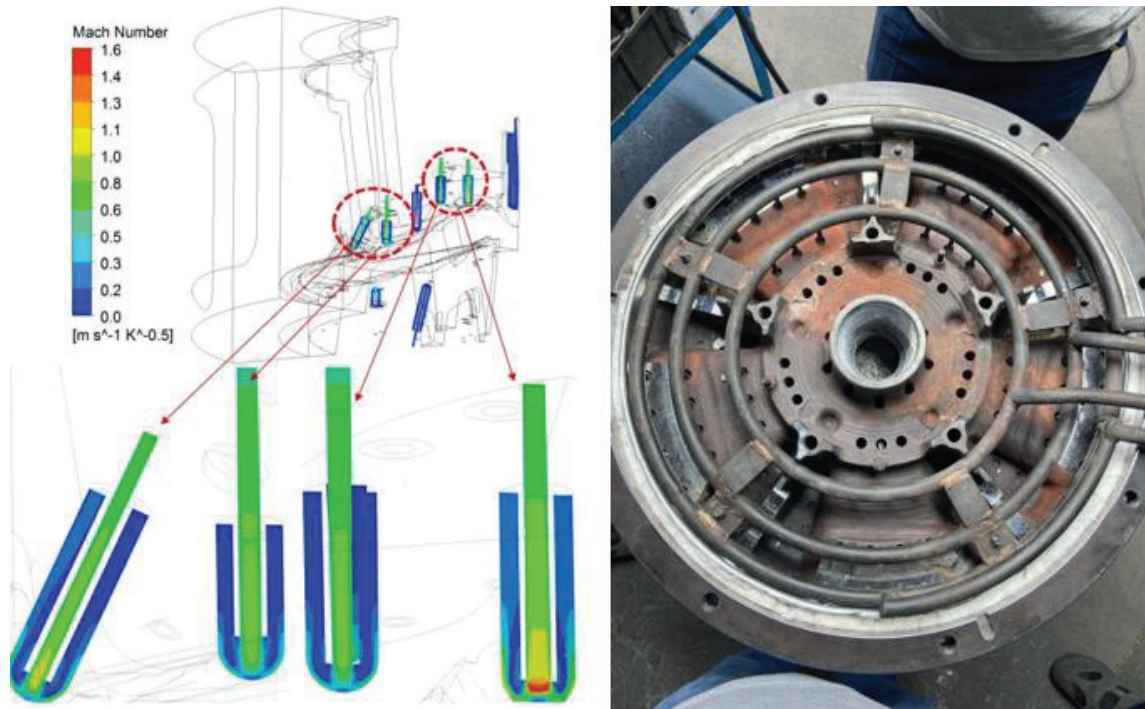


Figure 3.7. Cooling pipes of a die (Kırmızıgöl et al., 2020)

Although the design in the photo is not suitable for water use, there are areas where water is used for cooling. According to the knowledge, the main reason for the use of water is that thicker areas or areas that are required to solidify much faster cannot be cooled sufficiently with air and can instead be brought to lower temperatures in a shorter time with water (Özaydin, Kaya, and Çatal, 2022). In the mold used in this study, only air cooling was used during casting to cool the certain zones of the bottom core, top core and side cores.

Once the mold is placed to the machine as seen in figure 3.8, casting is ready if there is sufficient molten metal in the holding furnace. In mass production conditions, usually before starting production, two castings are made before cooling channels run and therefore castings are made before the full product is shaped. This approach aims to achieve a homogeneous temperature distribution within the mold and ensure a solid product in the final part. This method was employed during the experimental production phase and important for beginning the casting with relatively hot mold, when the mold temperature cannot be monitored locally. It can prevent casting defects that may occur due to increased molten metal flow. However, it is still important that the temperature of the mold can be monitored from at least one point. Otherwise, hot regions will be more likely to crack in stress concentrated areas. In the molds, this temperature is provided by



a thermocouple placed at the spoke end of the lower core and an infrared pyrometer measured manually from the outside.



Figure 3.8. LPDC machine

Once the casting has started and making sure that everything is working properly, cooling and its parameters are the most important issue. During mass production, there are quite limited possibilities to change with waiting time and cooling time. The reason for this is that the molds are given to mass production after the process has been established by the new product launch team. However, in this study, unlike mass production conditions, the process was completely free and casting was done with a different process than mass production conditions. With this process, the wheels passed x-ray without any defects. Then, the same process was applied for all cases in order to avoid any problems due to cooling difference. Following the completion of the casting process, aluminum wheels are removed from the machine and visually inspected by an operator. At this stage, the rim is checked for misrun, intense cold shots, cracks and deformations. Then, x-ray inspection is conducted to identify any porosities, shrinkages, or other defects present in the casting.

Xray is a mandatory quality inspection for all wheels, whether mass production or trial. Wheels that do not meet the criteria here are directly marked as scrap and separated. Xray inspect at the hub, spokes, rim, and offset of the wheel from certain viewing angles according to the ASTM E 155: Standard reference radiographs for inspection of aluminium and magnesium casting. A distinction is made according to the distance and size of the existing porosities from each other. If they are above a certain size and number, the wheel is separated into waste. The same applies to the shrinkage error. If there is also an error caused by the wire filter used in the hub, it can also be considered as waste. Small cracks may not be visible on xray. A liquid penetrant test is essential for this. In the trial production, all wheels passed the xray inspection intact.

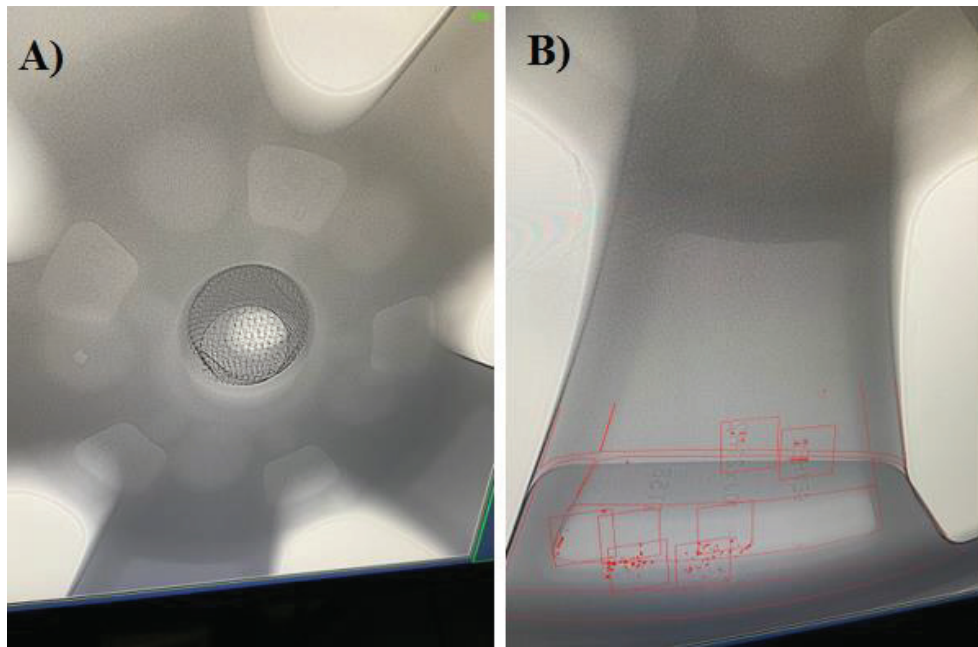


Figure 3.9. Xray inspection A) hub B) spoke part of wheel

### 3.3. Mechanical Characterization

As mentioned earlier, Fe intermetallics have a negative effect on the fracture properties of the wheel. In order to better understand and quantify this property, wheels were subjected to various mechanical characterization processes. Tensile tests were performed to see the differences between elongation and yield, tensile strength, Charpy impact test to see the fracture energy change and hardness measurements to see the changes in hardness.

### 3.3.1. Tensile Testing

The samples underwent processing according to DIN 50125 standards. The specimens undergo machining with a horizontal CNC turning machine to achieve the desired dimensions. (“Testing Of Metallic Materials – Tensile Test Pieces, Prüfung Metallischer Werkstoffe – Zugproben Deutsche Norm DIN50125”, 2016).

After cutting from the certain region of wheel for tensile test according to technical drawing can be observed in figure 3.10, tests were carried out at least 3 times for each region by using Zwick Z100 model test machine according to PN-EN ISO 6892-1: 2020-05 (“Metallic Materials - Tensile Testing - Part 1: Method Of Test at Room Temperature, PN-EN ISO 6892-1: 2020-05”, 2020). Preload is set 50 N and test velocity of tests is 0.002 1/s.

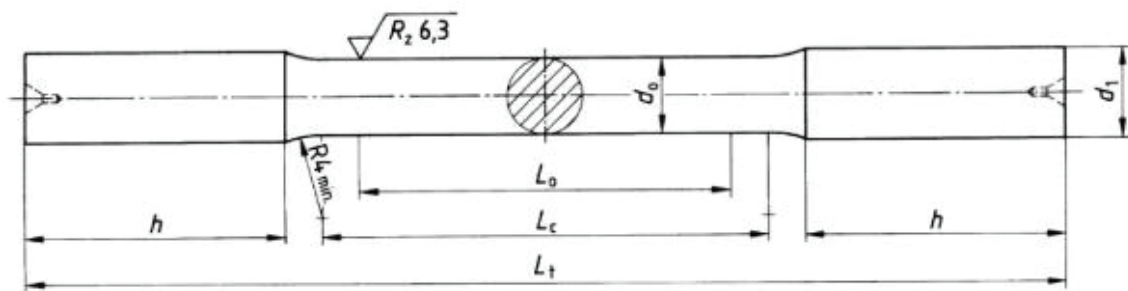


Figure 3.10. Tensile test bar in DIN 50125

In these trials, two wheels from each batch were subjected to tensile tests after heat treatment and as-cast condition. The bar was removed from the relevant areas. Approximately 5 tensile bars were removed from each area of a wheel in a batch, and four different zones were examined per wheel. Excluding the reference specimens, a total of 160 tensile tests were performed. The non-heat-treated bars removed to understand the progress of the trial production will not be shared to avoid data redundancy. For this reason, the averages of 120 tensile test results will be shared and discussed in the results section.

### 3.3.2. Hardness Test

Brinell hardness tests are conducted in accordance with EN ISO 6506 and ASTM E 10 standard. Prior to conducting the hardness test, it's essential to grind and polish the

surfaces of critical regions designated for testing. Following the polishing process, the cross section of wheels were prepared for the Brinell hardness test. Cross-sections are taken from the wheels and the hardness of the critical 11 different zones is examined. In this study, In order to see accurate results, the hardness of the critical areas of the cross sections taken from three different wheels belonging to the same batch, i.e. 12 different wheels in total, were examined by the machine Qness q250 Cs.

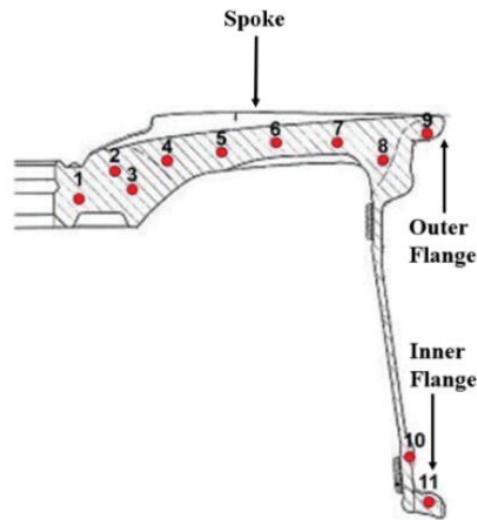


Figure 3.11. Points on a cross section of a wheel for hardness test (Kutsal et al., 2023)

The regions shown in figure 3.12 have different thicknesses and cooling parameters. It may therefore only make sense to compare the same number for a different wheel. For example, the region where solidification starts first is region 11th. It would not be surprising that the hardness here is higher than in region 2nd, which is a thicker and later solidifying zone. However, as mentioned before, after heat treatment, a hardness value above 80 HB should be observed in each of them. Hardness values are displayed directly on the digital display. The logic behind the calculation is the formula used in equation 3.1.

$$HB = 0.102 \frac{2F}{\pi D (D - \sqrt{D^2 - d^2})} \quad (3.1)$$



### 3.3.3. Charpy-Impact Test

The principle underlying the Charpy impact test relies on the concepts of potential energy and gravity. The sample is positioned centrally within the notch, and the hammer strikes the back of the notch. The hammer is initially held in a cocked position and then released from a consistent height. It falls freely, causing the specimen to fracture at the notch. Eventually, a numerical value in joules is displayed on the screen, representing the impact energy. This energy is calculated as the difference between the pendulum's initial position and its highest point following the fracture of the sample.



Figure 3.12. Red coloured Charpy specimen region on a wheel

These tests give binary like OK and not OK results under certain loads. In order to observe the effect of manganese addition more clearly, charpy samples were removed from the cosmetic surface of the wheel where industrial impact tests were performed. Since the specimen dimensions were 55 mm and the length and width were 10 mm, and since this is the area where the hammers of the other industrial impact tests hit, the specimen was removed from the area marked in red. A total of 18 specimens were removed from three different areas for each wheel with the same logic, 6 specimens from each batch, for a total of 18 specimens, such as the area marked in red in Figure 3.14. The

notched parts were created to coincide with the back side of the wheel. The reason for this is that in real life, the impacts on the wheel usually come from the front surface (such as hitting the curb, crushing with a car). Charpy impact tests were carried out v notched specimens by using the CEAST Resil Impactor having maximum hammer energy of 15 J.



Figure 3.13. Ceast Charpy impact test machine

### 3.4. Microscopic Characterization

Wheel production flow chart mentioned in detail in the previous chapter, the cast wheel first goes to xray control. If there is no casting defect such as porosity, shrinkage, etc. that meets the criteria, it is sent directly to the heat treatment furnaces, which is a continuous system, for T6 heat treatment. After heat treatment, waiting for the wheel to cool to room temperature, then it is sent to the laboratory.

In this study, T6 heat treated wheels were given to the laboratory. A number of cutting, grinding, and polishing processes were applied to 2 wheels from each batch for microstructural analyse. Since the wheel was too large for laboratory scale work, they

were first cut out on the band saw from the areas where the microstructure was to be examined. In order to see all of these regions properly, a cross-section was taken from half of the wheel, as was done during the new product launching phase. Since this cross-section would still be large, it was cut into pieces as shown in figure 3.16.

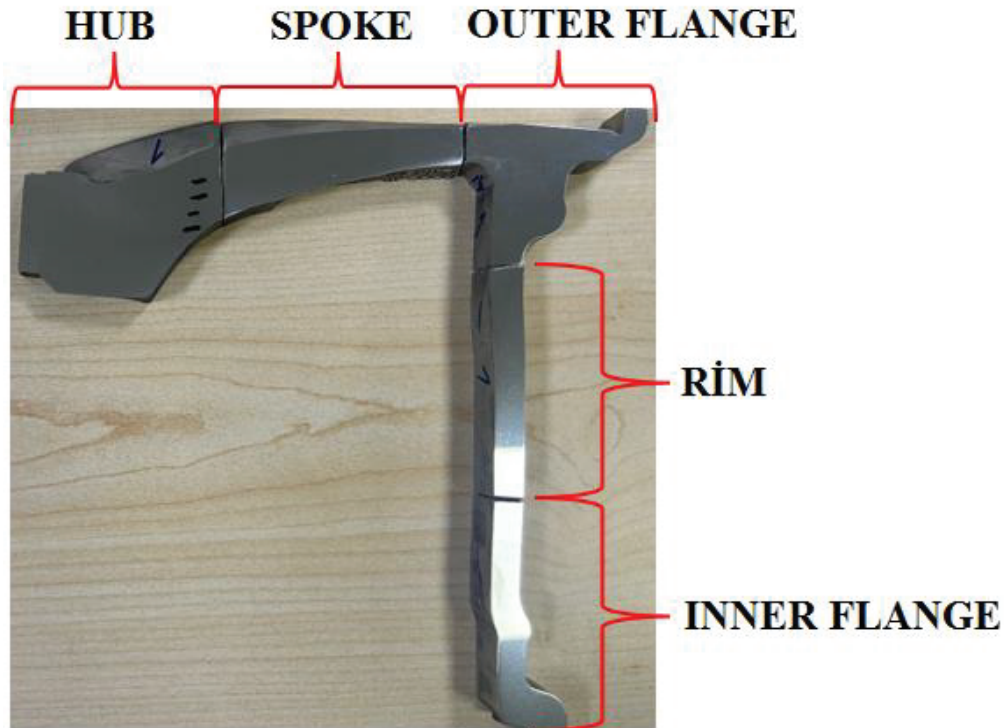


Figure 3.14. Wheel sections for microstructural analyse

On the other hand, after Charpy impact test, for deeper understanding the type of fracture and analysing the causes lying behind differences impact energies among specimens, they were prepared to examine the fracture surfaces to be observed by scanning electron microscopy. In total, 6 samples from each batch and a total of 18 Charpy impact tests were performed. However, since examining the surfaces of all specimens would lead to data pollution, the fracture surfaces of 5 specimens were examined from each batch, including the specimen closest to the average impact energy value and the specimens with the highest and lowest impact energy. The scanning electron microscopy (SEM) analysis revealed distinct fracture morphologies corresponding to the different impact energy values. Specimens with higher impact energies typically exhibited ductile fracture characteristics.

### 3.4.1. Optical Microscopy

First of all, the specimens need to be flattened. It is not possible to look at an unflattened specimen with an optical microscope because the depth of field is too low in an optical microscope. Such a specimen will have a clear image on one region and a blurred image on the other. This image may not provide proper information about the microstructure of specimen. For this purpose, surface preparation is started by passing the samples through abrasives ranging from 180 to 2500 ppi silicon carbide papers by using the machine Struers Tegramin. The sample is rotated 90 degrees before each grinding.

Heating is prevented by using water during grinding. The sample is cleaned with alcohol after grinding and immediately dried with compressed air to determine whether the sample has been grinded properly. Diamond pastes are categorized based on the dimensions of the particles they contain. Polishing with 1 micron diamond paste is performed. It is a water-free application. Following these procedures, the specimens undergo etching in a 0.5% HF contained etching solution. The polished surface is treated with the etching solution for approximately 15 seconds. Finally, the surface exhibits a reflective appearance like a mirror, indicative of the completion of the preparation process. This mirror-like image indicates that the sample is ready to be examined under the microscope.

As can be seen in figure 3.17, play dough was used as a support to ensure complete flatness during the optical examination of the pieces that were cut out of large pieces like wheel and could not be completely flattened. Because the surfaces of these specimens contacting the ground must be flattened as well as the upper surfaces. The time and labour required for specimens are decreased by using dough. The microstructural examination of samples was conducted using a Nikon LV150N optical microscope and analyzed with Clemex image analysis software. Using an optical microscope, examinations were performed at 100x and 200x magnifications. Previously, samples were prepared by dividing the wheel into hub, spoke, outer flange, rim and inner flange. Subsequent examinations showed that there were no visible differences between some regions. In these microstructural examinations, particular attention was given to identifying any inconsistencies or defects within the material. Regions of interest included the grain structure, presence of inclusions, and potential microcracks, as these factors significantly influence the mechanical properties and overall performance of the wheel component.

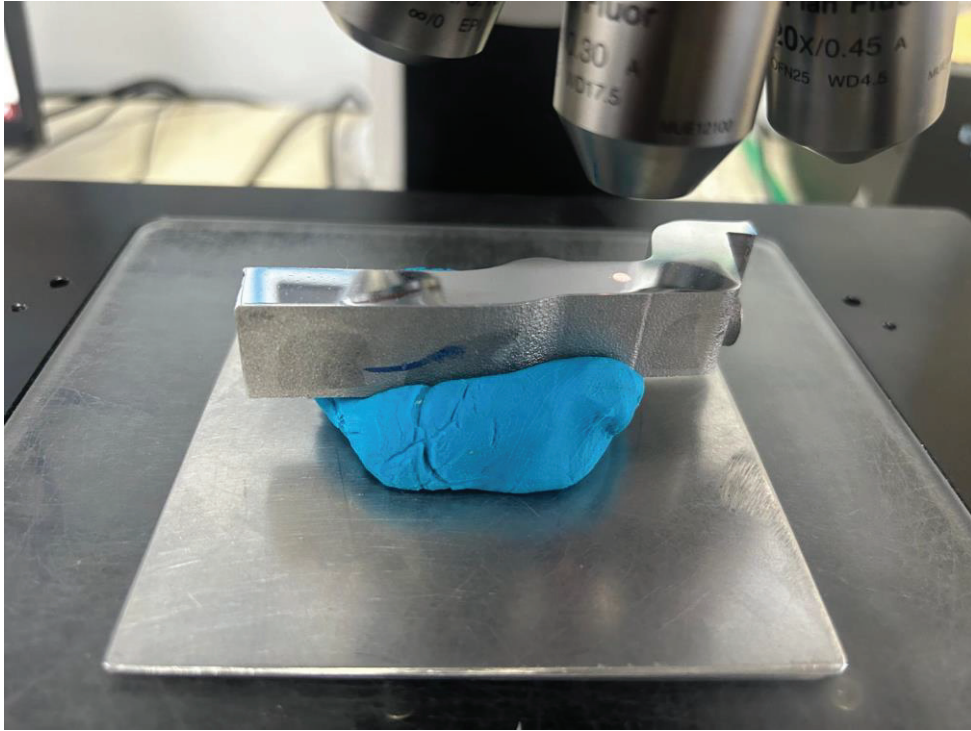


Figure 3.15. A sample of the optical microscopy

Therefore, these examinations were basically made from 3 different wheel regions. These were spoke, hub, and rim. In these images, the distribution of grain size, modification in eutectic silica, the distribution of different phases, aspect ratio and porosity-like casting defects were observed. In images recorded with the help of a microscope, the scale bar can be selected according to the closeness of the lens and specimen then the image can be saved with suitable scale bar. In addition, in order to verify the visual analysis with numerical data, various visualizations were made with the help of ImageJ software. After these visualizations, the numerical data were processed and converted into histograms. Another parameter that was analyzed using an optical microscope was the dimensions of the SDAS.

Measurements can be made at all magnifications, but these measurements were made at 25x magnification, looking at the sample from a distance to see a more general distribution. Critical regions were previously identified in figure 3.16 but SDAS was measured from these critical 3 regions as mentioned earlier. Using the linear interception method, the SDAS is determined by dividing the length of a dendrite arm by the number of arms. The procedure for measuring SDAS involved specifically selecting dendrites with at least five arms and performing the measurement exclusively on these dendrites (Özaydın, 2015). However, in this study, 3 primary dendrites with more than 5 branches



were selected and measurements were taken accordingly. The length of these dendrites was then divided by the number of arms to obtain a number. Finally, 3 numbers were obtained from each region and the average of these numbers was taken as the SDAS length of the region.

In addition to SDAS measurements, microstructures examined at 100x and 200x magnifications provide important information about the different zones of samples and their condition. With these photographs, circularity, aspect ratio, minor, and major axis histograms were drawn with the help of ImageJ software. These were plotted in two separate graphs as number fraction and area fraction.

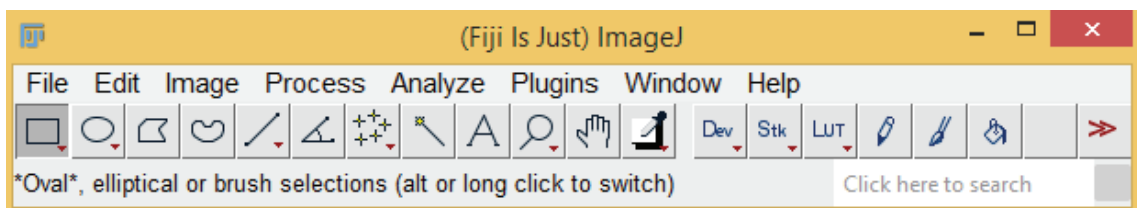


Figure 3.16. Menu of ImageJ

The optical micrographs taken here is first dragged and dropped by opening the ImageJ software. After opening the program, the menu in figure 3.19 appears. Select a rectangular shape and crop all sections of the image except the scale bar. If you think that the photo is not sufficient enough, utilize the subtract background option which is a subheading of the processing tab in the menu. To ensure that uniform lighting across the image. This process is not always mandatory but this step contributes to a smoother appearance of the photos. The important thing here is to make the color tones (shades of gray) so that as many different phases as possible are perceived before converting the image into digital data. For example, if the sample exhibits numerous scratches resulting from the grinding process and if it is not removed them with photo processing, these scratches can be perceived as other eutectic Si particles because they are black in color and can potentially leading to significant calculation errors. Once decided that the photo is suitable enough for processing, it can be changed to an 8-bit version, so that it is completely in shades of gray. Then select adjust from the menu, which is a sub-heading of the image option. Click on the threshold option, which is also a sub-heading. Threshold is the option where the relevant image painted. It can be guesswork from the name, here which phases and particles will be painted in which color can choose. If certain values

exceed, it might be the reason for places that are not actually eutectic Si to be counted as if they are. For instance, mistakenly classifying gas porosities and micro porosities that are obviously not Si as Si simply because of the exceeded threshold by a significant margin, but if it would be too low for certain values, it may be ended up not being able to mark all eutectic Si. The ideal way to avoid both of these issues is to experiment between values, checking where in the image they are marked.

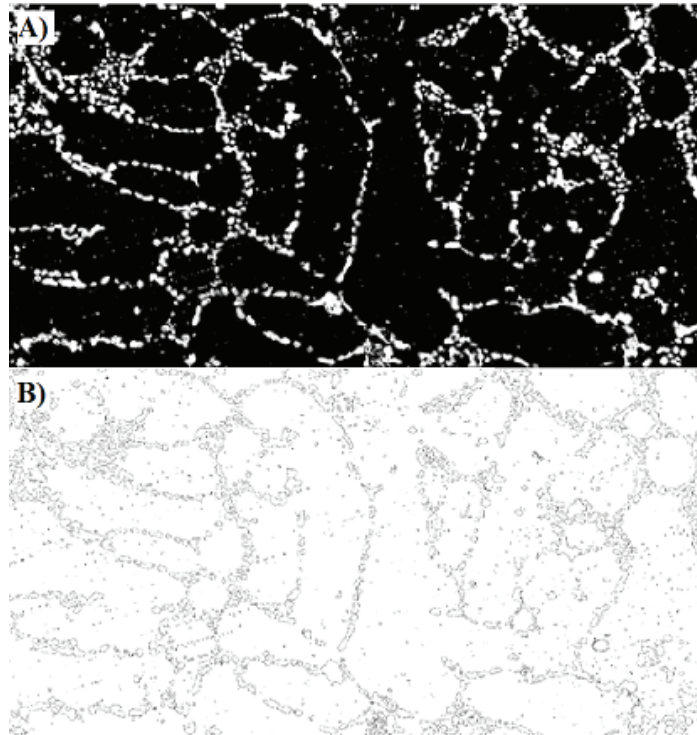
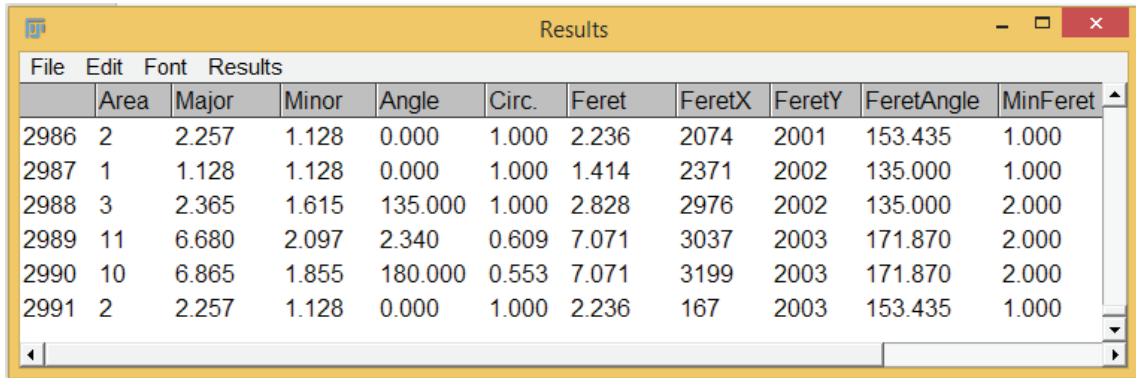


Figure 3.17. Created images at 100x magnification A) after threshold B) after particle analyse

Once ensured that the threshold option is properly configured, a black and white image is generated, as shown in Figure 3.20 A. Automated particle counting is feasible provided that the image does not contain an excessive number of individual particles that are in contact with each other. In this image, light-colored areas appear close to black tones, while dark-colored areas appear close to white tones. Assuming all silicon particles to be analyzed are accurately colored, the next step is particle analysis. The primary aim of generating object shapes is to analyse their morphology. Detectors that detect object contours automatically initiate the calculation of morphological characteristics. When applicable, these characteristics are calculated using the physical calibration and units of the source image. For instance, if image is calibrated with a pixel size in micrometers, the

area of objects will be expressed in square micrometers. During this stage, data generation is finalized after checking a few options based on the specific circumstances, such as excluding particles at the image edges. The software evaluates the particles as ellipses and generates corresponding data. Once it has figured out the correct threshold value and particle size range for your objects of interest, it can be automated particle analysis using macros.



	Area	Major	Minor	Angle	Circ.	Feret	FeretX	FeretY	FeretAngle	MinFeret
2986	2	2.257	1.128	0.000	1.000	2.236	2074	2001	153.435	1.000
2987	1	1.128	1.128	0.000	1.000	1.414	2371	2002	135.000	1.000
2988	3	2.365	1.615	135.000	1.000	2.828	2976	2002	135.000	2.000
2989	11	6.680	2.097	2.340	0.609	7.071	3037	2003	171.870	2.000
2990	10	6.865	1.855	180.000	0.553	7.071	3199	2003	171.870	2.000
2991	2	2.257	1.128	0.000	1.000	2.236	167	2003	153.435	1.000

Figure 3.18. Results window of a processed image

Eventually, some data is created by the software after bunch of image processing steps. Here are some captions about particles given in figure 3.21. The assessments are done by assuming these particles as an ellipse. Therefore, minor axis which is the y axis, major axis which is the x axis when thinking the coordinate system. Feret diameter is measure of an object's size along a specified direction. Feret x and feret y describes the starting coordinates of ferets. The longest distance between any two points along the selection boundary, is determined using the Feret. The angle of the Feret's diameter, which ranges from 0 to 180 degrees, is presented as the FeretAngle. We obtain the final histograms as a result of processing the data in these headings. Here we encounter two more critical concepts that will be discussed in the results section. They are circularity and aspect ratio.

$$\text{Circularity} = 4\pi \times \frac{\text{Area}}{(\text{Perimeter})^2} \quad (3.2)$$

$$\text{Aspect Ratio} = \frac{\text{Major Axis}}{\text{Minor Axis}} \quad (3.3)$$



According to the equation 3.2 circularity must be maximum a value of 1.0 that signifies a perfect circle, while approaching 0.0 suggests a progressively elongated shape. However, these values might not be reliable for very small particles. Whereas the aspect ratio tells whether there is elongation towards the major axis or the minor axis.

### **3.4.2. Scanning Electron Microscopy**

Electron microscopy was used to analyze the fracture surfaces and to understand the phases formed on the surfaces by EDX analysis. Efforts were undertaken to capture the brittle or ductile fracture of the surfaces, alongside the shrinkage and oxides resulting from casting. Since the fractured surface is analyzed, the sample surface is full of indentations and protrusions. For this reason, the depth of field, which is very low in optical microscopy, was examined in electron microscopy due to the need for a technique that can analyze well and take closer images. Surface preparation methods (polishing, grinding) steps could not be applied as in optical microscopy because of the topology of fracture surface. However, in order to examine these images accurately, like the optical microscope, the fracture surfaces must be cleaned of any dirt that may come to the surface during the test. For this reason, each fracture surface that was decided to be examined was placed in a beaker. The sample was filled with ethanol until it was completely submerged. Then, the mouth of the beaker was covered with parafilm and aluminum foil. It was placed in the ultrasonic washer as shown in figure 3.22 and waited for 5 hours. The ethanol of the samples taken out of the beaker was filtered and dried in the oven at 60 °C for 1 hour.

Dried samples were placed in the ZEISS Evo 10 scanning electron microscopy (SEM) device for examination. A total of 5 samples were examined. These were the sample closest to the average from each batch, and the samples with the maximum impact energy and the minimum impact energy among all samples. Initially, an examination was made with the help of a secondary electron detector to understand the surface topology, see the broken grains and whether there were brittle or ductile fractures or examples of both. Then, for each batches, photographs were taken at a magnification of at least 50x and at most 5000x. The findings from the SEM and EDS analyses were integrated with the results from the Charpy impact tests and optical microscopy to build a comprehensive understanding of the material behavior.



Figure 3.19. Ultrasonic cleaning of SEM samples

To understand the effect of manganese addition and to have a deeper knowledge about the composition of certain areas on fracture surfaces, elemental distribution was examined in determined areas and points with the help of a backscattered detector. With the assistance of the backscattered detector, various interpretations can be derived, given that heavier elements appear brighter than the gray tones in the area. Instead of providing topographical data, this detector reveals elemental distinctions that may arise in critical regions. A more thorough analysis was conducted using the EDX detector, which displays the elemental distribution of marked regions as points, areas, or lines. Due to their small atomic weight, elements like carbon and smaller in the periodic table cannot be detected. Moreover, the percentage elemental distribution in the marked area can be determined using this detector. In this study, elemental distribution information was obtained by conducting EDX analysis on critical areas on the fracture surfaces of these 5 samples.

### **3.5. Casting Simulation**

In the previous chapters, it was explained that wheels are produced by the LPDC method, in which the cooling rate, alloy chemical composition and casting defects highlighting a direct influence on the mechanical properties of the wheel. It was said that the LPDC method is generally preferred in wheel production because it is a profitable method when large number of pieces are required. In parallel with these, the parameters

and designs of the cooling, the designs and thicknesses of the molds, the pressurization and molten metal temperature parameters of the casting are the parameters that have a significant effect on the mechanical properties of the product, the shape and size of the phases in the microstructure, since they are deeply influential on solidification and feeding, even if the composition does not change during the process. Developing and experimenting with these parameters and determining the most accurate one would require a great deal of time and cost if attempted in real life. For example, it takes hours to send a mold to the relevant mold repair team for modification, and even just thinning certain areas of the bottom core. This is due to the intensity of the work at the time, the time it takes to mount the mold to the workbench, and the time it takes to machine it, making it a time-consuming operation. Once the mold is tested with new parameters, it undergoes internal approval tests again due to its role as a safety component. Its integration into mass production requires a process and tracking mechanism that takes days. If the labor and alternative costs spent during this period are taken into account, it is obvious that it is not a budget-friendly method. For exactly these reasons (time and costs), software that performs computer-aided calculations has been developed. MagmaSoft commercial casting software, which is frequently used in the casting industry, especially in high pressure die casting, and is also the most helpful program in wheel manufacturing by low pressure die casting, was also used within the scope of this study. MagmaSoft has not been only just a theoretical model, but also becoming a practical tool that aids foundries by continuously gathering data from its customers and integrating real field parameters into the program. (Fan et al., 2018; Guofa et al., 2009; Reilly et al., 2013).

The first menu that appears when you open MagmaSoft 6.0 is shown in figure 3.23. Here you need to select the project you are working on from the project section. In order to start a new project, you can also set up a new project from this section. In the geometry section, the main geometric data is defined to Magma. Generally, the parts drawn in commercial drawing softwares such as CATIA V5 are introduced to Magma in .stp format under this subsection.

A definition is assigned to each part to make it meaningful for casting. Because the program cannot know which casting element is drawn and for what purpose. For example, you need to introduce the program that the geometry is a cooling channel.

Besides, this is the section where the drawn runner, feeder and coolers are introduced.



Figure 3.20. Startup menu

Here, the input of the molten metal should also be introduced to the program, however additions can be made with the help of additional drawings with the help of a simple interface.

The entire mold looks like the one shown in Figure 3.24. Each component of the casting layout is converted into a separate .stp file and then introduced to Magma individually.

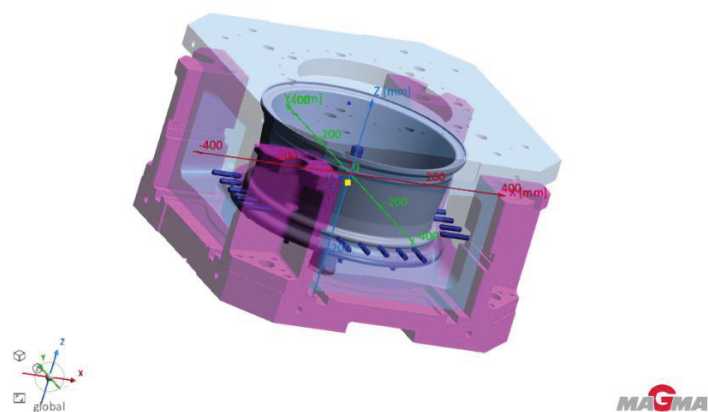


Figure 3.21. .CAD data of the mold, wheel, and casting system

This approach allows for distinct assignments to be made for each tool, as it's not possible to make different definitions on a single part. The area coloured in purple in the figure represents the machine bedding part. While this section may not be particularly crucial in terms of casting, defining it separately enables the selection of different material types and heat transfer coefficients for further modelling sections. By incorporating such detailed information into the software, the inconsistency between simulation and real-life casting is reduced.



Figure 3.22. Mesh quality

After the geometry operations are completed, the meshing process is started. Meshing is the determination of the smallest unit selected in the software where mathematical formulas work and the weaving of the material with this unit. This refers to the process of getting closer to reality by creating the smallest possible network structure that outlines the workpiece. In specific areas, we can adjust the mesh to be either more detailed or more simplified as needed. As shown in figure 3.25, this mesh structure can be checked under the heading mesh quality. For this study, it should be noted that the areas indicated as in contact with air may or may not be genuinely connected to the air. Where edge-edge is shown highlighted with yellow, the problem can be solved by thinning the mesh a little more.

Material definition is one of the most important subheading of the program. As can be seen in figure 3.26, almost all important information about the casting is defined here. Casting temperature, alloy composition, material type of mold parts, initial temperatures, heat transfer coefficients between casting elements including refractory materials, casting time, pressurization are just a few of them. Of course, it is not always

possible to define this stage one hundred percent accurately, as how realistic you can build your model depends on how accurately you can actually measure it at the manufacturing field. In this study, the Mn composition was changed and run.

Material	Mat ID	Database/File name	Initial Temperature (°C)	Aluminum Composition
Cast Alloy		User/AlSi7Mg-JMATPro	710.0	Cr (Chromium) 0.0025 %
				Cu (Copper) 0.0019 %
				Fe (Iron) 0.0893 %
				H (Hydrogen) 0.3 ml/100g
				Mg (Magnesium) 0.263 %
				Mn (Manganese) 0.04 %
				Na (Sodium) 0.0 %
				Ni (Nickel) 0.005 %
				P (Phosphorus) 0.0 %
				Sb (Antimony) 0.0 %
				Si (Silicon) 7.324 %
			Sr (Strontium) 0.0194 %	
			Ti (Titanium) 0.09 %	
			Zn (Zinc) 0.0042 %	
Material	Mat ID	Database/File name	Initial Temperature (°C)	
> Filter		User/Sieve_0.55		
Material	Mat ID	Database/File name	Initial Temperature (°C)	
Permanent Mold				
Bottom Core	ALTMACA	MAGMA/X40CrMoV5_1	450.0	
Bottom Core	SERAMIKYOLLUK	MAGMA/Al2O3	400.0	
Bottom Core	MADENIYOLLUK	MAGMA/GIL-250	450.0	
Bottom Core	DIKME1	MAGMA/GIL-250	300.0	
Machine Bedding	ALTPLAKA	MAGMA/STEEL	300.0	
Side Core	YANBLOK1	MAGMA/GIL-250	350.0	
Side Core	YANBLOK2	MAGMA/GIL-250	350.0	
Side Core	YANBLOK3	MAGMA/GIL-250	350.0	
Side Core	YANBLOK4	MAGMA/GIL-250	350.0	
Top Core	USTPLAKA	MAGMA/X38CrMoV5_1	350.0	
Top Core	USTMACA	MAGMA/STEEL	450.0	

Figure 3.23. Material definitions



## CHAPTER 4

### RESULTS AND DISCUSSION

In this chapter, the mechanical properties and micro analysis data obtained from the wheels as a result of trial casting will be shared and their results will be evaluated.

#### 4.1. Mechanical Characterization Results

In this section, HB hardness results, tensile test results, and impact test results will be shared respectively.

In the screen of Qness q250 Cs test machine Brinell hardness results are seen. Screen provides magnified views of both the samples' surfaces and the indenter's marks. Measured points were shared previously in figure 3.12. Tests were carried out with EN ISO 6506 and ASTM E 10 standard. In this study, cross-sectional hardness measurements were taken from the defined areas of the wheels from three wheels from each of the reference samples (without added manganese), batch 1, batch 2, batch 3. In the table 4.1, each of these data is shared and then the averages for all three wheels are given with the abbreviation AVR. Standard deviations of hardness values are given with the abbreviation STD and error bars are plotted according to standard deviations. Since the wheel product is directionally solidified, it is so normal to have different hardness values at the 11 points given. In addition, the thickness and geometry of the wheel varies regionally. Also, areas close to the cooling nozzles will also cool rapidly and show high hardness values. Depending on the cooling direction, it was observed that the hardness increased towards the rim surface as expected. Reference specimens (specimens without manganese addition), showed relatively higher hardness than those with manganese addition.

In this section, hardness, tensile strength, yield strength, percent elongation, impact energy and optical microscope and scanning electron microscope images are given, respectively. In here, which is also enriched with SDAS measurements, comments are left superficial as far as seen from the graphs and data. The main discussion will be made in the conclusion.

Table 4.1. Hardness test results

Position Number	1	2	3	4	5	6	7	8	9	10	11	
Sample	<b>HARDNESS BRINELL</b>											
<b>Ref. Sample</b>	<b>1st</b>	89.3	85.7	87.5	84.4	85.7	84.0	89.9	89.0	89.7	88.9	92.1
	<b>2nd</b>	88.4	88.1	87.7	88.8	87.0	86.2	83.7	89.1	87.9	89.1	93.0
	<b>3rd</b>	88.6	89.1	92.0	87.5	86.3	83.0	88.5	88.2	87.2	91.2	92.0
	<b>AVR</b>	88.8	87.6	89.1	86.9	86.3	84.4	87.4	88.8	88.3	89.7	92.4
	<b>STD</b>	0.5	1.7	2.5	2.3	0.7	1.6	3.3	0.5	1.3	1.3	0.6
<b>Batch 1</b>	<b>1st</b>	89.5	87.5	83.5	85.7	84.0	77.8	87.6	86.1	88.6	79.7	87.7
	<b>2nd</b>	86.1	85.0	83.1	86.3	84.9	84.7	84.3	88.6	86.4	87.5	90.3
	<b>3rd</b>	88.0	86.4	84.8	85.1	83.0	85.0	85.3	87.8	89.0	88.0	89.1
	<b>AVR</b>	87.9	86.3	83.8	85.7	84.0	82.5	85.7	87.5	88.0	85.1	89.0
	<b>STD</b>	1.7	1.3	0.9	0.6	1	4.1	1.7	1.3	1.4	4.7	1.3
<b>Batch 2</b>	<b>1st</b>	90.1	88.0	89.0	84.7	83.4	81.6	91.7	90.1	89.0	88.0	90.6
	<b>2nd</b>	84.3	84.0	86.2	87.7	84.4	88.1	85.0	88.5	88.1	86.7	89.3
	<b>3rd</b>	85.4	84.1	86.8	86.2	83.8	85.0	84.4	87.7	88.6	86.5	89.3
	<b>AVR</b>	86.6	85.4	87.3	86.2	83.9	84.9	87.0	88.8	88.6	87.1	89.7
	<b>STD</b>	3.1	2.3	1.5	1.5	0.5	3.3	4.1	1.2	0.5	0.8	0.8
<b>Batch 3</b>	<b>1st</b>	90.7	87.2	87.4	86.1	85.0	83.7	90.4	91.3	88.3	85.4	89.6
	<b>2nd</b>	84.3	85.0	85.0	87.7	84.1	84.0	84.4	85.0	86.4	89.3	90.1
	<b>3rd</b>	86.1	85.2	88.4	85.0	86.3	85.7	85.0	89.3	87.3	85.1	89.0
	<b>AVR</b>	87.0	85.8	86.9	86.3	85.1	84.5	86.6	88.5	87.3	86.6	89.6
	<b>STD</b>	3.3	1.2	1.7	1.4	1.1	1.1	3.3	3.2	1	2.3	0.6

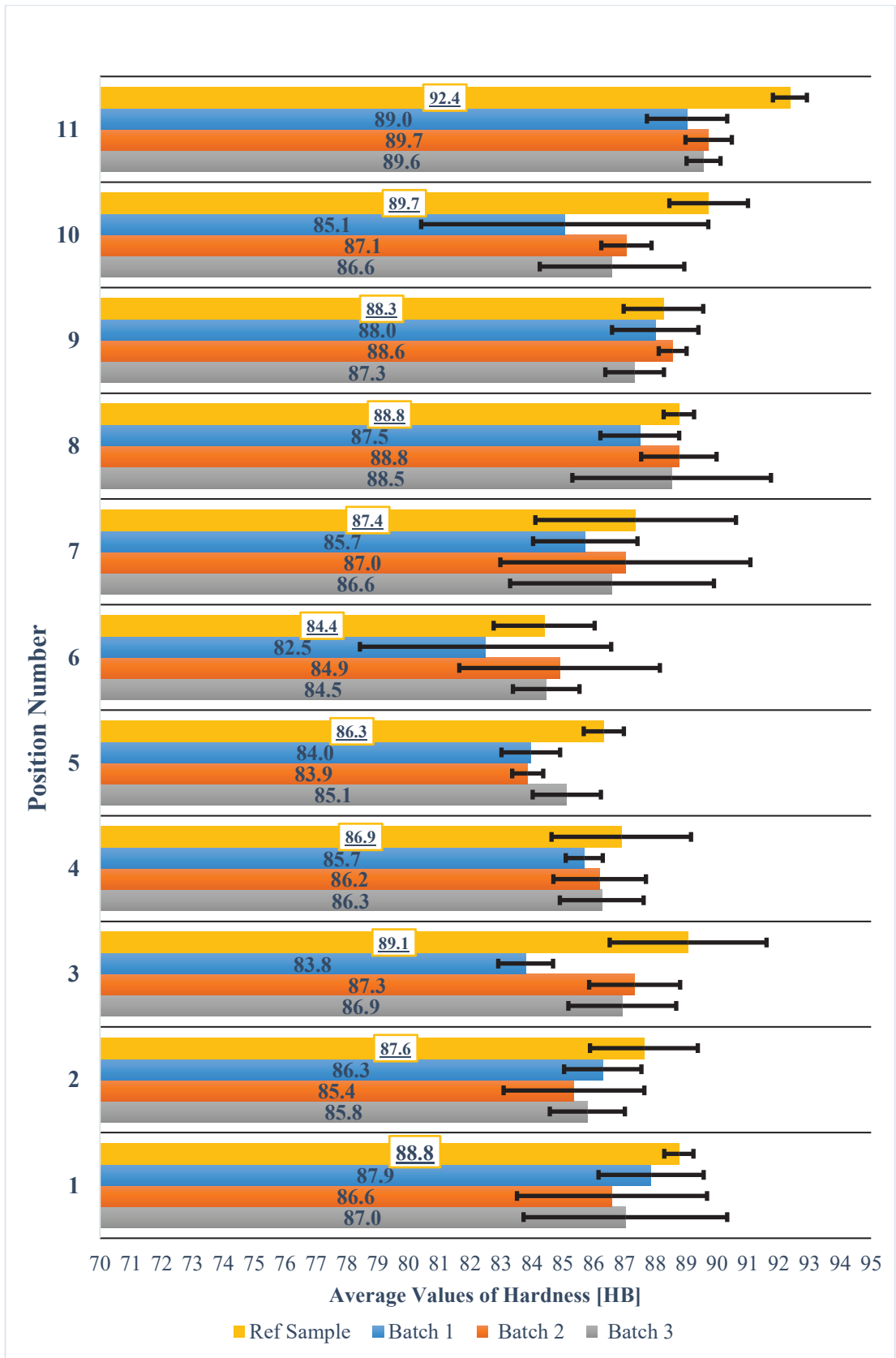


Figure 4.1. Average hardness test results

The reason for the hardness diminish in zones 4, 5, and 6 may be that the parameters in the spoke are set for the metal to feed. If the metal solidifies immediately in these regions, it will not be able to feed to the rim surface and tend to create casting defects. For this reason, the hardnesses also decreased as the cooling was running later in the spoke.

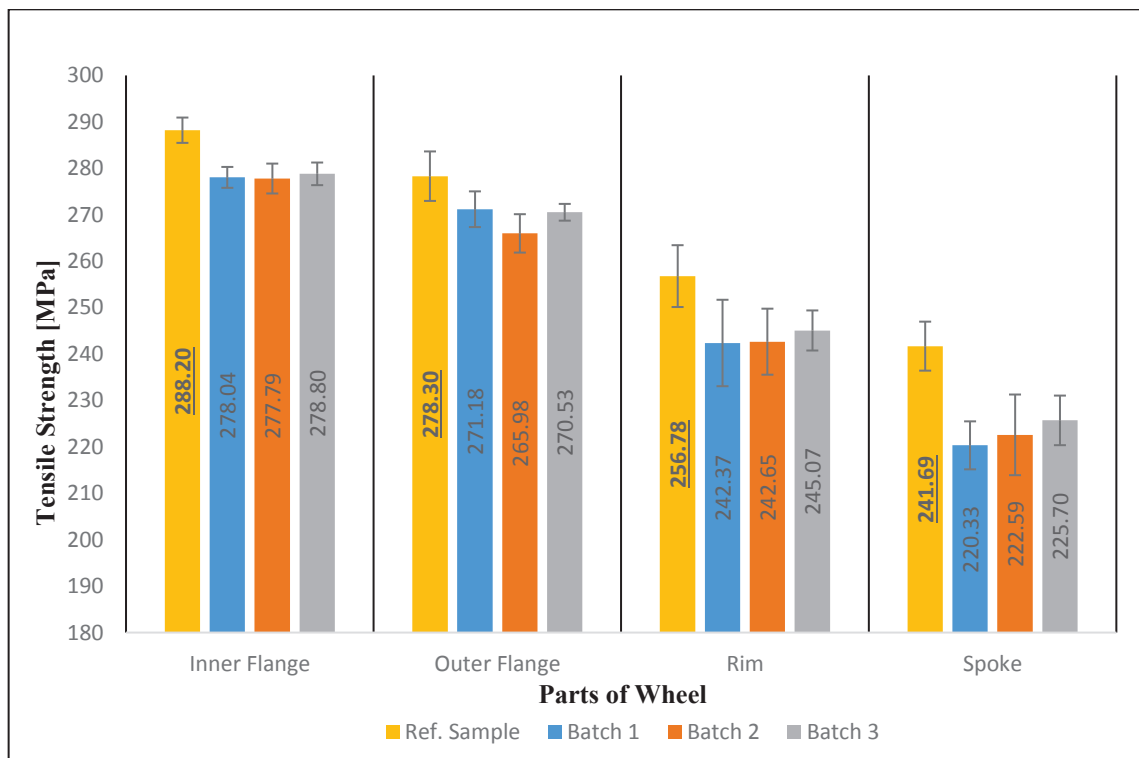


Figure 4.2. Tensile strength results

In this study, tensile bars were extracted from 4 different regions of the automobile wheel. Since the cooling rates in these regions were different, obviously different mechanical properties were observed. For this reason, it is necessary to compare the same regions among themselves. So, the same regions are gathered together. Batches are also indicated with the same color.

The averages of tensile strength results are given in figure 4.2. Although there was no significant difference between the reference specimen and the manganese added specimens, there was a difference between batch 1, batch 2, and the reference specimen in the spoke region.

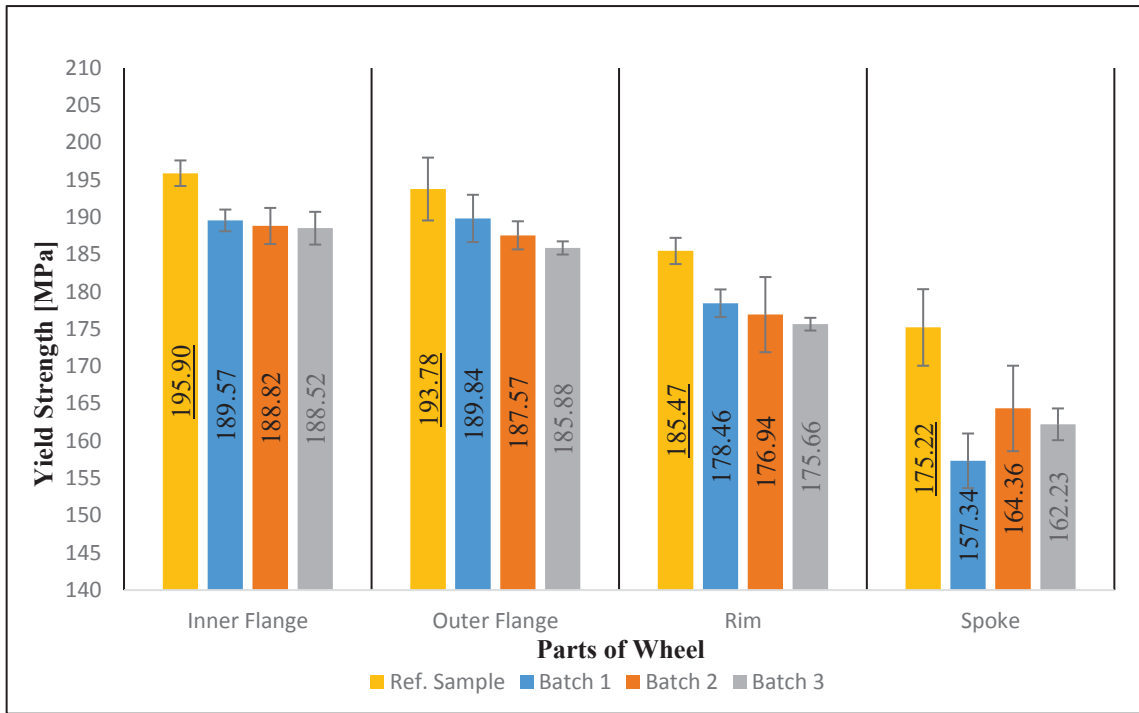


Figure 4.3. Yield strength results

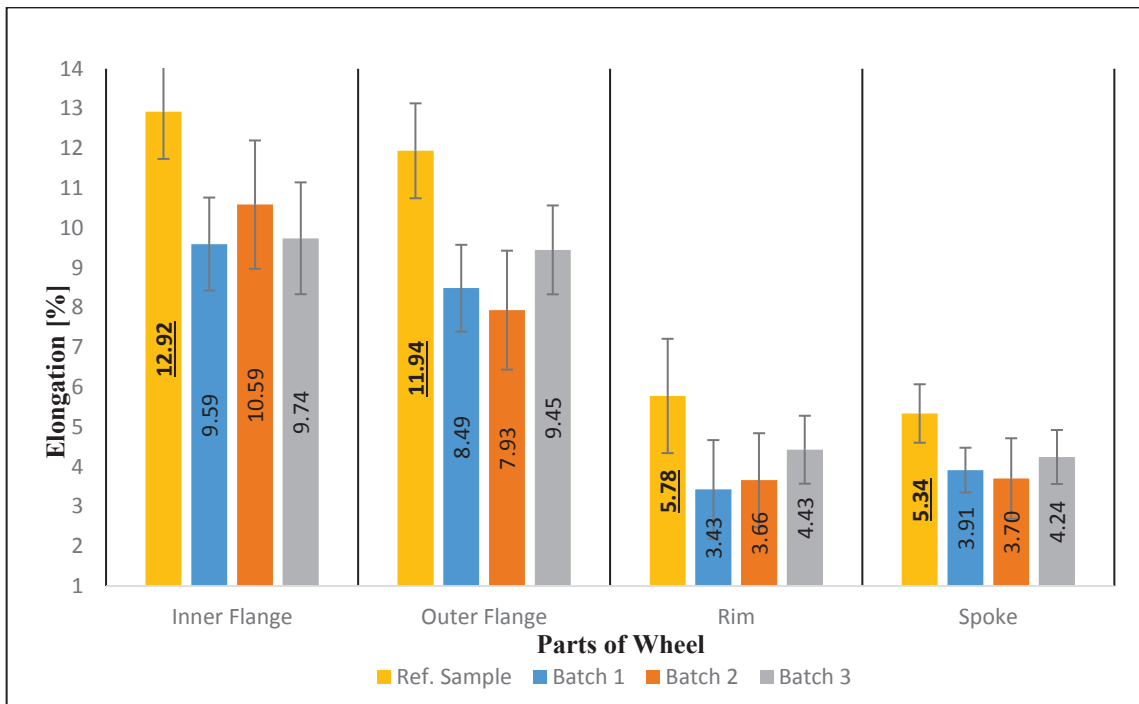


Figure 4.4. Elongation results

A decrease in hardness was observed in the manganese added batches. Although the decrease in other regions was around 4% when manganese added, it increased up to 9% in the spoke region.

The average values of yield strength were also plotted regionally. At these data, it can be said that it exhibits a similar behavior with tensile strength. A 9% decrease in the spoke compared to the hub, outer and inner flange region, where 2% and 3% decreases were observed, in batches with manganese additions.

Elongation generally develops inversely to yield strength. As the wheels are heat-treated, their strength values increase above a certain level, while the same mechanism reduces their ductility. When the batches with manganese addition are compared among themselves, batch 3 has the highest elongation except for the inner flange region. However, in parallel with the other tensile test results, lower values were obtained compared to reference samples.

Table 4.2. Arranged data of impact energy

<b>Sample</b>	<b>Batch 1 (Joule)</b>	<b>Batch 2 (Joule)</b>	<b>Batch 3 (Joule)</b>
1st	1.59	1.74	2.08
2nd	1.65	2.04	1.7
3rd	2.04	1.41	1.69
4th	1.76	1.89	1.84
5th	1.66	1.42	1.61
6th	1.89	1.68	2.31
Max	2.04	2.04	2.31
Min	1.59	1.41	1.61
AVR	1.74	1.68	1.83
STD	0.11	0.20	0.18

Charpy tests were carried out with specimens removed from the areas of the wheel that were most likely to be impacted as described in the previous section. 6 specimens from each batch were tested. All values are given in Table 4.2. Mean values and standard deviations by batch are also given with the abbreviations AVR and STD, respectively. After that, a graph was drawn using the average values of the impact energies obtained as a result of the Charpy test. In this graph, the values are given by calculating the error bars (standard deviations).



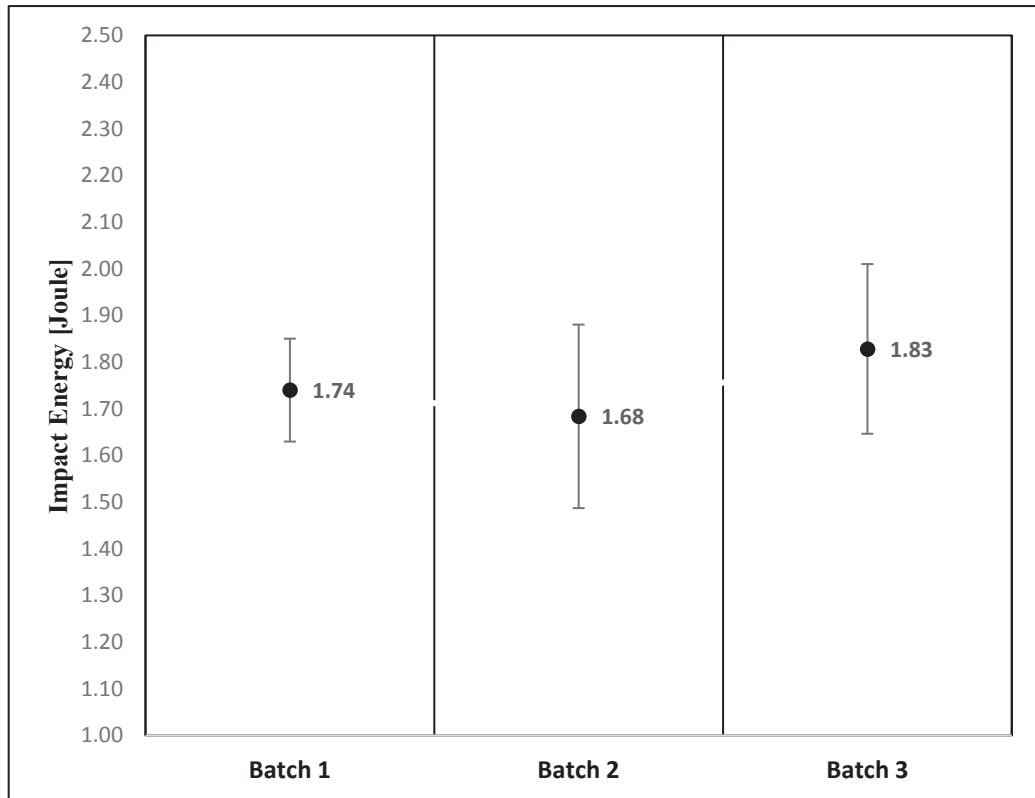


Figure 4.5. Average values of Charpy impact test

In the graph in Figure 4.5, the average values are plotted by neglecting the minimum and maximum values. Error bars are plotted based on standard deviation of samples.

According to the graph, the impact energy is higher in batch 3 where manganese addition is the highest. Although the values are very close to each other in general, it is really hard to be said that there is a significant difference between batch 1 and batch 2 considering the sensitivity of the test. Impact energy can be affected by intensity of porosity and oxides in the area where the sample is taken. On the other hand, iron intermetallics in the microstructure can also lead to significant differences. The amount of modification of the eutectic Si grains and the grain size also affect the strength and hardness of the specimen and will be discussed again in the following section.

Since sample production for batch zero was not possible in this test, only the impact energies in batches with Mn addition could be observed. In previous studies, it was observed that there was no significant difference in the results when the same test was repeated without Mn addition.

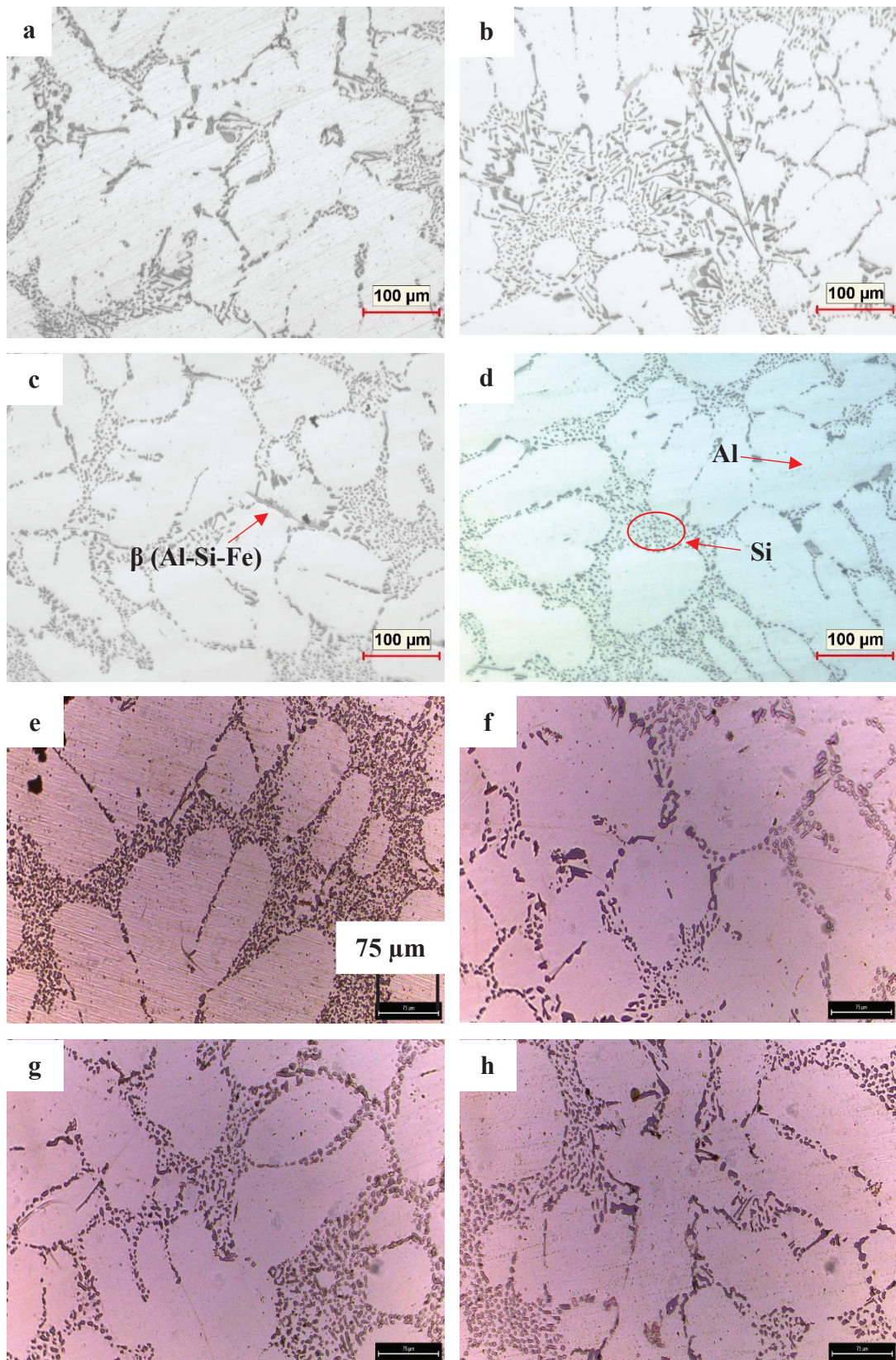


Figure 4.6. Optical microscopy images of hub section a) reference sample at 100x b) batch 1 at 100x c) batch 2 at 100x d) batch 3 at 100x e) reference sample at 200x f) batch 1 at 200x g) batch 2 at 200x h) batch 3 at 200x



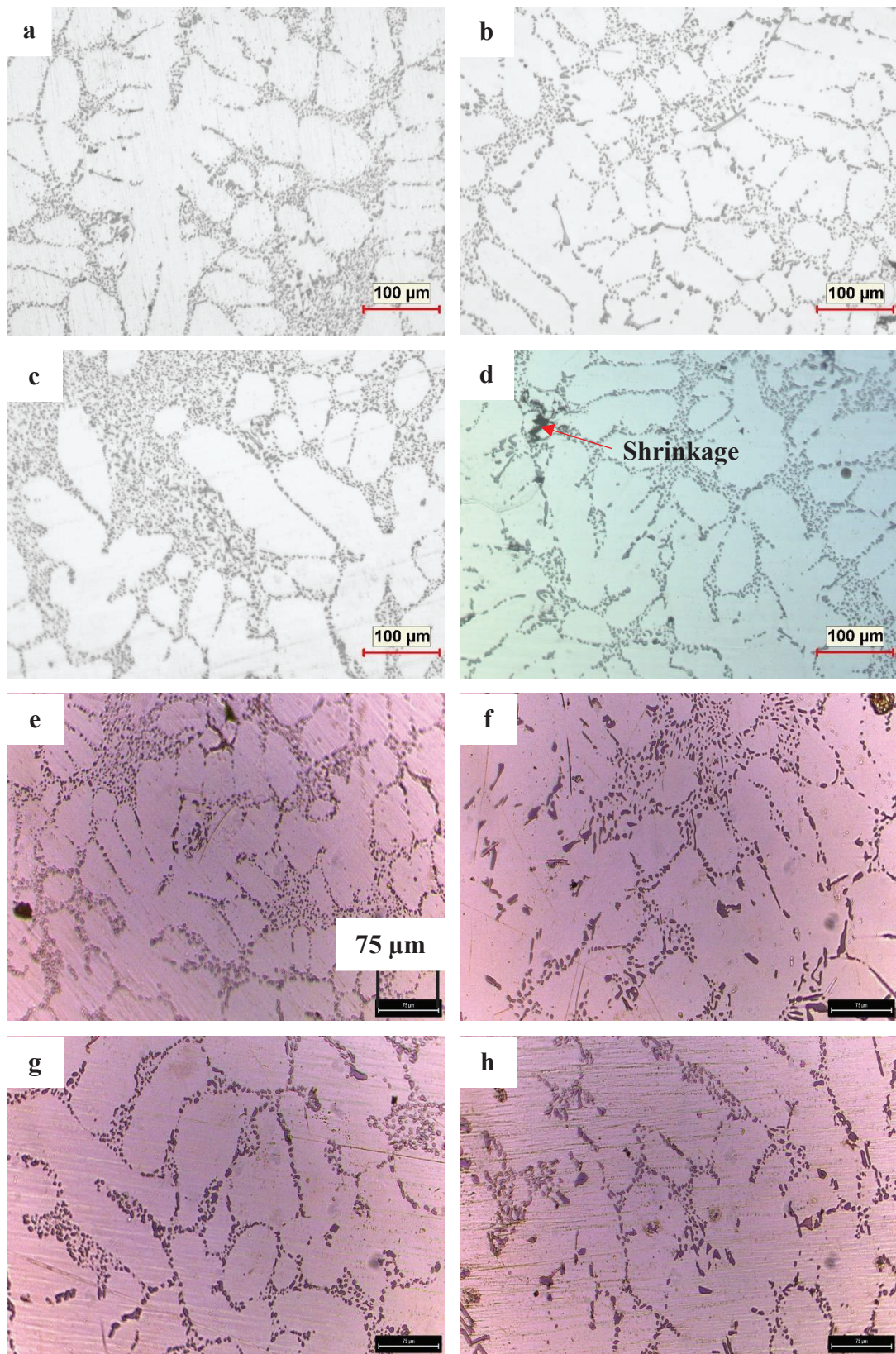


Figure 4.7. Optical microscopy images of spoke section a) reference sample at 100x b) batch 1 at 100x c) batch 2 at 100x d) batch 3 at 100x e) reference sample at 200x f) batch 1 at 200x g) batch 2 at 200x h) batch 3 at 200x



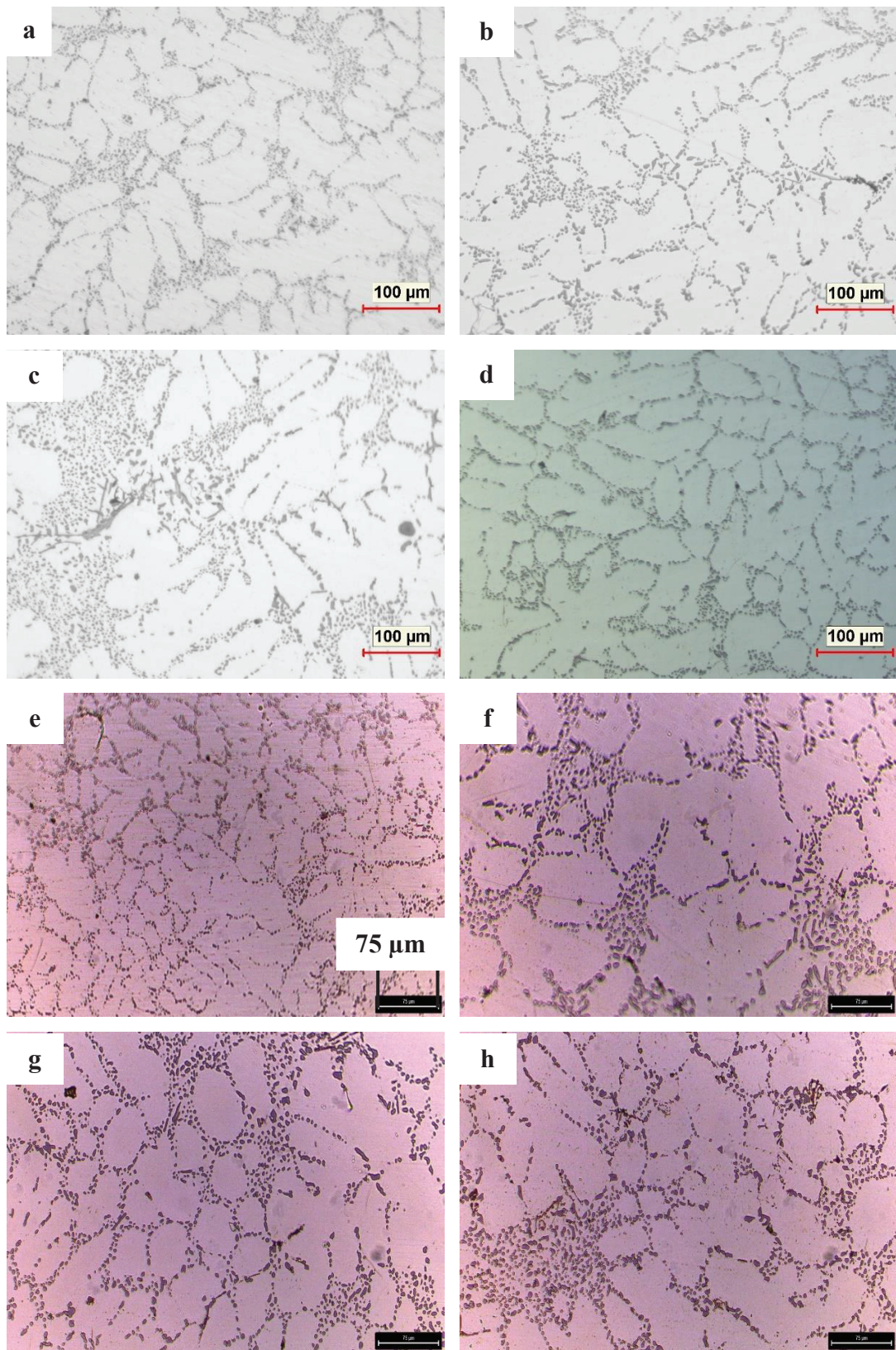


Figure 4.8. Optical microscopy images of rim section a) reference sample at 100x b) batch 1 at 100x c) batch 2 at 100x d) batch 3 at 100x e) reference sample at 200x f) batch 1 at 200x g) batch 2 at 200x h) batch 3 at 200x

Microstructure images were examined locally on the cross-section of the wheel. Images were taken from the main three regions: Hub, spoke, and rim. These images were examined at 100x and 200x magnification. In the images as like in figure 4.6 (d), the darker small particles are usually Si, while the light matrix is alpha aluminum. Their location is indicated by arrows. In addition, different intermetallic formations are also observed and marked in figure 4.6 (c). One of these is the frequently encountered Al-Si-Fe intermetallics. The shrinkage defect, which is one of the casting defects that occur during solidification, is also marked on the figures. The most critical information about the microstructures is the observation that the Si grains are smaller and more globular in the regions where the solidification is completed earlier due to the decrease in cross-sectional thickness as expected. This may be the reason why coarser grains and more needle-like Si grains are observed in the hub region. Since the hub part of the wheel is thicker, it will be the region that heats up the latest in heat treatment. For this reason, there may be areas where the modification is not completed. Numerical analysis of this will be done by drawing histograms in the following sections.

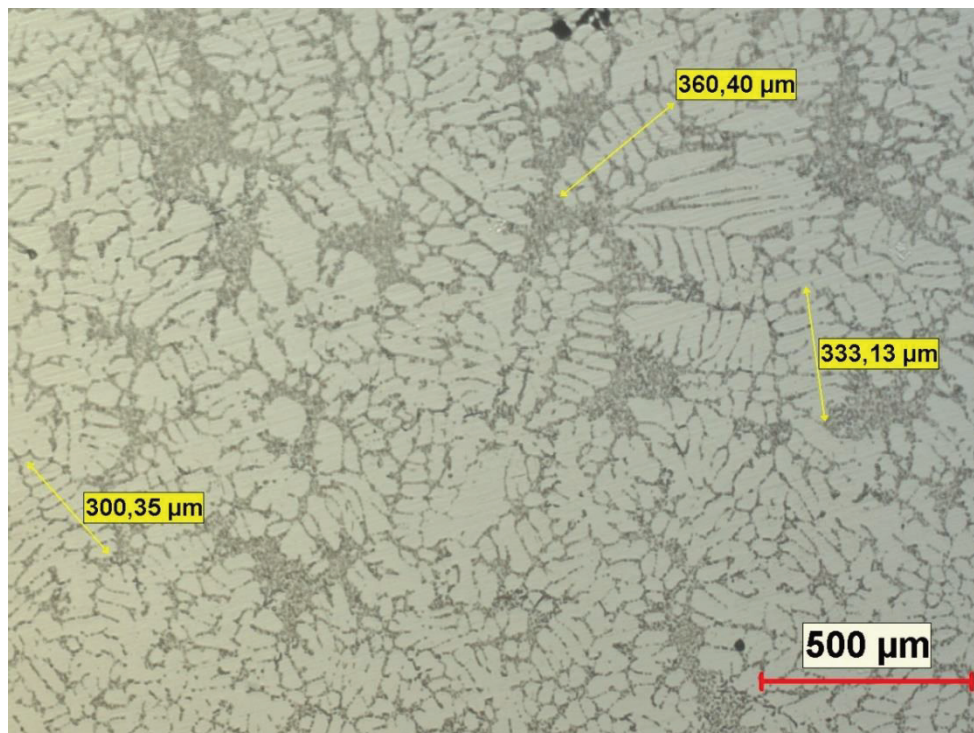


Figure 4.9. SDAS measurement at 25x magnification



Table 4.3. Arranged data of SDAS measurements

Batch	Section	SDAS ( $\mu\text{m}$ )	Number of Arms	SDAS per Arm
Batch 1	Hub	615.62	10	61.56
	Hub	451.14	10	45.11
	Hub	473.87	6	78.98
	<b>AVR</b>			<b>61.88</b>
	<b>STD</b>			<b>16.93</b>
Batch 1	Spoke	417.8	8	52.23
	Spoke	601.6	11	54.69
	Spoke	320.33	7	45.76
	<b>AVR</b>			<b>50.89</b>
	<b>STD</b>			<b>4.61</b>
Batch 1	Rim	300.35	9	33.37
	Rim	333.13	7	47.59
	Rim	360.4	8	45.05
	<b>AVR</b>			<b>42.00</b>
	<b>STD</b>			<b>7.58</b>
Batch 2	Hub	413.36	8	51.67
	Hub	312.35	5	62.47
	Hub	484.41	8	60.55
	<b>AVR</b>			<b>58.23</b>
	<b>STD</b>			<b>5.76</b>
Batch 2	Spoke	380.06	8	47.51
	Spoke	390.04	7	55.72
	Spoke	395.07	8	49.38
	<b>AVR</b>			<b>50.87</b>
	<b>STD</b>			<b>4.30</b>
Batch 2	Rim	194.44	6	32.41
	Rim	265.91	9	29.55
	Rim	390.78	10	39.08
	<b>AVR</b>			<b>33.68</b>
	<b>STD</b>			<b>4.89</b>
Batch 3	Hub	489.41	8	61.18
	Hub	402.53	5	80.51
	Hub	705.67	14	50.41
	<b>AVR</b>			<b>64.03</b>
	<b>STD</b>			<b>15.25</b>
Batch 3	Spoke	253.81	5	50.762
	Spoke	264.92	5	52.984
	Spoke	263.07	5	52.614

(Cont. on next page)



Table 4.3. (cont.)

	<b>STD</b>			<b>1.19</b>
	<b>AVR</b>			<b>52.12</b>
<b>Batch 3</b>	Rim	319.52	8	39.94
	Rim	203	6	33.83
	Rim	316.93	9	35.21
	<b>AVR</b>			<b>36.33</b>
	<b>STD</b>			<b>3.20</b>

SDAS measurements were taken at 25x magnification from the three regions identified in this study as shown in figure 4.9. Efforts were made to ensure that each dendrite had at least five arms. The measured values, number of dendrite arms and mean SDAS are given in table 4.3. AVR represents the mean and STD represents the standard deviation of the data. Based on this data, a graph was drawn with the average values by region as shown in figure 4.10.

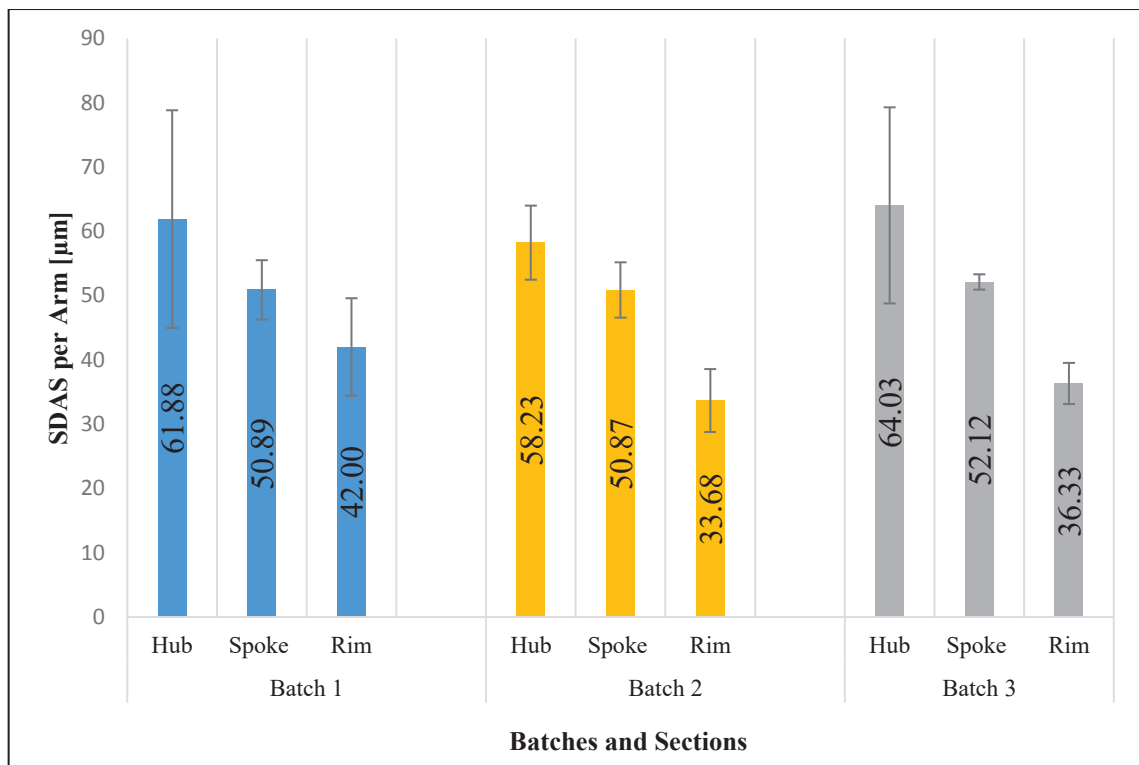


Figure 4.10. Averages of SDAS per arm

The mean SDAS is calculated by dividing the measured distance by the number of dendrites. SDAS values can be influenced by various factors like alloy composition, location of measurement points, distance from the surface, distance from cooling

channels. It is not always right decision comparing with other SDAS values. due to the reasons listed before it's depend on a few critical things. Most importantly, it relies on the operator's choose. Therefore it should always be criticise with other data like mechanical properties and microstructural images collected from sample. It is known that effective cooling, grain refinement affects SDAS. For this reason, it is expected that the SDAS size will decrease when moving from the hub region to the rim region in a regular manner between the regions. It can be said that the mechanical property decreases in Batch 1, which are also observed for other mechanical properties between batches, are not surprising when compared in terms of SDAS size. The relative good performance of Batch 2 in impact energy and other mechanical properties is also attributed to the shortest SDAS dimensions. However, as observed in the mechanical properties, there were no significant differences between batches.

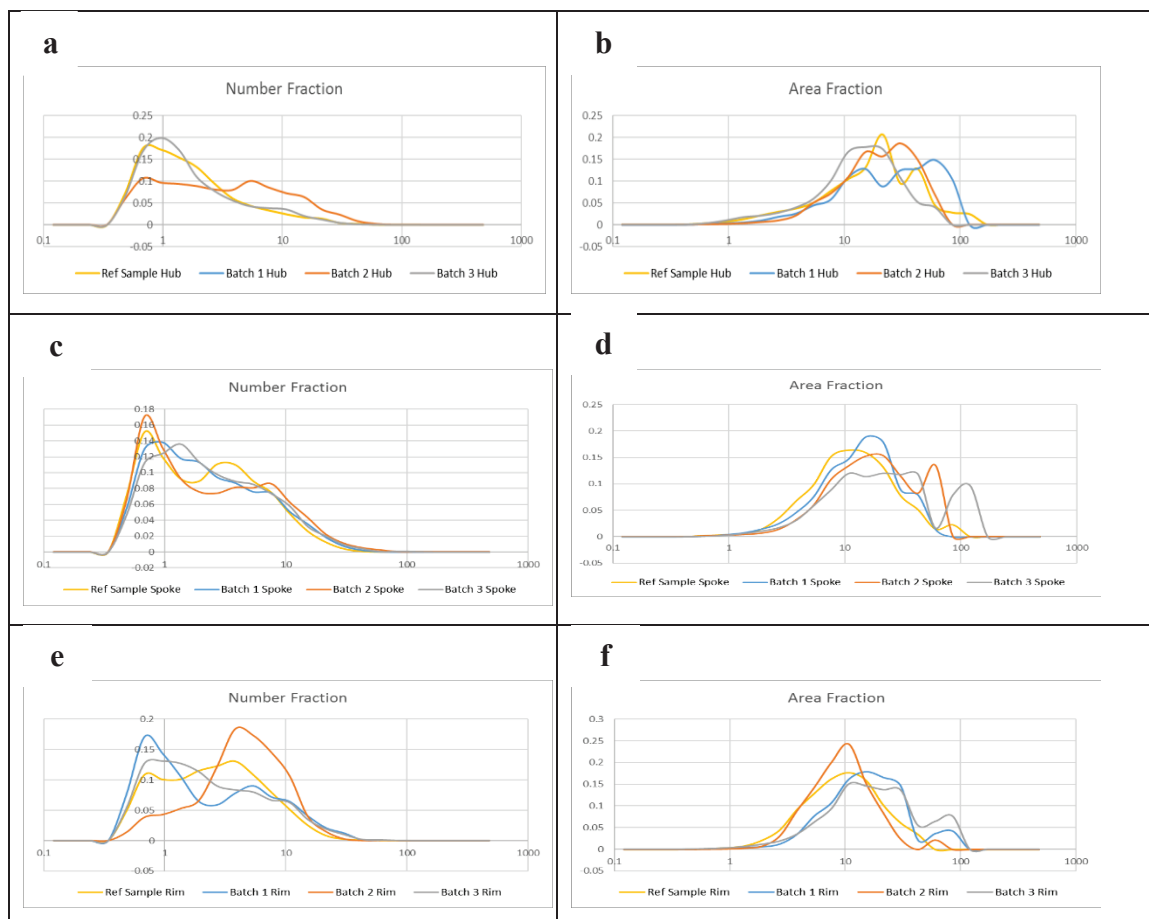


Figure 4.11. Major axis plotted histograms via ImageJ a) number fraction of hub b) area fraction of hub c) number fraction of spoke d) area fraction of spoke e) number fraction of rim f) area fraction of rim

As mentioned in the previous sections, optical light microscope photographs were taken and interpreted regionally. In this section, after converting these photographs into digital data and processing them with the ImageJ software, regional comparisons were made by creating histograms. The use of the program was explained in the previous section. Images smaller than 5 pixels were not included in the calculation to avoid errors. In Figure 4.11, there are graphs giving the distributions according to the state of the major axes. The major axis is the primary axis of the ellipse, the x-axis. ImageJ recognizes these particles as ellipses and gives an output in pixels. This output is converted to microns and the process continues. Here the size distribution of the elongated grains along the x-axis is shown.

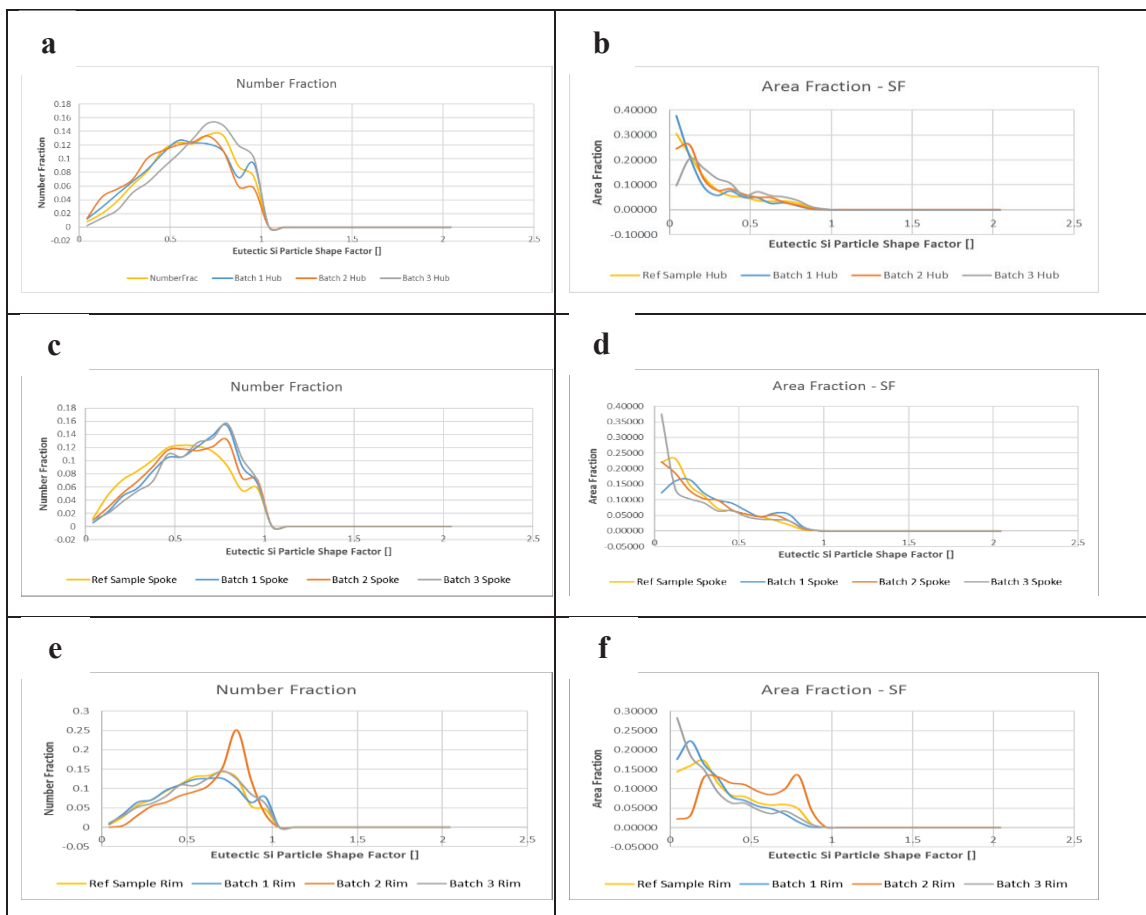


Figure 4.12. Circularity plotted histograms via ImageJ a) number fraction of hub b) area fraction of hub c) number fraction of spoke d) area fraction of spoke e) number fraction of rim f) area fraction of rim

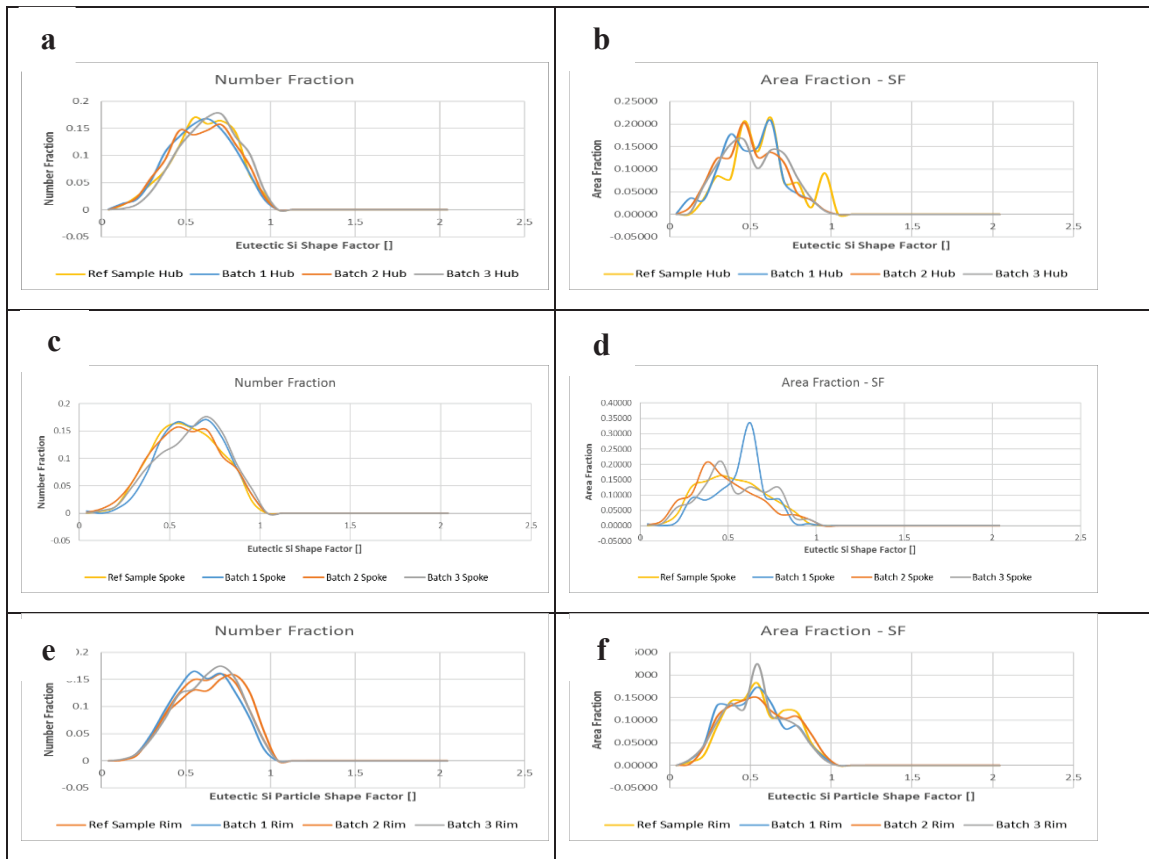


Figure 4.13. Aspect ratio plotted histograms via ImageJ a) number fraction of hub, b) area fraction of hub, c) number fraction of spoke, d) area fraction of spoke, e) number fraction of rim, f) area fraction of rim

Numerical distributions are given in the graphs on the left (a,c,e). Looking at these graphs, it is seen that the peaks occur in regions close to 1 micron. In other words, there are too many pieces close to 1 micron. However, it may be wrong to make this interpretation directly because when we look at the area distribution on the right side (b,d,f), it is understood that the grains close to 1 micron do not take up that much space when the area is considered. Accordingly, the peaks are generally distributed in the range of 10-100 microns.

Circularity is the area divided by the square of the perimeter. The graphs in figure 4.12 illustrate this property. It is clear from the formula that if a perfect ellipse is drawn, its value will be 1. Therefore, with this property, which shows a distribution between 0-1, the modification status of Si grains was analyzed depending on the regions. Looking at the graphs on the left side (a,c,e), it seems that peaks close to 1 were formed in all regions and excellent distributions were observed. But here only the distribution of the number of almost perfectly round Si grains is shown. Since these perfectly round grains do not

occupy much space in the area, the peaks in the area fraction are in the range 0-0.5. The batch 2 rim region showed the best modification. Localized peaks are observed in the spoke region, but the overall distribution is closer to 0. This supports the poor performance of the spoke region in terms of mechanical properties.

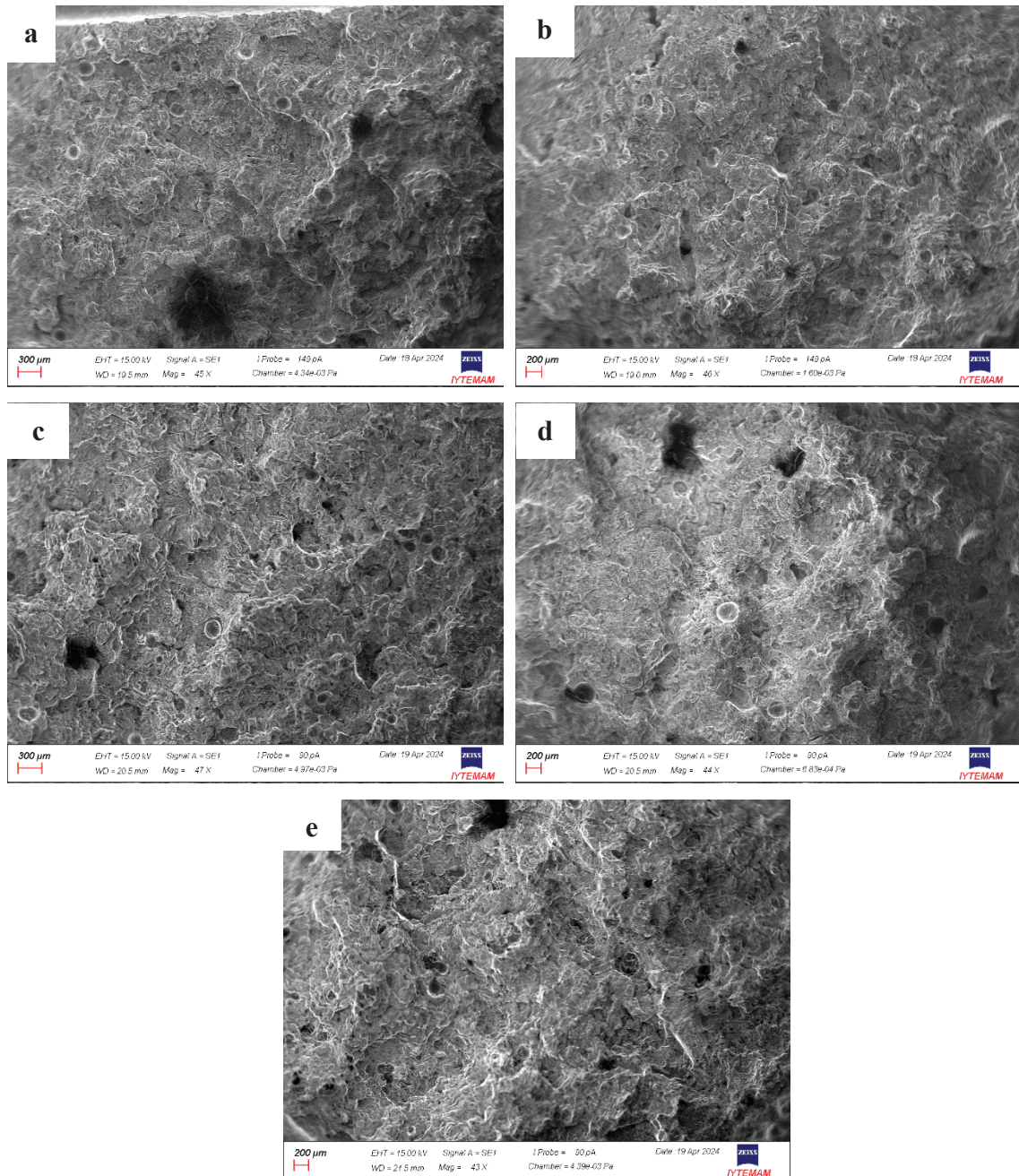
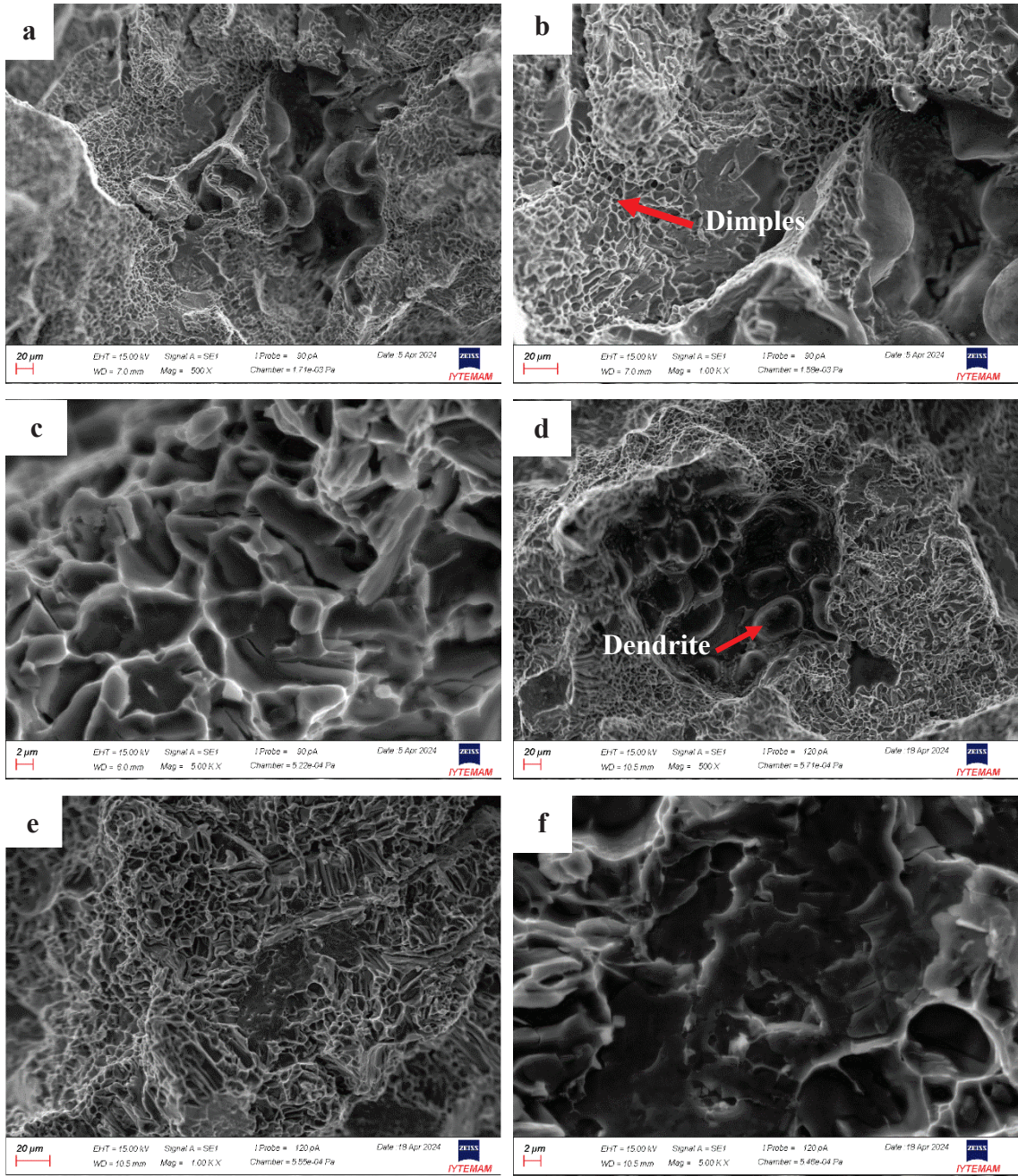


Figure 4.14. SEM images at 45x a) batch 1 4th, b) batch 3 1st, c) batch 2 5th, d) batch 2 6th, e) batch 3 4th





(cont. on next page)

Figure 4.15. SEM images of the fracture surface a) batch 1 4th 500x, b) batch 1 4th 1000x, c) batch 1 4th 5000x, d) batch 3 1st 500x, e) batch 3 1st 1000x, f) batch 3 1st 5000x, g) batch 2 5th 500x, h) batch 2 5th 1000x, i) batch 2 5th 5000x, j) batch 2 6th 500x, k) batch 2 6th 1000x, l) batch 2 6th 2500x, m) batch 3 4th 500x, n) batch 3 4th 1000x, o) batch 3 4th 5000x



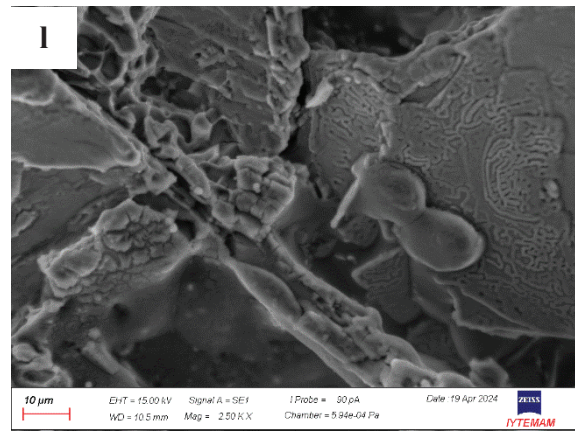
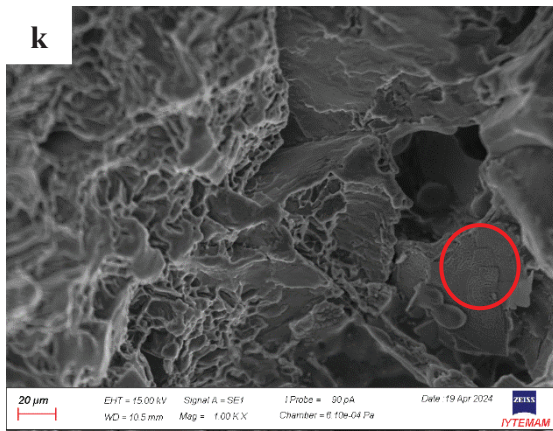
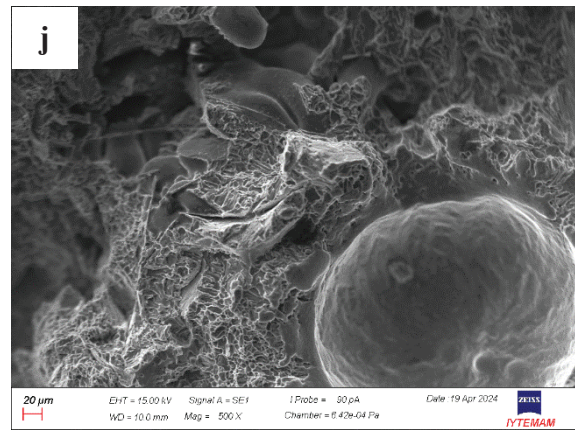
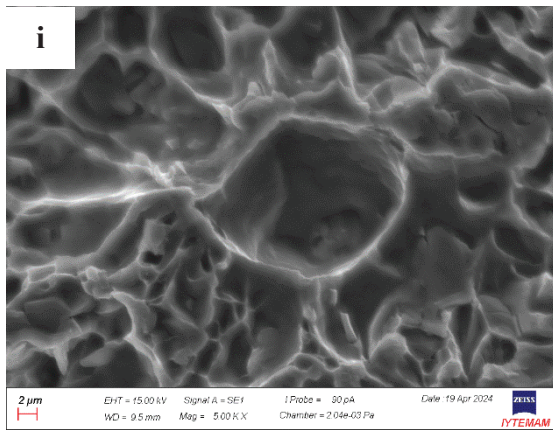
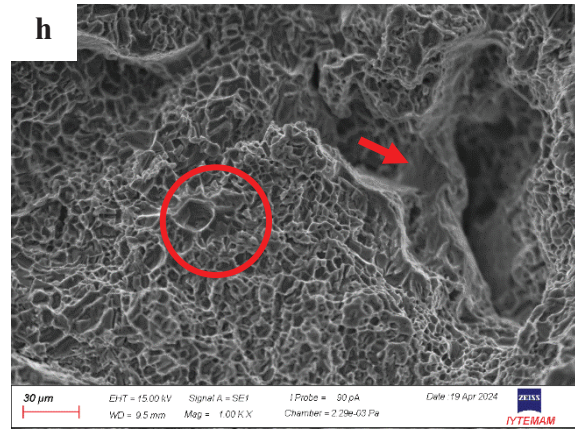
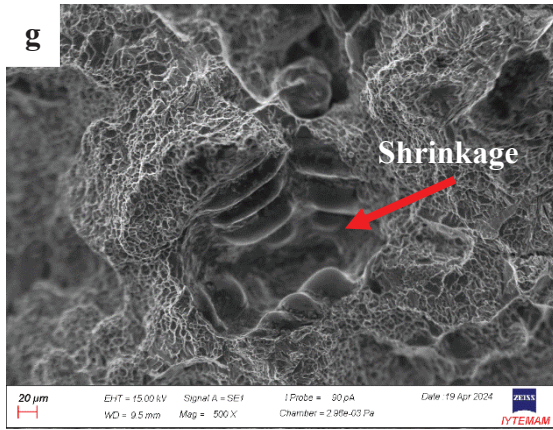
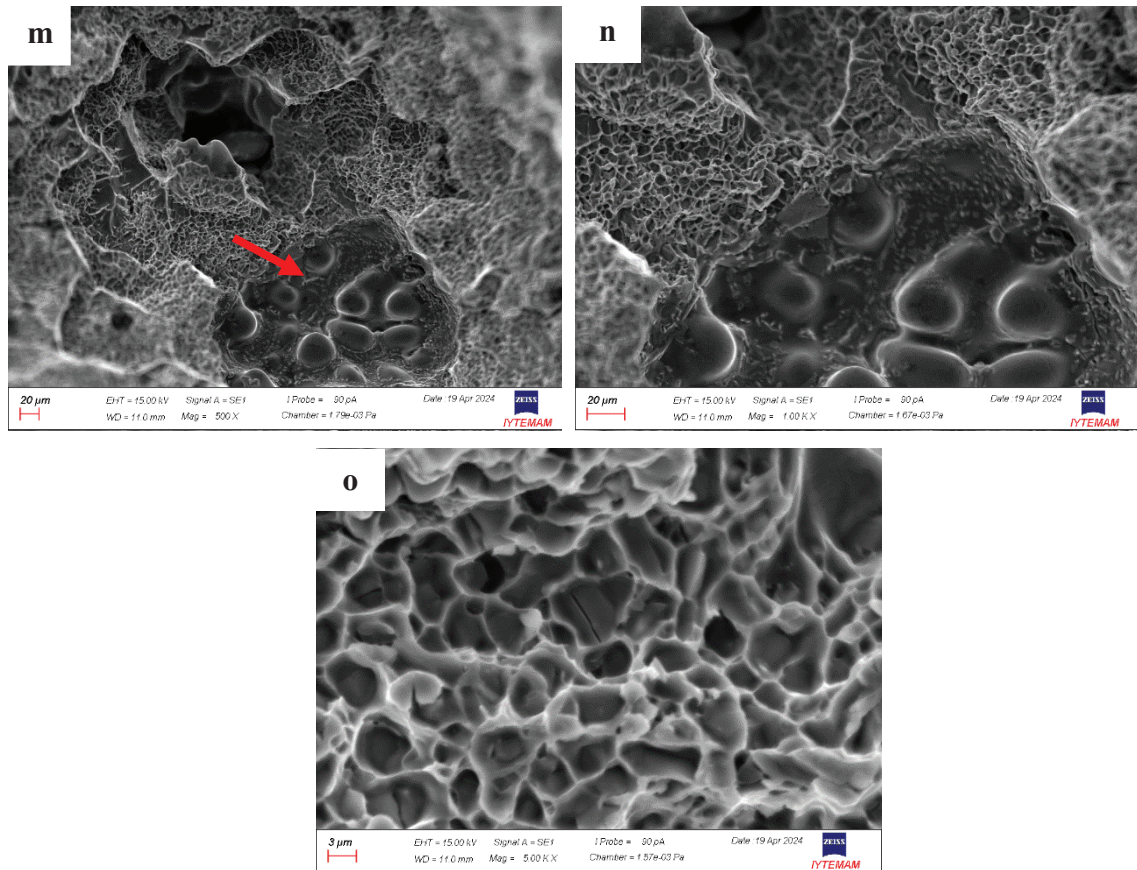


Figure 4.15. (cont.)



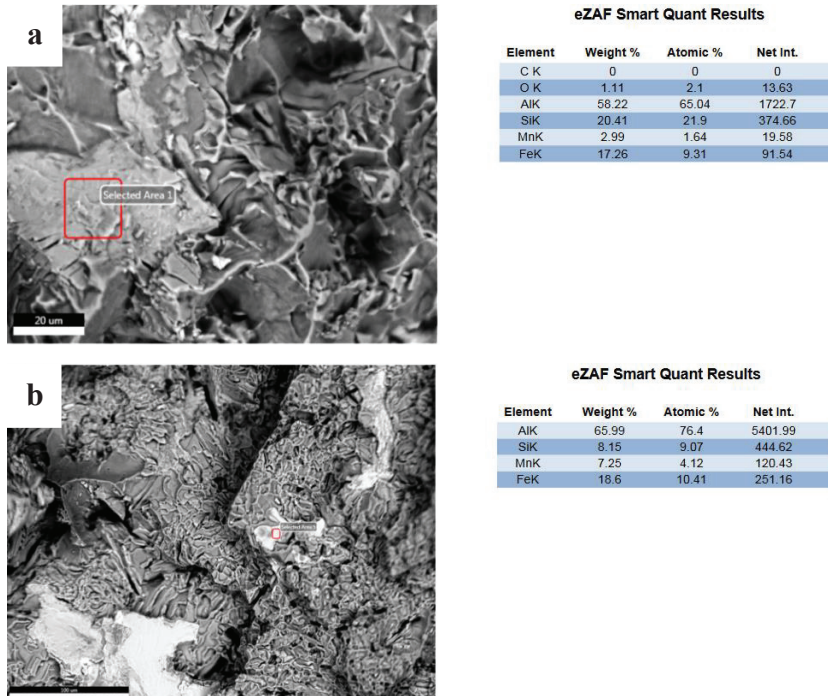
**Figure 4.15. (cont.)**

The fractured surfaces after the Charpy impact test were examined in scanning electron microscopy. A total of 6 fracture surfaces were examined. From each batch, a sample closest to the average value and the samples with the minimum and maximum values among all samples were examined. The images were taken from the secondary electron detector. Because of the capability of the depth of field. Fracture surfaces are intricately structured and that's why the technique requires depth of field. As can be seen in the photographs, the structure showed a ductile fracture for all batches to a pretty large extent. It is showed that from the cup and cone structures circled in red in figure 4.15 (h). When the red circled region is zoomed in 5000x (i), it can be easily seen that the grains actually did not break suddenly and catastrophically by forming an indented topography. However, it can be seen from the circular structure in figure 4.15 (k) that brittle fracture behavior is also observed in some areas. This is due to the direct fracture of the grain and the fact that it leaves no indentation before fracture. The dimple rich structure seen in Figure 4.15 (o) at 5000x magnification is another proof that ductile fracture is observed in the batch 3. Figure 4.15 (g) is an image of the sample with the lowest impact energy of 1.42 J among all samples. It can be seen, the possibility of shrinkage which is a casting



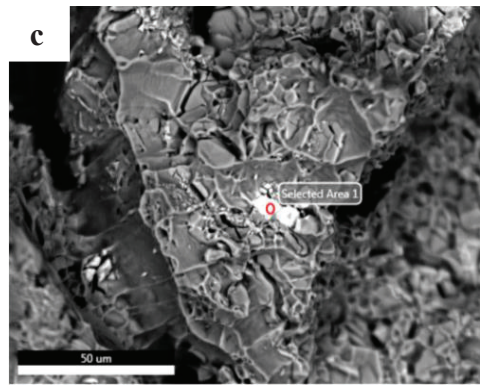
defect throughout the specimen weakened the mechanical properties. In addition, cleavage fracture is seen in the region marked with a red arrow in (h), which suggests that the fracture is also brittle locally. In contrast, the image seen in (e), which is the sample image with the highest impact energy value, is generally seen to form dimples.

In addition to images taken with the secondary electron detector in the scanning electron microscope, backscattered mode was also examined. As a result of this examination, the regions with compositional differences were analyzed elementally with the help of EDX detector. After this analysis, precipitates came together between the tear ridges and other light-colored structures were examined while aluminum was concentrated in the darker matrix. Fe and Mn were generally found together in the light-colored regions examined by field scanning. In figure 4.16 (b), the sample with the highest impact value, Al, Si, Fe, Mn, which are the basic elements we expect to see in the matrix, were observed, while impurities were observed in the light-colored areas in sample (c), where the lowest energy was observed. Along with P and Ca, trace amounts of O were also observed in the structure. Trace amounts of oxygen and matrix elements were observed in all other samples.



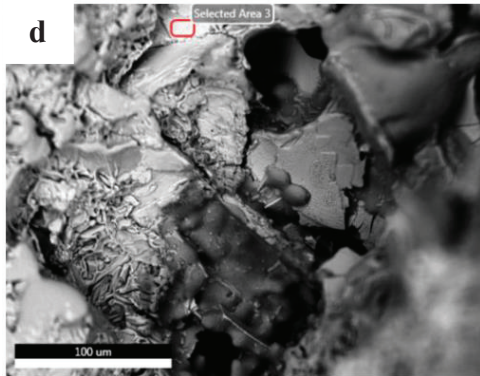
(cont. on the next page)

Figure 4.16. EDX results a) batch 1 4th, b) batch 3 1st, c) batch 2 5th, d) batch 2 6th, e) batch 3 4th



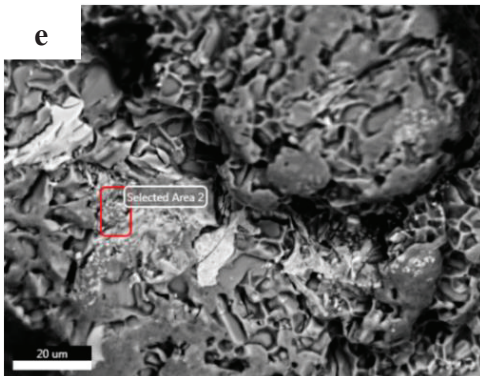
**eZAF Smart Quant Results**

Element	Weight %	Atomic %	Net Int.
O K	3.89	6.59	334.14
MgK	1.98	2.2	484.15
AlK	38.44	38.59	8909.65
SiK	48.81	47.08	8297.29
P K	4.45	3.89	498.33
CaK	2.43	1.64	208.17



**eZAF Smart Quant Results**

Element	Weight %	Atomic %	Net Int.
C K	3.7	10.8	8.57
O K	3.84	8.41	31.2
MgK	1.26	1.81	10.12
AlK	28.61	37.12	262.48
SiK	4.09	5.1	35.15
MnK	7.75	4.94	19.38
FeK	50.75	31.82	99.67



**eZAF Smart Quant Results**

Element	Weight %	Atomic %	Net Int.
O K	0.85	1.51	96.6
AlK	79.99	84.19	18379.33
SiK	9.02	9.12	1204.96
MnK	3.22	1.66	132.59
FeK	6.92	3.52	235.63

(Figure 4.16. cont.)

## 4.2. Simulation Results

The installed project was run as described in the previous sections. Various results were observed and 6 different project versions were tried to converge to the reality. In these versions, the entire parameters were kept constant and only the Mn level was changed inline with the experimental parameters. Since no change could be observed in the solidification curves, porosity dispersion, and other critical results. Then, comprehensive study was abandoned in the simulation. An attempt was made to achieve

convergence in the new version by simply setting the casting parameters as it was during the trial casting.

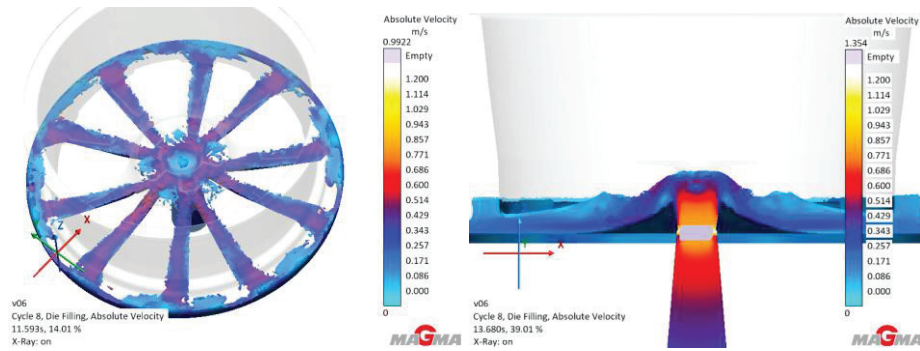


Figure 4.17. Die filling absolute velocity (m/s) results back and cross-sectional view

Die filling is a module where we are able to see how the mold cavity is filled at the end of the simulation depending on different variables. In figure 4.17, it is shown depending on absolute velocity and time. As the color shifts towards yellow, the filling speed of the metal increases. It is often repeated in the literature that 0.5 m/s should not be exceeded for an ideal casting. On the contrary, when parameters are taken as in the figure, it is observed that 0.5 m/s is exceeded in the spoke regions. In addition, it is seen that a strong turbulence occurs due to the bottleneck in the area where the metal starts to fill the mold in the mold filling, which is viewed as cross-sectionally. These undoubtedly have a negative effect on the mechanical properties of the wheel due to the folding oxide films.

Die filling can also occur depending on temperature and time. In figure 4.18, areas that remain hot and places where cold shots are likely to occur can be observed.

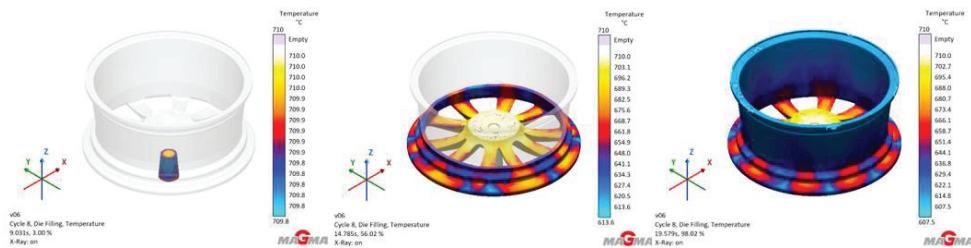


Figure 4.18. Die filling temperature results

Accordingly, cooling design or mold thickness can be altered. As expected and frequently mentioned in the previous sections, the hub area is the hottest area after the filling is completely finished, while at the spoke had medium temperature, the rim could cool down immediately.

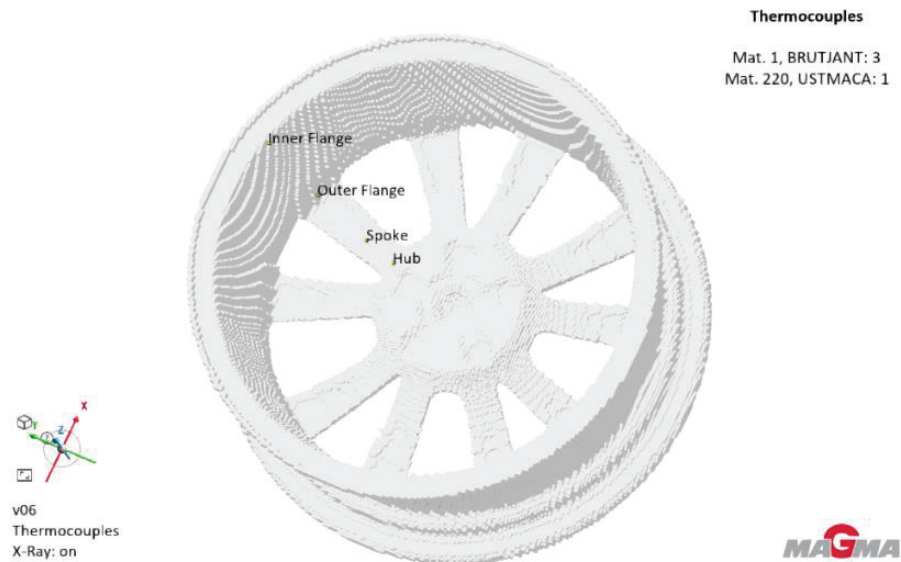


Figure 4.19. Termocouple inserted locations

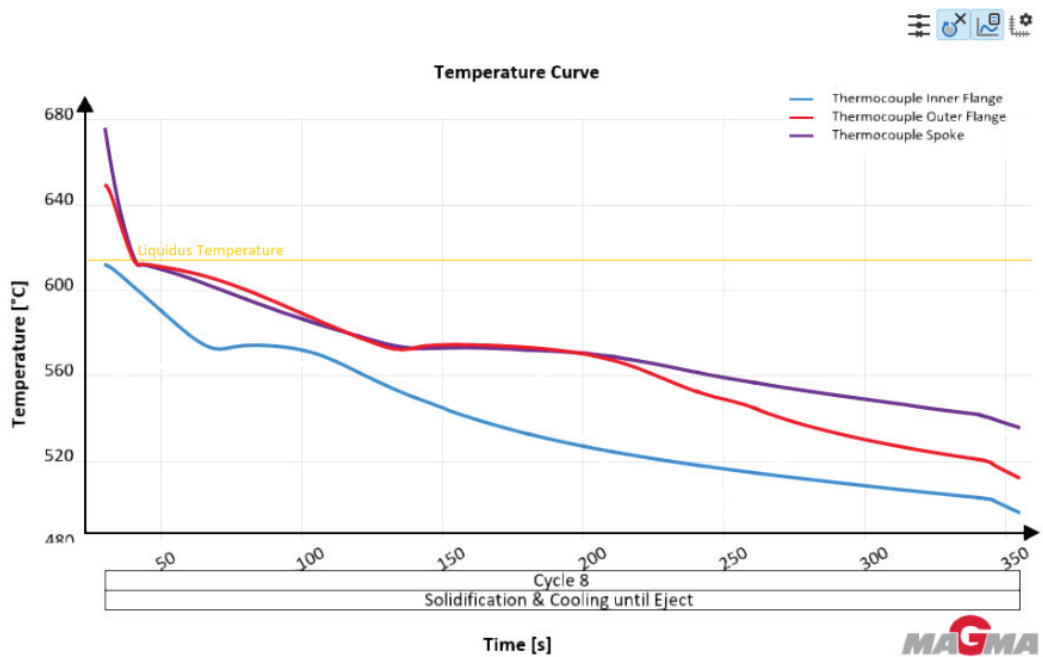


Figure 4.20. Termocouple data during solidification and cooling

MagmaSoft provides more than just information about mold filling; it also allows the study of various properties during solidification and cooling. Additionally, curves can be defined as if there were a virtual thermocouple in the desired regions. Each point shown in Figure 4.19 represents a thermocouple. Among these, only the thermocouple in the inner flange region is placed in the top core, while the others are positioned on the rim. When the temperature curves during solidification are examined in figure 4.20, it can be observed that due to directional solidification, the inner flange region, being closest to the rim, cools first, followed by the outer flange region, and finally the spoke region, which cools last. It is well known that the delayed cooling leads to grain growth, which negatively impacts mechanical properties.

### **4.3. Statistical Approach**

In the previous section, it was mentioned that it is difficult to directly correlate the length of major axis, circularity, aspect ratio values of the obtained from microstructure photographs through a software with the mechanical property values such as hardness, yield strength, percent elongation and impact energy. Therefore, "Multiple Linear Regression Analysis" (MLRA) was performed to take into account all microstructure parameters. MLRA is performed when determining the outcome of a dependent variable using two or more independent variables. Microstructure related parameters are circularity, aspect ratio, major axis, area fraction, SDAS, grains/mm<sup>2</sup>. Mechanical related parameters are elongation, tensile strength, yield strength, Brinell hardness, impact energy. Also, there is a parameter, Mn content, that is not related to either mechanical properties or microstructure.

These correlations were calculated using the Pearson Correlation Coefficient (PCC) equation. Statistically, the Pearson Correlation Coefficient measures the linear correlation between two variables, indicating the strength and direction of their relationship. A result of 1 signifies a perfect positive linear correlation, a result of zero indicates no linear correlation, and a result of -1 signifies a perfect negative linear correlation (Pearson and Galton, 1997).



In this study, a total of 62,798 data points were analyzed, including 669 related to mechanical properties and 62,129 related to microstructural properties. To interpret this extensive dataset, it was necessary to develop a statistical model.

When tables 4.4 and 4.5 are analyzed, it is found that some internal structure parameters are directly related to each other; in other words, these parameters are not considered independent of each other. Internal structure parameters were also found to have strong correlations among themselves. For example, as a result of the strong correlation between circularity and aspect ratio, circularity was removed from the analysis and aspect ratio was continued. Not only the simplest model was created by eliminating the parameters showing the same behavior with each other, but also it is ensured that the input parameters of the model are independent parameters.

It was observed that aspect ratio, grains/mm<sup>2</sup> and some mechanical properties showed strong correlations with each other after the values given in tables 4.4 and 4.5 also the values subtracted for similar behavior. Afterwards, the relationships between the mechanical property values and the specified microstructure parameters were examined. It was obtained that only the yield strength, elongation, and impact energy had a strong relationship between aspect ratio and grains/mm<sup>2</sup>.

Predictions were made by conducting a regression analysis (R-squared) of these values. These values are obtained to evaluate the goodness of fit of a regression model. If it is 1, then model explains all the variance in the dependent variable.

Analysis of Variance (ANOVA) was performed to further understand the relationship between strongly correlated parameters. ANOVA determines whether the observed differences are statistically significant. Therefore, significance F-values are shared to see how significant the analysis is. Lower than 0.15 is considered better. On the other hand, a sensitivity analysis was performed by using tornado charts to understand which microstructural feature is most sensitive to mechanical properties. In addition to these processes, Tornado plots were used to see the effect of increasing or decreasing each of the strongly correlated microstructure parameters by 10% on the yield strength, percent elongation and impact energy values.

Table 4.4. Pearson correlation values between microstructural and mechanical parameters for rim region

	Mn Content	YS	TS	e	Hardness	SDAS	Circularity (num)	Circularity (area)	Major (num)	Major (area)	Aspect ratio (num)	Aspect ratio (area)	Impact energy	Area frac	Grains/mm2
Mn Content	1														
YS	-0.850	1.000													
TS	-0.557	0.909	1.000												
e	-0.345	0.784	0.972	1.000											
Hardness	-0.451	0.778	0.911	0.906	1.000										
SDAS	-0.473	0.703	-0.296	-0.415	-0.997	1.000									
Circularity (num)	0.309	-0.492	-0.463	-0.424	-0.057	-0.883	1.000								
Circularity (area)	-0.188	-0.030	-0.117	-0.174	0.257	-0.703	0.872	1.000							
Major (num)	0.259	-0.586	-0.662	-0.666	-0.312	-0.711	0.951	0.815	1.000						
Major (area)	0.708	-0.570	-0.402	-0.262	-0.614	0.459	-0.402	-0.798	-0.331	1.000					
Aspect ratio (num)	0.452	-0.290	-0.031	0.104	0.354	-0.997	0.799	0.648	0.579	-0.283	1.000				
Aspect ratio (area)	-0.356	0.527	0.620	0.609	0.883	-0.943	0.406	0.673	0.170	-0.811	0.642	1.000			
Impact energy	-0.621	0.940	0.996	0.948	0.883	0.201	-0.507	-0.136	-0.683	-0.414	-0.112	0.582	1.000		
Area frac	0.842	-0.488	-0.137	0.080	-0.210	-0.082	-0.201	-0.608	-0.299	0.849	0.178	-0.382	-0.193	1.000	
Grains/mm2	-0.414	0.671	0.676	0.637	0.313	0.846	-0.966	-0.761	-0.984	0.221	-0.671	-0.158	0.711	0.133	1

Table 4.5. Pearson correlation values between microstructural and mechanical parameters for spoke region

	Mn Content	YS	TS	e	Hardness	SDAS	Circularity (num)	Circularity (area)	Major (num)	Major (area)	Aspect ratio (num)	Aspect ratio (area)	Impact energy	Area frac	Grains/mm2
Mn Content	1														
YS	-0.667	1.000													
TS	0.757	-0.989	1.000												
e	-0.491	0.946	-0.929	1.000											
Hardness	-0.054	0.719	-0.609	0.683	1.000										
SDAS	0.955	0.208	0.902	0.928	0.547	1.000									
Circularity (num)	0.786	-0.946	0.946	-0.791	-0.659	0.765	1.000								
Circularity (area)	-0.390	-0.416	0.283	-0.518	-0.874	-0.848	0.246	1.000							
Major (num)	0.691	-0.719	0.792	-0.794	-0.103	0.050	0.583	-0.058	1.000						
Major (area)	0.972	-0.483	0.597	-0.314	0.181	0.917	0.621	-0.592	0.643	1.000					
Aspect ratio (num)	0.667	-0.597	0.588	-0.309	-0.508	0.703	0.818	0.041	0.077	0.549	1.000				
Aspect ratio (area)	0.282	0.420	-0.282	0.405	0.933	0.572	-0.365	-0.931	0.233	0.493	-0.342	1.000			
Impact energy	-0.621	0.988	-0.981	0.983	0.682	0.923	-0.889	-0.432	-0.788	-0.445	-0.469	0.380	1.000		
Area frac	0.627	0.127	-0.020	0.371	0.527	0.996	0.147	-0.862	0.007	0.750	0.463	0.634	0.213	1.000	
Grains/mm2	-0.780	0.977	-0.998	0.925	0.556	-0.702	-0.930	-0.232	-0.829	-0.632	-0.558	0.219	0.975	-0.007	1

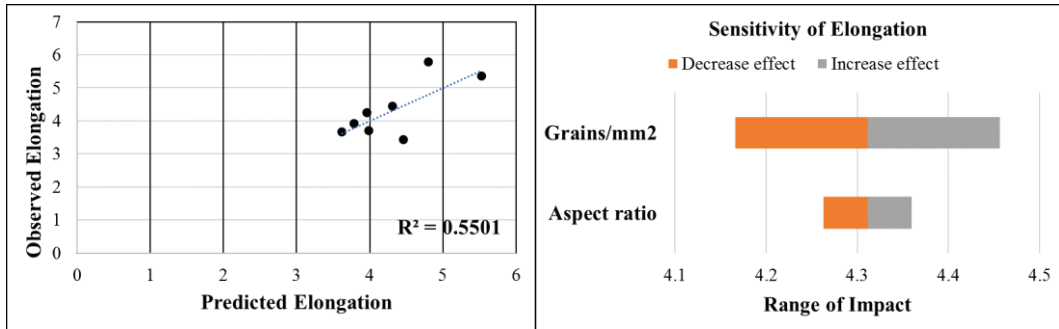


Figure 4.21. Significance, predicted values, and sensitivity analysis of elongation

Aspect ratio and grain/mm<sup>2</sup> values are the most sensitive parameters for the mechanical properties studied. In figure 4.21 shows the relationship with aspect ratio and grains/mm<sup>2</sup> parameters, which are the most affected parameters of elongation. The tornado graph illustrates the relative importance of various variables. The Significance F value indicates the statistical reliability of your results, making it a worthwhile metric to analyze. According to the coefficient of determination (R-squared), 55% of the values fit this regression analysis model. For elongation, the significance F value is 0.1357. Since this value is less than 0.15, it is consistent for further analysis. According to sensitivity analysis, a change in particle/mm<sup>2</sup> values affects the elongation value much more than a change in aspect ratio.

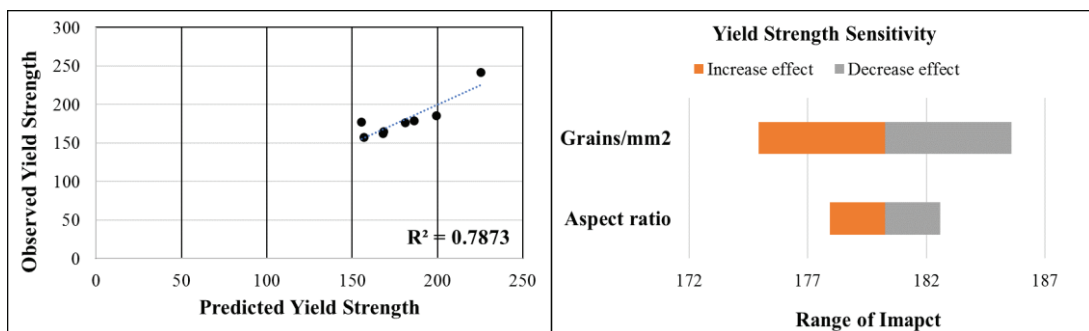


Figure 4.22. Significance, predicted values, and sensitivity analysis of yield strength

In figure 4.22, results of analyse were given for yield strength. The two most effective internal structure parameters are aspect ratio and grains/mm<sup>2</sup>, just like the elongation values. The behavior of these values is also more sensitive to grains/mm<sup>2</sup> as in elongation. 78.7 % of values fits this regression analysis model according to R square.

Also, significance F value is 0.0208 which means it's worth to analyse and make predictions. For elongation and yield strength values, the number of grains per square millimeter, grain size, is a more significant microstructure parameter than whether the grain is modified. Changes in grain size have a greater impact on these mechanical properties. This conclusion is supported by the F-value and R-squared values, which are meaningful statistical tools for making these interpretations.

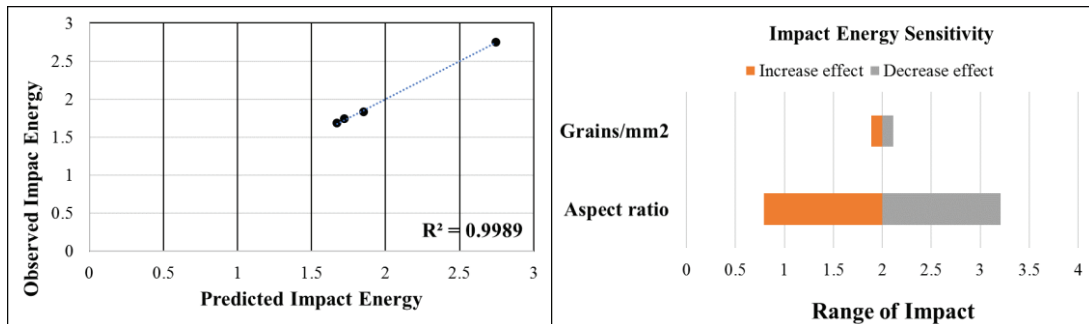


Figure 4.23. Significance, predicted values, and sensitivity analysis of impact energy

In figure 4.23, a model was created and a graph was drawn according to the microstructure parameters most affected by the impact energy. Unlike the mechanical properties obtained as a result of the tensile test, the aspect ratio of the grains is a much more decisive internal structure parameter. In other words, the aspect ratio of the grains has an effect on changing the impact energy rather than the size of the grains. Significance F value is 0.0336 and 99.9 % of values fits this regression analysis model according to R square.

## CHAPTER 5

### CONCLUSIONS

As expected, the hardness and yield strength values exhibited similar behavior across all samples. With regional increases and decreases mirroring each other. However, no significant differences were observed between the samples with added Mn. The only notable exception was the spoke region, which showed a yield strength value 9% lower than expected. This reduction may be attributed to turbulence observed in the spoke region, as discussed in the simulation section. This idea is supported by the shrinkage seen in optical microscope images and the porosities dispersed throughout the structure. The convergence of circularity number fraction values to 1 in the spoke region, as analyzed by ImageJ, also may indicate an excess of porosities larger than 5 pixels in size. Despite their presence, these porosities affect only a very small area and this can be easily said by looking at the area fraction curves. Additionally, when comparing aspect ratios and the area fraction of the spoke region, it is evident that Si modification is pretty ineffective (less than 0.5), except for the peak in batch 1, contributing to the decrease in mechanical properties.

Examining the fractured surfaces and energies reveals no significant differences between the samples. SEM images show extensive ductile fractures in nearly all samples, though some regions exhibit cleavage fractures. EDX detector scans confirmed the presence of Mn in all batches, consistent with the OES analysis. On the sample surface with an impact energy of 1.42 J, which was the lowest value among all samples, impurity elements like P and Ca were detected. Refractory wall of the gas-fired crucible could be caused these impurities mentioned in the experimental section. Alternatively, the flux content in the Mn tablets could have agglomerated in the liquid metal and entered the mold, contributing to this observation.

The turbulent flow in the spoke region, which is thought to be the cause of the low mechanical properties, may have originated from the runner inlet diameter indicated by the red circle.

A non-strong negative linear correlation between Mn concentration and mechanical properties was observed. Therefore, Mn addition is not the only and the strongest parameter for the decrease in mechanical properties.

Elongation and yield strength are strongly dependent on aspect ratio and grains/mm<sup>2</sup>. But they are more sensitive to grains/mm<sup>2</sup> than aspect ratio.

Impact energy is also strongly influenced on aspect ratio and grains/mm<sup>2</sup>. But oppositely, it is more sensitive aspect ratio than grains/mm<sup>2</sup>.



## REFERENCES

Ak, Meltem. 2012. "AA206 Alüminyum Döküm Alaşımında Empürite Demirin Mekanik Özelliklere Etkilerinin İncelenmesi." Istanbul Technical University.

Askeland, Donald R., Frank Haddleton, Phil Green, and Howard Robertson. 2013. *The Science and Engineering of Materials*. Springer.

ASM Handbook. 1990. *Properties and Selection: Nonferrous Alloys and Special-Purpose Materials*. Vol. 2. ASM International. <https://doi.org/10.31399/asm.hb.v02.9781627081627>.

ASM Handbook. 1991. *Heat Treating*. Vol. 4. ASM International.

Barrirero, Jenifer. 2019. "Eutectic Modification of Al-Si Casting Alloys." *Chemistry and Biology (IFM)*, Linköping Studies in Science and Technology., 2014 (October):5–46. <https://doi.org/10.3384/diss.diva-160235>.

Başer, Tanya Aycan. 2013. "Alüminyum Alaşımları ve Otomotiv Endüstrisinde Kullanımı." *Mühendis ve Makina*, January 15, 2013.

Becker, H., T. Bergh, P. E. Vullum, A. Leineweber, and Y. Li. 2019. "Effect of Mn and Cooling Rates on  $\alpha$ -,  $\beta$ - and  $\delta$ -Al-Fe-Si Intermetallic Phase Formation in a Secondary Al-Si Alloy." *Materialia* 5 (March):100198. <https://doi.org/10.1016/j.mtla.2018.100198>.

Bhutada, Govind. 2022. "How Is Aluminum Made?" Elements by Visual Capitalist. August 12, 2022. <https://elements.visualcapitalist.com/how-is-aluminum-made/>.

Biol, Yucel. 2014a. "Grain Refinement and Modification of Al-Si Foundry Alloys with B and Sr Additions." *Materials Science and Technology* 30 (August):1154–61. <https://doi.org/10.1179/1743284713Y.0000000392>.

Biol, Yucel. 2014b. "Grain Refining AlSi7Mg0.3 Foundry Alloy with Commercial Al-4B Master Alloy." *Materials Science and Technology* 30 (April):465–70. <https://doi.org/10.1179/1743284713Y.0000000380>.

Borecki, Michal, Arkadiusz Rychlik, Li Zan, and Michael Korwin-Pawlowski. 2024. "Steel Automotive Wheel Rims—Data Fusion for the Precise Identification of the Technical Condition and Indication of the Approaching End of Service Life." *Materials* 17 (January):475. <https://doi.org/10.3390/ma17020475>.

Campbell, Flake C. 2012. *Lightweight Materials: Understanding the Basics*. ASM International.

Campbell, John. 2004. *Castings Practice: The Ten Rules of Castings*. 1st ed. Butterworth-Heinemann.

Can Dizdar, Kerem, Hayati Sahin, Furkan Tezer, and Derya Dispinar. 2022. "Characterization of Casting Properties of Rare-Earth Modified A356." In *Aluminium Alloys - Design and Development of Innovative Alloys, Manufacturing Processes and Applications*, <https://doi.org/10.5772/intechopen.101722>.

"Car Steel Wheels." n.d. EUWA. Accessed April 27, 2024. <https://www.euwa.org/products/car-steel-wheels/>.

Çetin, Arda, and Ali Kalkanli. 2009. "Investigation of Microporosity Formation Mechanisms in A356 Aluminium Alloy Castings." *International Journal of Microstructure and Materials Properties* 4 (January). <https://doi.org/10.1504/IJMMP.2009.031143>.

"Cevher." n.d. Accessed April 30, 2024. <https://www.cevher.com/#/development-and-production/production>.

"Circular Aluminium Action Plan." 2020. Belgium: European Aluminum. [https://european-aluminium.eu/wp-content/uploads/2022/08/2020-05-13\\_european-aluminium\\_circular-aluminium-action-plan\\_executive-summary.pdf](https://european-aluminium.eu/wp-content/uploads/2022/08/2020-05-13_european-aluminium_circular-aluminium-action-plan_executive-summary.pdf).

Davis, Joseph R. 1993. *Aluminum and Aluminum Alloys*. ASM International.

"Delivering the European Green Deal - European Commission." n.d. Accessed April 7, 2024. [https://commission.europa.eu/strategy-and-policy/priorities-2019-2024/european-green-deal/delivering-european-green-deal\\_en](https://commission.europa.eu/strategy-and-policy/priorities-2019-2024/european-green-deal/delivering-european-green-deal_en).

Do Lee, Choong. 2018. "Effect of Artificial Ageing on the Defect Susceptibility of Tensile Properties to Porosity Variation in A356 Aluminium Alloys." *International Journal of Metalcasting* 12 (2): 321–30. <https://doi.org/10.1007/s40962-017-0168-1>.

Edwin Raja Dhas, J., M. Edwin Sahayaraj, K. Anton Savio Lewise, P. M. Akhil, and A. Sudhakar. 2023. "Design and Fabrication of Automobile Wheel Rim Using Composite Materials." *Materials Today: Proceedings*, July. <https://doi.org/10.1016/j.matpr.2023.06.413>.

Fan, Pan, Steve Cockcroft, Daan Maijer, Lu Yao, Carl Reilly, and Andre Phillion. 2018. "Examination and Simulation of Silicon Macroseggregation in A356 Wheel Casting." *Metals* 8 (7): 503. <https://doi.org/10.3390/met8070503>.

Fasching, Andreas. 2015. "Thermodynamische Berechnung der Einflüsse von Spurenelementen auf der Bildung intermetallischer Phasen bei Al- Gusslegierungen." Montanuniversität Leoben.

Fleming, Siobhan. 2012. *An Overview of Magnesium Based Alloys for Aerospace and Automotive Applications*.

Gardie, Eneyw, Velmurugan Paramasivam, Habtamu Dubale, Ewnetu Tefera Chekol, and Senthil Kumaran Selvaraj. 2021. "Numerical Analysis of Reinforced Carbon Fiber Composite Material for Lightweight Automotive Wheel Application." *Materials Today: Proceedings*, 3rd International Conference on Materials, Manufacturing and Modelling, 46 (January):7369–74. <https://doi.org/10.1016/j.matpr.2020.12.1047>.

Geller, Tom. 2007. "Aluminum: Common Metal, Uncommon Past." *Science History Institute*, 2007. Archived from the original on 2019-04-26.

Grjotheim, Kai, Conrad Krohn, Milan Malinovsky, Kamil Matiasovsky, and Jomar Thonstad. 1982. *Aluminium Electrolysis*. 2nd ed. Düsseldorf.

Güneren, Alper. 2019. "T6 Heat Treatment Optimization Of A356 Alloy." Dokuz Eylül University.

Guofa, Mi, Liu Xiangyu, Wang Kuangfei, and Fu Hengzhi. 2009. "Numerical Simulation of Low Pressure Die-Casting Aluminum Wheel." *China Foundry* 6 (February).

Gursoy, O., A. Nordmak, F. Syversten, M. Colak, K. Tur, and D. Dispinar. 2021. "Role of Metal Quality and Porosity Formation in Low Pressure Die Casting of A356: Experimental Observations." *Archives of Foundry Engineering* Vol. 21, iss. 1. <https://doi.org/10.24425/afe.2021.136071>.

Haque, Mohafizul Md, and Md Abdul Maleque. 1998. "Effect of Process Variables on Structure and Properties of Aluminium–Silicon Piston Alloy." *Journal of Materials Processing Technology* 77 (1–3): 122–28.

Huang, Li-Wu, Pi-Wein Wang, Teng-Shih Shih, and Jenq-Hwu Liou. 2002. "Effect of Degassing Treatment on the Quality of Al7Si and A356 Melts." *Materials Transactions - MATER TRANS* 43 (January):2913–20. <https://doi.org/10.2320/matertrans.43.2913>.

"ISO 148-1 2009 Metallic Materials — Charpy Pendulum Impact Test." 2009.

Kan, Wen Hao, Yves Nadot, Matthew Foley, Lionel Ridosz, Gwénaëlle Proust, and Julie M. Cairney. 2019. "Factors That Affect the Properties of Additively-Manufactured AlSi10Mg: Porosity versus Microstructure." *Additive Manufacturing* 29 (October):100805. <https://doi.org/10.1016/j.addma.2019.100805>.

Karabulut, Cansu, Gülce Malkoç, A. Yiğit Kaya, Onur Özaydin, and Paşa Yayla. 2023. "Influence of Different Fe Levels on Mechanical Properties of AlSi7Mg0.3 Aluminum Casting Alloys." *International Journal of Metalcasting*, December. <https://doi.org/10.1007/s40962-023-01227-y>.

Kaufman, John Gilbert, and Elwin L. Rooy. 2004. *Aluminum Alloy Castings: Properties, Processes, and Applications*. ASM International.

Kaya, A. Yiğit, Onur Özaydin, Tuğçe Yağcı, Adem Korkmaz, Elvan Armakan, and Osman Çulha. 2021. "Effect of Chip Amount on Microstructural and Mechanical Properties of A356 Aluminum Casting Alloy." *Archives of Foundry Engineering* 21 (July):19–26. <https://doi.org/10.24425/afe.2021.136108>.

Kaya, Yiğit, Onur Özaydin, Esra Dokumacı, and Elvan Armakan. 2019. "Farklı Döküm Aşamalarındaki Sıvı Metal Akışkanlığının İncelenmesi." in İzmir.

Kırmızıgöl, Süleyman, Onur Özaydin, Sercan Acarer, and Elvan Armakan. 2020. "Fluid Flow and Heat Transfer Simulations of the Cooling System in Low Pressure Die Casting" 16 (June):161–68. <https://doi.org/10.18466/cbayarfbe.641177>.

Korkut, Talha, Elvan Armakan, Onur Özaydin, K. Ozdemir, and Aytac Goren. 2020. "Design and Comparative Strength Analysis of Wheel Rims of a Lightweight Electric Vehicle Using Al6063 T6 and Al5083 Aluminium Alloys" 2 (April):57–63. <https://doi.org/10.5604/01.3001.0014.1776>.

Korkut, Talha, Aytac Goren, Onur Özaydin, and Elvan Armakan. 2019. "Aerodynamic Effects of Composite Wheel Cover on Electric Vehicle (EV) (PART A)" 8 (January):20–24.

Kuchariková, Lenka, Eva Tillová, and Otakar Bokuvka. 2017. "Recycling and Properties of Recycled Aluminum Alloys Used in the Transportation Industry." *Transport Problems* 11 (2): 117–22. <https://doi.org/10.20858/tp.2016.11.2.11>.

Kutsal, Umit, Yağız Arslan, Onur Özaydin, Yağız Akyildiz, A. Yiğit Kaya, and Onur Ertugrul. 2023. "Heat Treatment Simulation of Aluminum Alloy Wheels and Investigation of Process Steps." *International Journal of Metalcasting*, August. <https://doi.org/10.1007/s40962-023-01132-4>.

Kvande, Halvor. 2015. "Occurrence and Production of Aluminum." In *The Lightest Metals: Science and Technology from Lithium to Calcium*, edited by Robert A. Scott, 2nd ed. Wiley. <https://doi.org/10.1002/9781119951438.eibc2350>.

Lee, Choong do. 2013. "Effect of T6 Heat Treatment on the Defect Susceptibility of Fatigue Properties to Microporosity Variations in a Low-Pressure Die-Cast A356 Alloy." *Materials Science and Engineering: A* 559 (January):496–505. <https://doi.org/10.1016/j.msea.2012.08.131>.

Li, Cong, Thien Dang, Mertol Gökelma, Sebastian Zimmermann, Jonas Mitterecker, and Bernd Friedrich. 2023. "Assessment of Separation and Agglomeration Tendency of Non-Metallic Inclusions in an Electromagnetically Stirred Aluminum Melt." In , 906–14. [https://doi.org/10.1007/978-3-031-22532-1\\_120](https://doi.org/10.1007/978-3-031-22532-1_120).

Li, Cong, Mertol Gökelma, Wolfram Stets, and Bernd Friedrich. 2024. "The Separation Behavior of TiB<sub>2</sub> during Cl<sub>2</sub>-Free Degassing Treatment of 5083 Aluminum Melt." *Metals* 14 (March):402. <https://doi.org/10.3390/met14040402>.

Li, Hong-ying, De-wang Li, Zhi-xiang Zhu, Bao-an Chen, Xin Chen, Chang-long Yang, Hong-yu Zhang, and Wei Kang. 2016. "Grain Refinement Mechanism of As-Cast Aluminum by Hafnium." *Transactions of Nonferrous Metals Society of China* 26 (12): 3059–69. [https://doi.org/10.1016/S1003-6326\(16\)64438-2](https://doi.org/10.1016/S1003-6326(16)64438-2).

Li, Qinglin, Yuqian Zhu, Shang Zhao, Yefeng Lan, Dexue Liu, Guangfei Jian, Qiang Zhang, and Hongwei Zhou. 2020. "Influences of Fe, Mn and Y Additions on Microstructure and Mechanical Properties of Hypoeutectic Al-7%Si Alloy." *Intermetallics* 120 (May):106768. <https://doi.org/10.1016/j.intermet.2020.106768>.

Lide, David R. 2003. *Handbook of Chemistry and Physics*. 84th ed. CRC Press.

Mahmoud, M. G., E. M. Elgallad, M. F. Ibrahim, and F. H. Samuel. 2018. "Effect of Rare Earth Metals on Porosity Formation in A356 Alloy." *International Journal of Metalcasting* 12 (2): 251–65. <https://doi.org/10.1007/s40962-017-0156-5>.

Md Yahaya, Shamy Nazrein, I. Azmi, Chuan Huat Ng, Lai Chee Fung, mohd yussni Hashim, Anbia Adam, R. Baehr, and Karl Grote. 2020. "An Overview on Forming Process and Heat Treatments For Heat Treatable Aluminium Alloy." *Journal of Advanced Research in Fluid Mechanics and Thermal Sciences* 70 (April):112–24. <https://doi.org/10.37934/arfmts.70.1.112124>.

"Metallic Materials - Tensile Testing - Part 1:Method Of Testat Room Temperature, PN-EN ISO 6892-1: 2020-05." 2020.

Mohanty, P. S., and J. E. Gruzleski. 1995. "Mechanism of Grain Refinement in Aluminium." *Acta Metallurgica et Materialia* 43 (5): 2001–12. [https://doi.org/10.1016/0956-7151\(94\)00405-7](https://doi.org/10.1016/0956-7151(94)00405-7).

Muşdal, Ertan. 2018. "Effect of Iron Intermetallics on Aluminum-Silicon Alloys." Istanbul University.

Nikolic, Filip, Ivan Štajduhar, and Marko Čanađija. 2021. "Casting Microstructure Inspection Using Computer Vision: Dendrite Spacing in Aluminum Alloys." *Metals* 11 (May):756. <https://doi.org/10.3390/met11050756>.

Nogita, Kazuhiro, Stuart David McDonald, and Arne Kristian Dahle. 2003. "Effects of Boron-Strontium Interactions on Eutectic Modification in Al-10 mass%Si Alloys." *Materials Transactions* 44 (4): 692–95. <https://doi.org/10.2320/matertrans.44.692>.

Nunes, Helder, Omid Emadina, Rui Soares, Manuel F. Vieira, and Ana Reis. 2023. "Adding Value to Secondary Aluminum Casting Alloys: A Review on Trends and Achievements." *Materials* 16 (3): 895. <https://doi.org/10.3390/ma16030895>.



Ou, Jun, Chunying Wei, Steve Cockcroft, Daan Maijer, Lin Zhu, Lateng A, Changhai Li, and Zhihua Zhu. 2020. “Advanced Process Simulation of Low Pressure Die Cast A356 Aluminum Automotive Wheels—Part I, Process Characterization.” *Metals* 10 (5): 563. <https://doi.org/10.3390/met10050563>.

Özaydin, Onur, Elvan Armakan, and Alper Kaya. 2018. “The Mechanical Properties of Sr Modification on Aluminium Casting Alloys.” In .

Özaydin, Onur, A. Yiğit Kaya, and Yiğit Çatal. 2022. “Design and Analysis of Various Cooling Conditions of an Aluminium Wheel Mold.” *La Metallurgia Italiana* 3 (March):56.

Özaydin, Onur. 2015. “The Effects of Grain Refinement on the Mechanical Properties of Aluminium Cast Alloys Used in Automotive Industry.” Technische Universitat Dortmund, Turkish German University.

Özaydin, Onur, Elvan Armakan, Yiğit Kaya, and Aytaç Gören. 2019. “Yapay Yaşlandırma Şartlarının Jantın Darbe Özelliklerine Etkisi.” TÜDÖKSAD 2. Ulusal Döküm Kongresi, December.

Öztürk, Hüseyin. 2008. “Analysis And Design For Aluminum Forging Process.” Middle East Technical University.

Pearson, Karl, and Francis Galton. 1997. “VII. Note on Regression and Inheritance in the Case of Two Parents.” *Proceedings of the Royal Society of London* 58 (347–352): 240–42. <https://doi.org/10.1098/rspl.1895.0041>.

Peng, Ji-hua, Xiao-long Tang, Jian-ting He, and De-ying Xu. 2011. “Effect of Heat Treatment on Microstructure and Tensile Properties of A356 Alloys.” *Transactions of Nonferrous Metals Society of China* 21 (9): 1950–56. [https://doi.org/10.1016/S1003-6326\(11\)60955-2](https://doi.org/10.1016/S1003-6326(11)60955-2).

Pezda, Jacek. 2015. “Effect of Shortened Heat Treatment on Change of the Rm Tensile Strength of the 320.0 Aluminum Alloy.” *Archives of Foundry Engineering* 15 (March). <https://doi.org/10.1515/afe-2015-0013>.

Pozan, Makbule. 2022. “A356 Alaşımı Parçaların Mekanik Özelliklerinin Toz Formlu Tane İncelticiler Kullanılarak Geliştirilmesi.”

Raabe, Dierk, Dirk Ponge, Peter J. Uggowitzer, Moritz Roscher, Mario Paolantonio, Chuanlai Liu, Helmut Antrekowitsch, et al. 2022. "Making Sustainable Aluminum by Recycling Scrap: The Science of 'Dirty' Alloys." *Progress in Materials Science* 128 (July):100947. <https://doi.org/10.1016/j.pmatsci.2022.100947>.

Rao, P., Periyasamy P, Vasudeva Rao, Ramanan N., and Naveen. 2019. "Mechanical Behavior of Aluminum Metal Matrix Composite for Wheel Hub Application." *International Journal of Engineering and Advanced Technology* 9 (December):2146–49. <https://doi.org/10.35940/ijeat.B3618.129219>.

Reilly, C., J. Duan, L. Yao, D. M. Maijer, and S. L. Cockcroft. 2013. "Process Modeling of Low-Pressure Die Casting of Aluminum Alloy Automotive Wheels." *JOM* 65 (9): 1111–21. <https://doi.org/10.1007/s11837-013-0677-1>.

Riahi, A. R., and A. T. Alpas. 2006. "Fracture of Silicon-Rich Particles during Sliding Contact of Al–Si Alloys." *Materials Science and Engineering: A* 441 (1): 326–30. <https://doi.org/10.1016/j.msea.2006.08.043>.

Robles Hernandez, Francisco C., Jose Martin Herrera Ramirez, and Robert Mackay. 2017. "Al-Si Alloys, Minor, Major, and Impurity Elements." In *Al-Si Alloys*, by Francisco C. Robles Hernandez, Jose Martin Herrera Ramirez, and Robert Mackay, 1–15. Cham: Springer International Publishing. [https://doi.org/10.1007/978-3-319-58380-8\\_1](https://doi.org/10.1007/978-3-319-58380-8_1).

Runyoro, Joseph J., and J. Campbell. 1992. "The Running and Gating of Light Alloys." *Foundryman*, no. 85, 117–24.

Sanchez, Jon Mikel, Maribel Arribas, Haize Galarraga, Maider Garcia de Cortazar, Marco Ellero, and Franck Girod. 2023. "Effects of Mn Addition, Cooling Rate and Holding Temperature on the Modification and Purification of Iron-Rich Compounds in AlSi10MnMg(Fe) Alloy." *Heliyon* 9 (2): e13005. <https://doi.org/10.1016/j.heliyon.2023.e13005>.

Schlesinger, Mark E. 2014. *Aluminum Recycling, Second Edition*.

Schwarz, H.-G. 2004. "Aluminum Production and Energy." In *Encyclopedia of Energy*, 81–95. Elsevier. <https://doi.org/10.1016/B0-12-176480-X/00372-7>.

Seetharaman, Seshadri, Alexander McLean, Roderick I. L. Guthrie, and Seetharaman Sridhar. 2014. *Treatise on Process Metallurgy*. Vol. 3. Amsterdam Waltham Paris: Elsevier.

Sejal, Akre. 2024. "Automotive Alloy Wheel Market Size, Share, Growth Report 2030." <https://www.marketresearchfuture.com/reports/automotive-alloy-wheel-market-3931>.

Shakil, S. I., A. Hadadzadeh, B. Shalchi Amirkhiz, H. Pirgazi, M. Mohammadi, and M. Haghshenas. 2021. "Additive Manufactured versus Cast AlSi10Mg Alloy: Microstructure and Micromechanics." *Results in Materials* 10 (June):100178. <https://doi.org/10.1016/j.rinma.2021.100178>.

Shi, Zhiming, Qiang Wang, Yuting Shi, Ge Zhao, and Ruiying Zhang. 2015. "Microstructure and Mechanical Properties of Gd-Modified A356 Aluminum Alloys." *Journal of Rare Earths* 33 (9): 1004–9. [https://doi.org/10.1016/S1002-0721\(14\)60518-4](https://doi.org/10.1016/S1002-0721(14)60518-4).

Sigworth, Geoffrey. 2013. *Fundamentals of Solidification in Aluminum Castings*. *International Journal of Metalcasting*. Vol. 8. <https://doi.org/10.1007/BF03355567>.

Şimşek, İjlal, and Dursun Özyürek. 2019. "Investigation of the Effects of Mg Amount on Microstructure and Wear Behavior of Al-Si-Mg Alloys." *Engineering Science and Technology, an International Journal* 22 (1): 370–75. <https://doi.org/10.1016/j.jestch.2018.08.016>.

Singh, Harmeet, Gurinder Singh Brar, Harish Kumar, and Vikrant Aggarwal. 2021. "A Review on Metal Matrix Composite for Automobile Applications." *Materials Today: Proceedings*, 1st International Conference on Energy, Material Sciences and Mechanical Engineering, 43 (January):320–25. <https://doi.org/10.1016/j.matpr.2020.11.670>.

Song, XianChen, Hong Yan, QingJie Wu, and Zhi Hu. 2019. "Effect of (La+Yb) Addition on the Fluidity of an A356.2 Aluminum Alloy." *International Journal of Cast Metals Research* 32 (2): 59–66. <https://doi.org/10.1080/13640461.2018.1518744>.

Tabereaux, Alton T., and Ray D. Peterson. 2014. "Chapter 2.5 - Aluminum Production." In *Treatise on Process Metallurgy*, edited by Seshadri Seetharaman, 839–917. Boston: Elsevier. <https://doi.org/10.1016/B978-0-08-096988-6.00023-7>.

Taylor, John. 2004. *The Effect of Iron in Al-Si Casting Alloys*. 35th Australian Foundry Institute National Conference.

“Testing Of Metallic Materials – Tensile Test Pieces, Prüfung Metallischer Werkstoffe – Zugproben Deutsche Norm DIN50125, 2016.” 2016.

“The Aluminum Automotive Manual.” 2002. Designation System. European Aluminium Association.

Tigli, Ahmet, and Derya Dispinar. 2023. “Correlation Between K-Value, Density Index and Bifilm Index in Determination of Liquid Al Cleanliness.” *Archives of Foundry Engineering*, August. <https://doi.org/10.24425/afe.2023.144311>.

Tocci, Marialaura, Annalisa Pola, Giovina La Vecchia, and Modigell Michael. 2015. “Characterization of a New Aluminium Alloy for the Production of Wheels by Hybrid Aluminium Forging.” *Procedia Engineering* 109 (December):303–11. <https://doi.org/10.1016/j.proeng.2015.06.237>.

Tsai, Yu-Chou, Cheng-Yu Chou, Sheng-Long Lee, Chih-Kuang Lin, Jing-Chie Lin, and David S.W. Lim. 2009. “Effect of Trace La Addition on the Microstructures and Mechanical Properties of A356 (Al–7Si–0.35Mg) Aluminum Alloys.” *Journal of Alloys and Compounds* 487 (November):157–62. <https://doi.org/10.1016/j.jallcom.2009.07.183>.

Uludağ, Muhammet, R. Çetin, and Derya Dispinar. 2017. “Observation of Hot Tearing in Sr-B Modified A356 Alloy.” *Archives of Foundry Engineering* 17 (December). <https://doi.org/10.1515/afe-2017-0151>.

Warmuzek, Małgorzata. 2004. *Aluminum-Silicon Casting Alloys: Atlas of Microfractographs*. 1. print. Materials Park, Ohio: ASM International.

“Wheel Testing Services.” n.d. TÜV SÜD. Accessed April 7, 2024. <https://www.tuvsud.com/en/industries/mobility-and-automotive/automotive-and-oem/automotive-testing-solutions/wheel-testing>.

Wilczynski, A., M. Bartczak, Krzysztof Siczek, and Przemysław Kubiak. 2018. “Carbon Fibre Reinforced Wheel for Fuel Ultra-Efficient Vehicle.” *Mechanics and Mechanical Engineering* 22 (December):1419–37. <https://doi.org/10.2478/mme-2018-0111>.

Woycik, Gregory G., and Gordon Peters. 2008. “Low-Pressure Metal Casting.” In *ASM Handbook Casting*, 15:700–703.

Wu, Chih-Ting, Sheng-Long Lee, Ye-Feng Chen, Hui-Yun Bor, and Kung-Hui Liu. 2020. "Effects of Mn, Zn Additions and Cooling Rate on Mechanical and Corrosion Properties of Al-4.6Mg Casting Alloys." *Materials* 13 (8): 1983. <https://doi.org/10.3390/ma13081983>.

Xu, Cong, Wenlong Xiao, Shuji Hanada, Hiroshi Yamagata, and Chaoli Ma. 2015. "The Effect of Scandium Addition on Microstructure and Mechanical Properties of Al-Si-Mg Alloy: A Multi-Refinement Modifier." *Materials Characterization* 110 (December):160–69. <https://doi.org/10.1016/j.matchar.2015.10.030>.

Zabalegui, E., J. Huarte, E. Zoco, J. Arraiza, E. Rivero, A. Rios, Inigo Anza, et al. 2014. *Development of a New Methodology to Use Recycled Secondary Aluminum Substituting Primary A356 Aluminum Alloy in Safety Components in Low Pressure Technology*.

Závodská, Denisa, Eva Tillová, Ivana Švecová, Mária Chalupová, Lenka Kuchariková, and Juraj Belan. 2018. "The Effect of Iron Content on Microstructure and Porosity of Secondary AlSi7Mg0.3 Cast Alloy." *Periodica Polytechnica Transportation Engineering* 47 (4): 283–89. <https://doi.org/10.3311/PPtr.12101>.

Závodská, Denisa, Eva Tillová, Ivana Švecová, Lenka Kuchariková, and Mária Chalupová. 2018. "Secondary Cast Al-Alloys with Higher Content of Iron." *Materials Today: Proceedings* 5 (13): 26680–86. <https://doi.org/10.1016/j.matpr.2018.08.135>.

Zhang, qi, Miao Cao, Da-Wei Zhang, Shuai Zhang, and Jue Sun. 2015. "Research on Integrated Casting and Forging Process of Aluminum Automobile Wheel." *Advances in Mechanical Engineering* 6 (February):870182–870182. <https://doi.org/10.1155/2014/870182>.

Zolotarevsky, Vadim, N. Belov, and Michael Glazoff. 2007. "Chapter 5. Industrial Casting Aluminum Alloys, Pp.327-396 Casting Aluminum Alloys, Elsevier, Amsterdam 2007." 327–96.